



# Numerical Investigation of Transonic Buffet Control Using a Two-Dimensional Bump

A thesis submitted in fulfilment of the requirements for the degree of Master of  
Engineering

Zheng Yang

Bachelor of Engineering  
The University of Sheffield

School of Engineering  
College of Science, Engineering and Health  
RMIT University

March 2020

## Declaration

I certify that except where due acknowledgement has been made, the work is that of the author alone; the work has not been submitted previously, in whole or in part, to qualify for any other academic award; the content of the thesis is the result of work which has been carried out since the official commencement date of the approved research program; any editorial work, paid or unpaid, carried out by a third party is acknowledged; and, ethics procedures and guidelines have been followed.

Name: Zheng Yang

---

Signature:

---

Date: 17 March 2020

---

## Acknowledgements

Over the last two years, my life has been so special. After graduating from Sheffield University in the UK with a bachelor degree in summer 2016, I was not satisfied with what I've done, so I decided to come to Australia for further education. The original chosen course was a Master by coursework in Aerospace Engineering, which has a similar course structure as my undergraduate study. Right, I've failed once, so I cannot afford to make the same mistake again. I must study hard to turn things around! One day when I was walking to Swanston Library I met a colleague from my class, who told me that she just changed her course to a Master by Research. Really? I was so surprised to hear that! Why not consider doing a Research degree instead of coursework and switching to PhD if possible? This is a huge inspiration. So, I quit my original course and started a new application, and I stepped on an entirely new pathway that I've never followed before. Thank you so much, my colleague, my fellow Chinese friend. I very much regret that I had no chance to ask your name. I will remember you forever.

Having made up my mind of undertaking research, I spoke to one of our course lecturers, Dr Hideaki Ogawa, who later became my senior supervisor. After a few discussions through emails and face-to-face meetings, I finally established my research topic by finishing a research proposal. I express my sincere gratitude to Dr Ogawa for everything he did for me throughout the journey. Thank you for your patience of kindly responding to my questions and doubts from my emails; thank you for your time listening to my opinions and providing suggestions in every regular meeting; thank you for reviewing my conference paper and thesis; thank you for allowing me to work on your iMac machine; thank you for your warm welcome to your apartment and your herbal tea, and so on. I understand your ego of fulfilment that motivates you to be appointed as an Associate Professor at Kyushu University, which stopped you to continuously serve as my senior supervisor at RMIT. I respect your decision, and I wish you the best of luck with your career and your family.

Some special acknowledgements also go to the academic panel: Professor Pier Marzocca, who took over the supervision from Hideaki. I thank him for approving the extension request for my thesis submission, and also his valuable feedback in the milestone review. Professor Simon Watkins, who chaired my last two milestone review sessions, very appreciated for your unerring advice. Dr Francisco Gomez, who previously acted as my associate senior supervisor, thank you for your guidance as well. Dr Robert Carrese and Dr Woutijn Baars, thank you all for your technical comments as independent assessors. A special thank to the School Service Assistant Ms Mary Tomlinson for her incredible kindness. There have been so many times that I asked her for the entrance to the secure room for the access of the iMac machine,

and she always patiently relied my request either from email or in person and showed great willingness to help no matter what.

In addition, I would like to personally acknowledge one of my best friends that I knew in Melbourne, Suk Hyun Yeo. We are all Dr Ogawa's students and we were very lucky to know each other when taking a conference trip in Chengdu, China. We had a great hot pot meal and an amazing crayfish feast for dinner with your wife's family, and we had so much fun together. What an unforgettable memory! Thank you for being a good friend of mine. I wish you all the best with your PhD study and hope our friendship would never end for the rest of life!

Finally, I express my deepest gratitude to my parents. Thank you for your love and always being so generous and supportive at every stage of my life. I would have not persisted for so long without your continuous encouragements. This thesis is dedicated to you, mom and dad!

## Abstract

The aerodynamic performance of a transonic aircraft wing is strongly influenced by the interaction between the shock wave and the boundary-layer. The shock wave caused by locally supersonic flow and the viscosity existing in a boundary-layer can lead to several undesirable phenomena such as flow instability, drag rise, and buffet. These phenomena can crucially limit the flight envelop and hence operation. Flow instability is caused by the flow unsteadiness that exists in shock-induced separation, thus creating turbulence around a streamlined body such as aerofoils and transonic gas turbine blades. Drag rise, also known as drag-divergence phenomenon, is related to a concept called sound barrier, which implies that the aerodynamic drag exerted on a body can be extremely high as the flow speed approaches to the speed of sound. Buffet is rather complex, as it can be recognised as a coexistence phenomenon of which both flow instability and drag-divergence that are likely to occur simultaneously. The implication of this statement can be interpreted as follows: buffet can be triggered at a critical flow condition when the separated airflow creates unsteady pressure waves that can interact with a shock wave caused by the formation of locally supersonic flow, and the flow speed enters a regime where compressibility effect is dominant. The mechanism of transonic buffet can be characterised in the forms of self-sustained shock oscillation, unsteady pressure fluctuation and the generation of wave drag. Self-sustained shock oscillation is a periodic shock movement taking place on 2D transonic aerofoils and Diverterless Supersonic Intakes (DSI) with a frequency at about 70Hz to 80Hz, and this frequency of oscillation depends on the flow Mach number and the angle of attack. Pressure fluctuation acts as a time response of pressure variation associated with shock wave/boundary-layer interaction. The level of unsteady pressure fluctuation becomes significant at the shock location and the trailing edge, which can be felt as a structural vibration on the tail unit of an airframe. Wave drag is an independent drag component, which is created by the loss of stagnation pressure across a shock wave. It has been demonstrated experimentally that a 3D surface bump configuration can fulfil two objectives in shock wave/boundary-layer control, drag reduction and buffet delay. However, a rather few studies that investigate the aerodynamic performance associated with an unsteady transonic flow in the presence of a surface bump, which still withholds a couple of unknown aspects that need to be found out, such as the control mechanisms, impacts, benefits, and drawbacks.

The current research is undertaken by performing Computational Fluid Dynamics (CFD) simulations for a 2D aerofoil fitted with a shock control bump at a transonic flow condition. Reynolds-Averaged Navier-Stokes equation coupled with turbulence models is adopted to solve the flowfield. The bump has a conventional geometric feature which consists of a ramp, a crest and a tail, and it has eight variants for which the designed parameters are reasonably

specified according to the compressible aerodynamics theory. The bumps are placed at a forward and backward position on the suction side of the aerofoil, on which a shock wave is present. The forward position is 30% of the aerofoil chord and the backward position is 40% of the aerofoil chord. The chosen mathematical model is considered to be reliable as it has been well-validated by comparing the numerical results with the experimental data, in terms of the surface pressure distribution, unsteady pressure fluctuation and streamwise velocity profiles. Qualitative analysis is conducted through scrutinising the uncontrolled and controlled flowfields. The Mach number contours show that the forward bumps could generate a large oblique shock structure followed by an additional flow re-expansion due to the locally re-accelerated supersonic flow, while the backward bumps do not incur significant secondary expansion waves, and the oblique shock structure becomes relatively weaker and smaller on the backward bumps. Then, the control effectiveness of shock control bumps is analysed quantitatively. The control performance for each type of bump configuration is evaluated by computing the transient responses of the lift and drag coefficients, both in time and frequency domain. The results show that a shock control bump can mitigate the periodic lift oscillation that associates with a transonic buffet flow by attenuating the frequency and amplitude of the oscillation. The unsteady fluctuation of surface static pressure is calculated using an appropriate statistical approach. This analysis reveals that a bump with a low crest height is the most effective to suppress pressure fluctuation on an aerofoil globally. Finally, the overall aerodynamic performance is assessed by evaluating the lift curves, the effect of drag-divergence, lift-to-drag ratio and the parasitic drag. This assessment concludes that the bumps can lag the stall angle of attack, as well as delaying the drag-divergence Mach number. The bumps can offer an effective reduction of the total drag but incur a little penalty in the viscous drag. Recommendation for future work has been proposed with an emphasis on the shape optimisation of the bump geometry and the prediction of the buffet boundary for an optimum design configuration.

# Contents

<b>1</b>	<b>Introduction</b>	<b>1</b>
<b>2</b>	<b>Literature Review</b>	<b>4</b>
2.1	Overview . . . . .	4
2.2	Shock-induced boundary-layer separation . . . . .	5
2.3	Flow unsteadiness in shock-induced separation . . . . .	7
2.4	Periodic shock oscillation . . . . .	7
2.4.1	Transonic aerofoils . . . . .	7
2.4.2	Supersonic engine diffusers . . . . .	8
2.5	Shock control bump . . . . .	9
2.5.1	Control performance . . . . .	10
2.5.2	Flow structure . . . . .	11
2.6	Summary . . . . .	11
2.7	Aim and objectives . . . . .	12
2.8	Research questions . . . . .	12
<b>3</b>	<b>Methodology</b>	<b>13</b>
3.1	Governing equation . . . . .	13
3.2	Turbulence modelling . . . . .	15
3.2.1	One-equation model . . . . .	15
3.2.2	Two-equation model . . . . .	16
3.3	Design of bump configurations . . . . .	18
3.4	Numerical method . . . . .	22
3.5	Mesh and time step independence study . . . . .	23
3.6	Sensitivity of turbulence models . . . . .	25
3.6.1	Aerofoil without control . . . . .	25
3.6.2	Aerofoil with control . . . . .	27
<b>4</b>	<b>Results</b>	<b>33</b>
4.1	Flowfield properties . . . . .	33
4.1.1	Mach number distribution . . . . .	33
4.1.2	Streamwise velocity profiles . . . . .	39
4.2	Transient solutions . . . . .	43
4.2.1	Unsteady lift . . . . .	43
4.2.2	Unsteady pressure fluctuation . . . . .	51

<b>5</b>	<b>Discussion of results</b>	<b>54</b>
5.1	No control . . . . .	54
5.2	With control . . . . .	54
5.3	Aerodynamic performance . . . . .	55
5.3.1	Lift curve . . . . .	55
5.3.2	Effect of drag divergence . . . . .	60
5.3.3	Drag comparison . . . . .	63
<b>6</b>	<b>Conclusions and future work</b>	<b>66</b>
6.1	Conclusions . . . . .	66
6.2	Recommendation for future work . . . . .	68

# List of Figures

1.1	Transonic aircraft wing [Wikimedia (2013)] . . . . .	2
1.2	Numerical pressure distribution on an aircraft fuselage and wing [Murayama et al. (2013)] . . . . .	2
2.1	Definition of separation onset[Kim et al. (1996)] . . . . .	5
2.2	Wall pressure distribution of Shock wave/boundary-layer interaction on (a) forward-facing step and (b) compression ramp[Kim et al. (1996)] . . . . .	6
2.3	Model of self-sustained shock oscillation[Lee (1990)] . . . . .	8
2.4	Schematic of a shock control bump: a) in relation with the aerofoil; b) zoom in of the bump and design parameters[Sabater and Görtz (2019)] . . . . .	9
2.5	Bifurcated $\lambda$ -shock structure on a surface bump with wake total pressure profiles [Ogawa et al. (2008) & Bruce and Colliss (2015)] . . . . .	10
3.1	Geometrical feature of a standard bump(not to scale) . . . . .	19
3.2	Schematic of a baseline aerofoil with bump(not to scale) . . . . .	19
3.3	Theoretical oblique shock relations in transonic flow conditions . . . . .	20
3.4	Schematic of different bump geometries (Forward position) . . . . .	21
3.5	Schematic of different bump geometries (Backward position) . . . . .	21
3.6	(a) Farfield domain and (b) structured mesh around an OAT15A aerofoil . . . . .	23
3.7	Mesh independence studies of (a) lift and (b) drag coefficients for a baseline aerofoil ( $M_\infty=0.73$ , $\alpha=3.5^\circ$ ) . . . . .	24
3.8	Time responses of lift coefficient for various time steps ( $M_\infty=0.73$ , $\alpha=3.5^\circ$ ) . . . . .	24
3.9	Buffet-onset frequencies for CFD, theory and experiment ( $\alpha=3.5^\circ$ ) . . . . .	25
3.10	Pressure profiles for different (a) angles of attack and (b) turbulence models ( $M_\infty=0.73$ ) . . . . .	26
3.11	Root-Mean-Squared pressure fluctuations for different (a) angles of attack and (b) turbulence models ( $M_\infty=0.73$ ) . . . . .	26
3.12	Wall shear stress for different (a) angles of attack and (b) turbulence models ( $M_\infty=0.73$ ) . . . . .	27
3.13	Pressure profiles for forward bumps with different turbulence models ( $M_\infty=0.73$ , $\alpha=3.5^\circ$ ) . . . . .	28
3.14	Pressure profiles for backward bumps with different turbulence models ( $M_\infty=0.73$ , $\alpha=3.5^\circ$ ) . . . . .	29
3.15	Upper surface shear stress distributions for forward bumps with different turbulence models ( $M_\infty=0.73$ , $\alpha=3.5^\circ$ ) . . . . .	30

3.16	Upper surface shear stress distributions for backward bumps with different turbulence models ( $M_\infty=0.73$ , $\alpha=3.5^\circ$ ) . . . . .	31
4.1	Transient Mach number contour on an aerofoil without control ( $M_\infty=0.73$ , $\alpha=3.5^\circ$ ) . . . . .	34
4.2	Mach number contours for forward bumps ( $M_\infty=0.73$ , $\alpha=3.5^\circ$ ) . . . . .	35
4.3	Flow structures in the vicinity of forward bumps ( $M_\infty=0.73$ , $\alpha=3.5^\circ$ ) . . . . .	36
4.4	Mach number contours for backward bumps ( $M_\infty=0.73$ , $\alpha=3.5^\circ$ ) . . . . .	38
4.5	Flow structures in the vicinity of backward bumps ( $M_\infty=0.73$ , $\alpha=3.5^\circ$ ) . . . . .	39
4.6	Streamwise velocity profiles at four different locations on a baseline aerofoil ( $M_\infty=0.73$ , $\alpha=3.5^\circ$ ) . . . . .	40
4.7	Local streamwise velocity profiles within one buffet cycle for a baseline aerofoil ( $M_\infty=0.73$ , $\alpha=3.5^\circ$ , $x/c=0.6$ ) . . . . .	41
4.8	Streamwise velocity profiles at $x/c=0.6$ for different bumps ( $M_\infty=0.73$ , $\alpha=3.5^\circ$ ) . . . . .	42
4.9	Time histories of (a) lift and (b) drag coefficients for a baseline aerofoil with different turbulence models ( $M_\infty=0.73$ , $\alpha=3.5^\circ$ ) . . . . .	43
4.10	PSD of (a) lift and (b) drag coefficients for a baseline aerofoil with different turbulence models ( $M_\infty=0.73$ , $\alpha=3.5^\circ$ ) . . . . .	44
4.11	(a) Time and (b) frequency responses of lift coefficient for a baseline aerofoil with different angles of attack ( $M_\infty=0.73$ ) . . . . .	44
4.12	Lift response for forward bumps ( $M_\infty=0.73$ , $\alpha=3.5^\circ$ ) . . . . .	46
4.13	Lift response for backward bumps ( $M_\infty=0.73$ , $\alpha=3.5^\circ$ ) . . . . .	47
4.14	PSD of lift coefficient for forward bumps ( $M_\infty=0.73$ , $\alpha=3.5^\circ$ ) . . . . .	48
4.15	PSD of lift coefficient for backward bumps ( $M_\infty=0.73$ , $\alpha=3.5^\circ$ ) . . . . .	49
4.16	(a) Time and (b) frequency responses of lift coefficient with/without control ( $M_\infty=0.73$ , $\alpha=4.0^\circ$ ) . . . . .	50
4.17	Root-Mean-Squared pressure fluctuation distributions for forward bumps ( $M_\infty=0.73$ , $\alpha=3.5^\circ$ ) . . . . .	51
4.18	Root-Mean-Squared pressure fluctuation distributions for backward bumps ( $M_\infty=0.73$ , $\alpha=3.5^\circ$ ) . . . . .	52
5.1	Lift curves for forward bumps ( $M_\infty=0.73$ ) . . . . .	56
5.2	Lift curves for backward bumps ( $M_\infty=0.73$ ) . . . . .	57
5.3	Lift curves for forward bumps ( $M_\infty=0.75$ ) . . . . .	58
5.4	Lift curves for backward bumps ( $M_\infty=0.75$ ) . . . . .	59
5.5	Total drag coefficient verses Mach number for forward bumps ( $\alpha=3.5^\circ$ ) . . . . .	61
5.6	Total drag coefficient verses Mach number for backward bumps ( $\alpha=3.5^\circ$ ) . . . . .	62
5.7	Total drag comparisons for the forward bumps ( $M_\infty=0.73$ , $\alpha=3.5^\circ$ ) . . . . .	63
5.8	Total drag comparisons for the backward bumps ( $M_\infty=0.73$ , $\alpha=3.5^\circ$ ) . . . . .	64
5.9	Viscous drag comparisons for the forward bumps ( $M_\infty=0.73$ , $\alpha=3.5^\circ$ ) . . . . .	64
5.10	Viscous drag comparisons for the backward bumps ( $M_\infty=0.73$ , $\alpha=3.5^\circ$ ) . . . . .	65

# List of Tables

3.1	Forward bump parameters( $x/c=30\%$ ) . . . . .	18
3.2	Backward bump parameters( $x/c=40\%$ ) . . . . .	19
4.1	Shock angle comparison with forward bumps . . . . .	37
4.2	Shock angle comparison with backward bumps . . . . .	37

# Chapter 1

## Introduction

In the last century, modern aviation technology starts to develop on an unprecedented scale since the first mechanically powered flight was successfully fulfilled by Wright Brothers in 1903. Earlier than 1940s, aeroplanes were designed to fly marginally lower than the speed of sound. This is due to a concept called sound barrier, a drag-divergence phenomenon that existed to be a myth for more than a decade. Eventually on October of 1947, the first manned and faster-than-sound flight was achieved by the Bell XS-1 rocket-propelled aircraft. This extraordinary breakthrough owes to the in-depth understanding of transonic aerodynamics. In a transonic flow regime, a locally supersonic flow can be formed as the freestream flow reaches the critical Mach number, incurring shock waves on an aircraft wing. The locally increased adverse pressure gradient behind the shock wave causes the boundary-layer to separate, resulting in an undesirable effect called shock stall, also known as buffet, which is characterised by a self-sustained shock oscillation taking place on the suction side of a wing. The separated airflow downstream to the shock wave can engulf the trailing edge of a wing in an unsteady wake, which could lead to significant structural vibration on an airframe thus limit the flight envelope.

High-speed induced buffet can be artificially prevented by equipping a warning system onboard to alert the pilot whether or not the aeroplane exceeds its operational speed limit. However, human intervention by no means makes a difference in effective buffet precaution. More reliable measures need to be adopted with respect to the aerodynamic design and flow control technique. This implies that a tiny change in flow configuration can bring a range of dramatic engineering benefits in terms of drag reduction, turbulence suppression and mixing enhancement. The control mechanism is generally accomplished in two manners: active and passive control. An active flow control configuration is a dynamic system like actuators which dissipate energy, while a passive flow control device is a static configuration that requires no external energy. Both control techniques nowadays are progressing rapidly in the area of fluid dynamics and have been extensively used in various applications.

Nevertheless, the physical mechanism of transonic buffet is yet to be fully understood, and controlling the flow unsteadiness from shock stall remains to be a major concern for aeronautical engineers as the governing equation of fluid motion, namely the Navier-Stokes equation,



**Figure 1.1:** *Transonic aircraft wing [Wikimedia (2013)]*

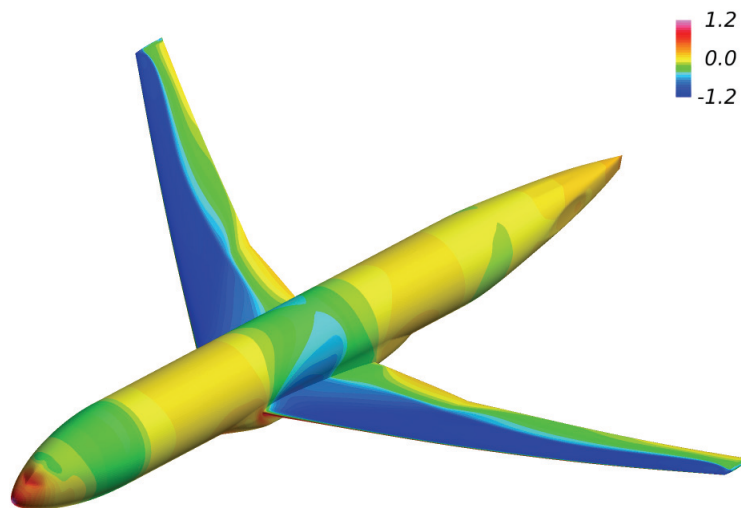


**Figure 1.2:** *Numerical pressure distribution on an aircraft fuselage and wing [Murayama et al. (2013)]*

is extremely difficult to solve. Thankfully, a state-of-the-art science Computational Fluid Dynamics (CFD) simplifies the problem of understanding complex flows around an object as well as evaluating its aerodynamic forces. A complete CFD simulation is performed in three procedures: pre-processing, solver and post-processing. Pre-processing begins with defining the geometry and discretising the flow domain. Solver contains a number of settings that are specified for calculation, such as boundary condition, turbulence model and numerical scheme. Post-processing is an extraction of the numerical solution from the solver, which can

be obtained by displaying the velocity, pressure and temperature distributions over the geometry. Such a procedure can be done in a relatively efficient and economical way compared to a wind tunnel experiment.

Preceding research on Shock wave/boundary-layer interaction (SBLI) has suggested that a surface bump possesses a potential to delay buffet on a wing at a transonic Mach number. However, a rather few experimental or computational studies have been carried out to demonstrate this advantage. Hence, the direction of research falls within the physical mechanism of how transonic buffet can be controlled using a 2D surface bump via Computational Fluid Dynamics approach. The scope of this thesis includes: Designs of eight bump configurations, four of which are placed at a forward position on an aerofoil's upper surface and the remaining four are on a backward position. Two elements of the bump geometry are varied, which are the chord length and the crest height. The first bump has a long chord length and a high crest; the second bump has a long chord length and a low crest; the third bump has a short chord length and high crest and the fourth bump has a short chord length and low crest. The backward bumps have similar geometrical features like the forward ones. The control effectiveness for all bumps has been assessed numerically. A validation assessment has been carried out by comparing the numerical surface static pressure distribution, the unsteady pressure fluctuation and the streamwise velocity profiles with the experimental measurements; flowfield characteristics that associates with the controlled and uncontrolled cases have been elaborated and summarised; control performance analysis with the transient variations of lift and drag as both time and frequency signals; overall aerodynamic performances in terms of the lift curves and the drag-rise are evaluated for all individual bumps. Finally, the control principle of a 2D surface bump has been explained and summarised in both qualitative and quantitative manner based on the produced numerical results.

## Chapter 2

# Literature Review

### 2.1 Overview

In civil engineering, buffet refers to the structural dynamics of a suspension bridge in the exposure of unsteady wind. In the automotive industry, a dynamic structural response called sunroof buffet is a dominant factor of the noise source in a vehicle. These two types of structural dynamics associated with a branch of mechanics called aeroelasticity, a subject that studies how an elastic object responds to an aerodynamic excitation. In the context of aeronautical engineering, the dynamic instability of a wing structure in an airstream is called flutter, which involves the interaction of flexural and torsional motion. Another type of dynamic response called wing buffet also plays a vital role in modern aeronautics. This kind of buffet is a single degree of freedom oscillation that is produced most commonly in a tailplane by eddies caused by poor airflow in the wing wake striking the tailplane at a resonant frequency [Megson (2016)]. This concept was firstly introduced in 1930 after the tail failure of a Junkers monoplane [Mabey (1981)]. The investigation of this failure leads to two general interpretations: a flow separation caused by disturbance from a severe gust and a direct structural failure of the wing due to a significant load of a gust. These interpretations imply that buffet typically initiates at critical flight conditions, especially when the aerodynamic load approaches to a limit or the aeroplane reaches its boundary of lateral or longitudinal stability. Buffet can also occur in cavities such as aircraft bomb-bays, steam turbine exhaust diffusers, turbomachinery blades and supersonic engine intakes [Raghunathan et al. (1999)]. Recent extensive research has shown that the nature of buffet can be characterised as a high-frequency pressure fluctuation associated with the separated flow behind the shock wave. Such fluctuation can cause a periodic shock movement over the aerofoil surface, which can be felt like a strong forced-vibration on the aircraft structure.

Mabey (1989) develops different buffet criteria for the wings of fighter and transport aircraft, as well as an experimental approach of predicting the onset and severity of buffet. The wind-tunnel experiment was done by NASA in 1970 on a series of 11 swept wings with a quarter chord swept angle of  $35^\circ$  and an aspect ratio of 6. Based on the acquired measurements, a fighter aircraft typically cruises well below the boundary of the onset of buffet, but it could go far beyond the boundary as it performs aerobatic manoeuvring. In contrast, a transport aircraft generally cruises about 10% below the lift coefficient at the onset of buffet. In an

unlikely event, the aircraft may encounter a strong gust of load that can take the aircraft right up to the moderate level of buffet. However, it is understandable that the extent of penetration beyond the buffet boundary will not be crucially influential unless there are additional factors involved, such as wing rocking, dropping, pitch-up and stalling.

## 2.2 Shock-induced boundary-layer separation

Wind tunnel experiments have proved that the interaction between shock waves and viscous boundary-layers takes place on two-dimensional aerofoils at transonic speeds. The appearance of separation depends chiefly upon the pressure gradient, and that the turbulent boundary-layer can withstand a much greater pressure increase before separation than can a laminar boundary-layer [Lange (1954)]. When a shock wave is stronger than certain strength, a destabilizing action due to its adverse pressure gradient is imparted into the boundary layer flow, leading to the occurrence of shock-induced boundary-layer separation (SIBLS) [Kim et al. (1996)]. By definition, an incipient separation occurs at zero wall shear stress for a given Mach number, namely the onset of separation. The boundary-layer is said to be fully separated when the wall shear stress becomes negative, as illustrated in Figure 2.1. The characteristics of the surface pressure distribution in the vicinity and downstream of the separation is

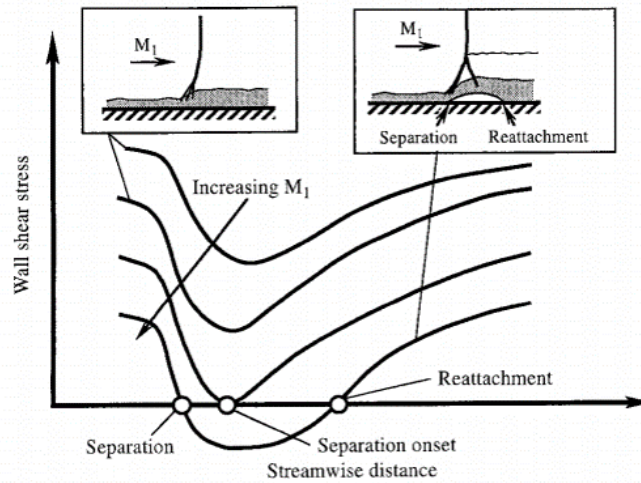


**Figure 2.1:** *Definition of separation onset*[Kim et al. (1996)]

presented in Figure 2.2, and the onset of SIBLS is diagnosed by considering the variation of the normalized pressure as a function of upstream Mach number, namely the shock strength [Pearcey (1959)]. According to Love (1955), there are two distinct points of interest on the pressure distribution associated with the Shock wave/boundary-layer interaction that causes separation. The first point is called the pressure rise at the separation point, and the second is the so-called first-peak pressure rise downstream to the separation point, as indicated on the pressure distribution for a forward-facing step and a compression ramp shown in Figure 2.2.

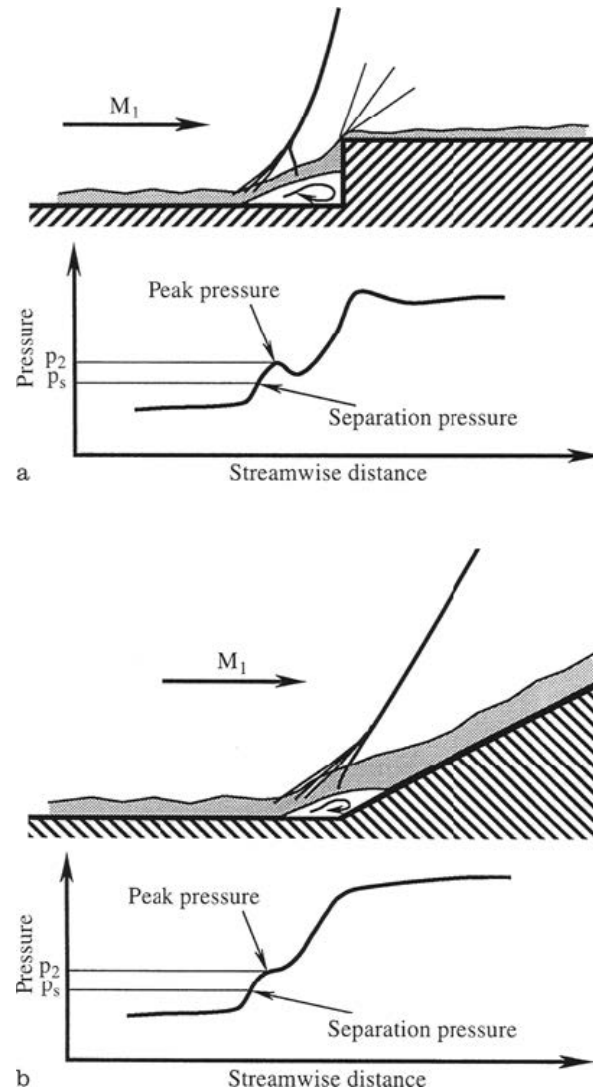


**Figure 2.2:** Wall pressure distribution of Shock wave/boundary-layer interaction on (a) forward-facing step and (b) compression ramp [Kim et al. (1996)]

Several instrumental-based criteria have been established to determine the onset of SIBLS. Stanewsky and Little (1971) constructs a criterion for separation measurement by associating the boundary-layer displacement thickness at certain stations on an aerofoil with the Mach number downstream to the shock wave. Alber et al. (1973) derives a practical approach by employing the oil-tracers to detect separation on a wing surface. The Alber criterion shows that the separation onset occurs when the upstream Mach number is 1.32 and the local outer Mach number at the separation point is sonic. Piponniau et al. (2009) proposed a model that explains the low-frequency unsteadiness found in shock-induced separation. This model supports the observation from an experiment done by a particle image velocimetry (PIV) in a Mach 2.3 oblique shock wave/turbulent boundary-layer interaction.

## 2.3 Flow unsteadiness in shock-induced separation

The prediction of the onset of the unsteadiness created by shock-induced buffet flow is generally performed on a transonic aerofoil but not limited to since its behaviour is similar to the buffet response of an aeroplane. Controlled wind tunnel tests show that the onset of flow unsteadiness is caused by large pressure fluctuations near and downstream of the main shock, as the angle of attack increases. Ganapathisubramani et al. (2007) investigates the relationship between the upstream boundary-layer and the low-frequency and large-scale unsteadiness of the separated flow in a Mach 2 compression ramp by performing a wide-field particle image velocimetry (PIV) and a planar laser scattering (PLS) measurements in streamwise-spanwise planes. The statistical analysis from instantaneous PIV and PLS fields indicate that the turbulent mechanism that accounts for the low-frequency unsteadiness within the shock-induced separation region can cause an elongated low and high-speed regions in the upstream boundary-layer.

A considerable amount of numerical research has also been conducted to fulfil the need for a better understanding of the low-frequency unsteadiness observed in shock wave/turbulent boundary-layer interactions. Toubert and Sandham (2009) presents a LES investigation for an oblique shock wave generated by an 8-degree wedge angle impinging on a Mach 2.3 turbulent boundary-layer by using the inflow technique, which makes a Fourier analysis of the low-frequency unsteadiness in a turbulent shock-induced separation bubble possible. The long-run and large-eddy simulation data lead to a possible driving mechanism for the observed low-frequency motion.

## 2.4 Periodic shock oscillation

### 2.4.1 Transonic aerofoils

The shock wave oscillations on aerofoils at transonic flow condition directly associate with buffet phenomenon. These oscillations are observed to be periodic, self-sustained and sinusoidal, but none of their features is entirely identical. Tijdeman (1977) conducted an experiment on a NACA 64A006 aerofoil with an oscillating trailing edge flap, from which three possible modes of shock oscillations are summarised. The oscillation modes are detected at three Mach numbers, which are Mach 0.85, 0.875 and 0.9. The type A shock motion occurs at Mach 0.9, at which shock waves are generated on both side of the aerofoil and they move in an anti-phase manner during the oscillation period. At Mach 0.875, the shock motion is approximately quasi-steady and sinusoidal without any phase-lag movement, but the shock becomes very weak and it starts to degrade into weak compression waves. This is classified as type B shock motion, of which mechanism has been investigated on an 18% thick biconvex aerofoil using a splitter plate technique and thin-layer Navier-Stokes code by [Raghuathan et al. (1999)]. This study reveals the fact that the shock-induced separation is the root-cause of periodic shock oscillation. The type C shock motion occurs at Mach 0.875 when weak compression waves replace the shock wave in a part of the oscillation cycle.

Lee (2001) provided a detailed explanation for the mechanism of self-sustained shock oscillation on transonic aerofoils. This mechanism has been confirmed experimentally and is identified as a feedback interaction between the pressure waves generated in the separated flow region and the disturbance waves generated in the unsteady turbulent wake. These waves impart energy to keep the shock oscillating, as illustrated in Figure 2.3. More detailed flow behaviour of shock oscillation has been further explored with a new experiment executed in the *ONERA S3Ch* transonic wind tunnel for an OAT15A supercritical wing. This experiment not only provides the CFD community with the well-documented test cases to validate the computational algorithm but also allows the precise definition of the conditions for the onset of buffet and the characterization of the properties of the periodic shock motion from unsteady surface pressure measurements. It also strongly suggests that the nature of shock oscillation is essentially two-dimensional, even if three-dimensional effects are detected [Jacquin et al. (2009)].

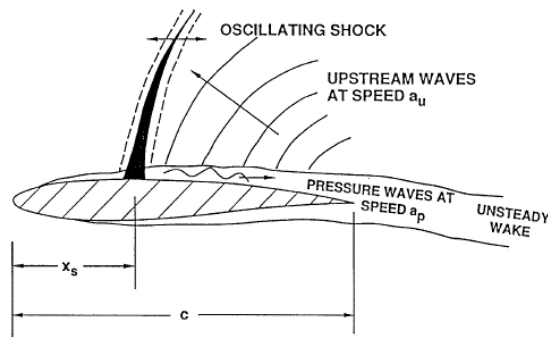


Figure 2.3: Model of self-sustained shock oscillation [Lee (1990)]

### 2.4.2 Supersonic engine diffusers

Supersonic aircraft and missile inlets may exhibit self-sustained oscillations (dynamic distortion, buzz) which constitute major limitations in off-design vehicle performance [Bogar (1986)]. The buzz in turbo-machinery systems can lead to compressor stall or blade fatigue, affecting compression efficiency and thrust production. A common solution to this issue is to estimate the safety margin for various operating requirements. This estimation is empirically done with costly wind tunnel tests, and the results are often over-predicted. To satisfactorily consider the self-sustained oscillation during the design process, several experimental techniques are proposed to study the structure of the self-excited oscillation in diffusers. Chen et al. (1979) studies the self-excited oscillation by recording the static wall pressure fluctuations using a miniature, 2-mm-diameter strain gauge-type transducers at numerous streamwise locations in a two-dimensional diffuser from a subsonic Mach number to Mach 1.38. The results show that both downstream-convected and upstream-propagating pressure disturbances result in maintaining the shock oscillation. Bogar (1986) adopts a two-component laser Doppler velocimeter (LDV) to measure the time evolution of the fluctuating velocity field in a supercritical, separated and transonic diffuser flows in the presence of self-sustained oscillation.

## 2.5 Shock control bump

The application of Shock Control Bump (SCB) originates in the late 1970s, during which engineers considered designing a humped transonic aerofoil to mitigate problems caused by high-shock strength and maximise the drag-divergence Mach number [Tai (1977)]. This technology was later regarded as a supercritical aerofoil, which offers a potential to improve off-design performance such as drag reduction and buffet delay. Although the experimental results have confirmed this engineering benefit, there is still significant space for further improvement. From the 2000s onwards, the direction of SCB research no longer focuses on achieving the performance benefits but concentrates on refining the understanding of the detailed flow physics that an SCB can produce to optimise the aerodynamic performance and overcome the future challenges in aviation technology. One of the greatest contributions on this is the work done by Qin et al. (2008), who has adopted a variety of 2D and 3D contour optimised bumps to reduce wave drag on transonic wings. On the experimental side, there has been a subtle shift from validation-based tests for large-scale models towards a carefully controlled environment where high-resolution local measurements are required. On the computational side, dramatic progress has been made to obtain high-quality results that contribute the physical insight into the flow mechanism. These days, many state-of-the-art projects into SCB are being conducted collectively by international partnerships who aim to create a brighter future of green aviation.

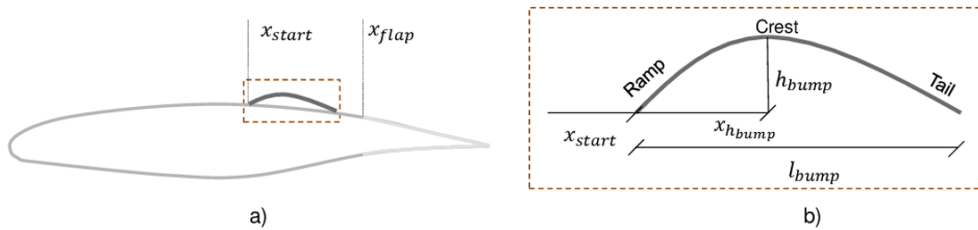


**Figure 2.4:** Schematic of a shock control bump: a) in relation with the aerofoil; b) zoom in of the bump and design parameters [Sabater and Görtz (2019)]

A conventional SCB is a bulged shape located on a wing surface where a shock wave is presented, as shown in Figure 2.4. It can have a beneficial smearing effect on the structure of the near-normal shock, achieving a reduction in wave drag through lower stagnation pressure loss. The typical geometry of an SCB comprises a ramp, a short crest region and then a tail. The ramp is generally upstream to the nominal shock position, which can generate a single oblique shock or a series of compression waves by deflecting the incoming supersonic flow to a certain angle. Over the crest region, the flow decelerates to subsonic speeds with a near-normal shock wave. The flow then travels downstream around the tail with a subsonic speed. The mode of operation of a SCB is not dissimilar to a converging-diverging duct, as used in a supersonic tunnel to decelerate from supersonic to subsonic flow downstream of the test section. SCBs can either be two or three-dimensional. Two-dimensional bumps imply that the bump profile is constant along the wing cross-section, whereas three-dimensional bumps have finite widths and can be arranged in an array along the wingspan.

### 2.5.1 Control performance

The research efforts into SCBs fall into one of the two categories: (1) Investigation that consists of parametric studies or optimisation; (2) Investigations that probe the detailed flow physics produced by SCBs in the controlled environments [Bruce and Colliss (2015)]. Tian et al. (2011) conducts a parametric analysis on improving the lift-to-drag ratio for a RAE2822 aerofoil using a bump with a Hicks-Henne profile. This study reveals that an optimum distance between the bump crest and shockwave is 30% of the bump chord; the lift-to-drag ratio increases as the bump chord increases, but decreases as the bump height increases. Yun et al. (2017) designs a forward and a backward SCB using Hicks-Henne function on a RAE2822 aerofoil. The results have shown that near the buffet onset condition, a forward bump can attenuate the shock intensity and alleviate the separation bubble at the shock foot, but no longer effective in suppressing the buffet characteristics for higher freestream Mach numbers. A backward bump performs better under a wider range of transonic flow conditions, which both decreases the downstream adverse pressure gradient and inhibits the flow separation. Ogawa et al. (2008) conducts an experimental investigation for three-dimensional bumps on transonic wings aiming to fulfil two major objectives in SBLI control, that is drag reduction and buffet delay. This method is a 3D control technique but being demonstrated as a 2D schematic shown in Figure 2.5. It is found that a double configuration of narrowly rounded bumps achieves the best performance, which considerably achieves a maximum overall drag reduction of about 30% by means of a well-established  $\lambda$ -shock structure with little viscous drag penalty. In a similar kind of way, bumps are also linked to supersonic intakes, where three-stage compression starts with an oblique shock, then a normal shock followed by an isentropic compression, reducing the total pressure loss in the wake. Birkenmeyer et al. (2000) presents a combination of 2D RANS computation and experiment to show that an SCB placed downstream to the main shock wave on a swept wing can postpone the buffet onset to higher lift coefficients. According to the review from Ashill et al. (2005), a 2D SCB may delay the onset of transonic buffet by creating an attached flow region between the shock wave and trailing edge of a supercritical wing.

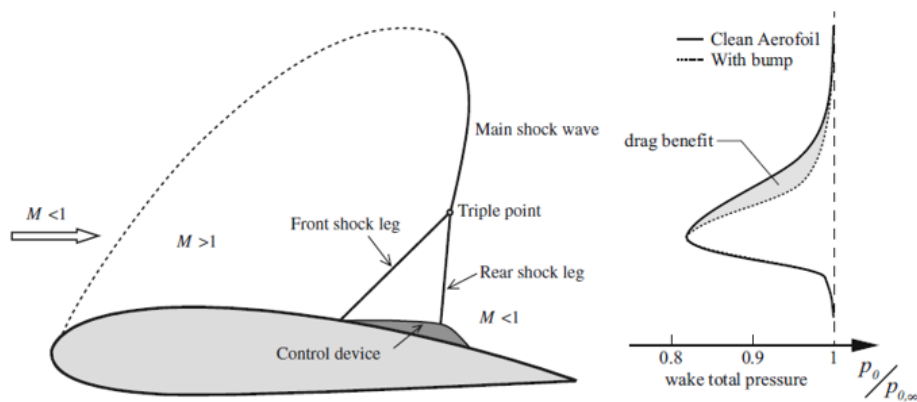


**Figure 2.5:** *Bifurcated  $\lambda$ -shock structure on a surface bump with wake total pressure profiles [Ogawa et al. (2008) & Bruce and Colliss (2015)]*

### 2.5.2 Flow structure

The flow structure produced by a SCB is highly sensitive to its location relative to the main shock position and the incoming boundary-layer state. It has been shown that variations in shock position away from this optimum location gives rise to the appearance of undesirable expansions and secondary shock systems that are detrimental to the performance of a 2D SCB. Some studies have shown that a well-designed 2D SCB generally yields negligible drawback on boundary-layer health compared to an uncontrolled case in which the rear shock position is closed to optimal. It has been demonstrated experimentally that a non-optimal rear shock location not only incurs a significant level of viscous drag, but also worsens the boundary-layer separation. However, some investigators argue that a 2D SCB still offers a positive impact on off-design performance in the ways of: (1) Breaking up large regions of separated flow to suppress interaction between an oscillating shock and an aerofoil's trailing edge; (2) Anchoring the front shock leg to keep the rear shock leg stable in the case of a straight ramp design.

It has also been demonstrated that an array of 3D SCBs can produce localised attached flows in the region downstream of the shock location. It plays the same role as mechanical VGs, creating a counter-rotating vortex pair that enhances the resilience of boundary layer Ogawa et al. (2008). In this way, the occurrence of flow breakdown due to the shock-induced separation can be postponed effectively. However, similar phenomenon will not be observed when the SCB is placed in the shock region, while it still offers a benefit in wave drag reduction.

## 2.6 Summary

The physical phenomena and mechanism in transonic buffet and the control strategy adopted in shock wave/boundary-layer interaction are reviewed from both numerical and experimental perspective. A general overview is briefly introduced in terms of the analytic interpretation of shock-induced separation, experimental approach that scrutinises the flow unsteadiness caused by shock-induced separation, and the characteristics of periodic shock oscillation that exists in various aerospace applications. The current novel passive flow control devices and techniques are reviewed, whose upsides and downsides in the control performances are summarised.

Based on this, the direction of this research aims at studying the control effectiveness of a 2D bump using CFD methods, with a particular focus on the aerodynamic responses associated with an unsteady transonic flow condition. The CFD model will be validated by comparing the numerical results with the experimental data presented on existing publications. Detailed flow physics will be analysed by applying appropriate qualitative and quantitative approach to gain an in-depth understanding about the control mechanism of a shock control bump.

## 2.7 Aim and objectives

Aim:

The aim of this research is to enhance and broaden the understanding about the physical insights into the buffet phenomena that associates with the transonic shock wave/boundary-layer interaction taking place on a 2D supercritical aerofoil, and in addition, further investigating the effect of a surface bump as a passive flow control technique that has been previously confirmed to be effective in the presence of shock wave/boundary-layer interaction.

Objectives:

- To conduct a detailed numerical investigation of the physical mechanism of transonic buffet taking place on a two-dimensional aerofoil.
- To propose an effective passive flow control technique (2D surface bump) that is functional to achieve considerable engineering benefits such as drag reduction and buffet alleviation.
- To obtain an in-depth physical insight into the control mechanism of a 2D surface bump by scrutinising a range of flowfield properties that are generated from Computational Fluid Dynamics simulations.

## 2.8 Research questions

1. How can the shock-induced buffet be controlled in the presence of a well-designed 2D bump?
2. What will be the flowfield characteristics in the presence of bump control?
3. What will be the benefits and drawbacks of using a 2D surface bump as a control device in the presence of transonic buffet flow?
4. How will the aerofoil change its aerodynamic performance in the absence/presence of a control bump?
5. Which type of bump performs the best among all the designed ones?
6. What are the advantages/drawbacks for each design in terms of the overall performance?

# Chapter 3

## Methodology

### 3.1 Governing equation

The Navier-Stokes equation describes the motion of a viscous fluid, which governs the velocity and pressure in the forms of conservation of mass, momentum and energy. *Reynolds-Averaged Navier-Stokes* (RANS) equation is generally used to analyse turbulent flows, in which all the quantities of the equation are time-averaged after dividing them into a mean and a fluctuating component using Reynolds decomposition. This concept is based on a mean and relative motion of matter argument that was raised by the British physicist Osborne Reynolds who strictly redefined the velocity components in Navier Equation that was firstly introduced in 1822. As the velocity fluctuations still appear to be a nonlinear term known as Reynolds stress, some additional equations need to be derived to close the RANS equation. That is the closure problem, which refers to a mathematical technique called turbulence modelling. A two-dimensional, compressible and high Reynolds number viscous flow is considered for this investigation. The differential form of this equation is expressed in Cartesian coordinates as follows,

Continuity:

$$\frac{\partial \rho}{\partial t} + \nabla \cdot (\rho V) = 0 \quad (3.1)$$

Momentum balance neglecting body forces in  $x$  and  $y$  direction, respectively:

$$\frac{\partial(\rho u)}{\partial t} + \frac{\partial}{\partial x}(\rho u^2) + \frac{\partial(\rho uv)}{\partial y} + \frac{\partial p}{\partial x} + \nabla \cdot (\rho u V) = \frac{\partial \tau_{xx}}{\partial x} + \frac{\partial \tau_{xy}}{\partial y} \quad (3.2)$$

$$\frac{\partial(\rho v)}{\partial t} + \frac{\partial(\rho uv)}{\partial x} + \frac{\partial(\rho v^2)}{\partial y} + \frac{\partial p}{\partial y} + \nabla \cdot (\rho v V) = \frac{\partial \tau_{xy}}{\partial x} + \frac{\partial \tau_{yy}}{\partial y} \quad (3.3)$$

With the effective stress tensors defined by

$$\tau_{xx} = 2\mu_{eff} \frac{\partial u}{\partial x} - \frac{2}{3}\mu_{eff} \left( \frac{\partial u}{\partial x} + \frac{\partial v}{\partial y} \right) \quad (3.4)$$

$$\tau_{xy} = \mu_{eff} \left( \frac{\partial u}{\partial y} + \frac{\partial v}{\partial x} \right) \quad (3.5)$$

$$\tau_{yy} = 2\mu_{eff} \frac{\partial v}{\partial y} - \frac{2}{3}\mu_{eff} \left( \frac{\partial u}{\partial x} + \frac{\partial v}{\partial y} \right) \quad (3.6)$$

Energy conservation neglecting heat transfer and the rate of work done by the body forces:

$$\begin{aligned} \frac{\partial}{\partial t} \left\{ \rho \left[ c_v T + \frac{1}{2}(u^2 + v^2) \right] \right\} + \nabla \cdot \left\{ \rho \left[ c_v T + \frac{1}{2}(u^2 + v^2) V \right] \right\} \\ = \frac{\partial}{\partial x} \left( u\tau_{xx} + v\tau_{xy} + k_{eff} \frac{\partial T}{\partial x} \right) + \frac{\partial}{\partial y} \left( u\tau_{xy} + v\tau_{yy} + k_{eff} \frac{\partial T}{\partial y} \right) \end{aligned} \quad (3.7)$$

Applying Reynolds decomposition to the velocity components  $u$  and  $v$ , and taking time averaging to Eq(3.1), Eq(3.2), Eq(3.3) and Eq(3.7), the unclosed RANS equation becomes:

$$\frac{\partial \rho}{\partial t} + \frac{\partial(\rho U)}{\partial x} + \frac{\partial(\rho V)}{\partial y} = 0 \quad (3.8)$$

$$\frac{\partial(\rho U)}{\partial t} + \frac{\partial}{\partial x}(\rho U^2) + \frac{\partial(\rho UV)}{\partial y} + \frac{\partial p}{\partial x} + \rho \left( U \frac{\partial U}{\partial x} + V \frac{\partial U}{\partial y} + \frac{\partial \bar{u}^2}{\partial x} + \frac{\partial \overline{u'v'}}{\partial y} \right) = \frac{\partial \bar{\tau}_{xx}}{\partial x} + \frac{\partial \bar{\tau}_{xy}}{\partial y} \quad (3.9)$$

$$\frac{\partial(\rho V)}{\partial t} + \frac{\partial(\rho UV)}{\partial x} + \frac{\partial(\rho V^2)}{\partial y} + \frac{\partial p}{\partial y} + \rho \left( U \frac{\partial V}{\partial x} + V \frac{\partial V}{\partial y} + \frac{\partial \bar{v}^2}{\partial x} + \frac{\partial \overline{u'v'}}{\partial y} \right) = \frac{\partial \bar{\tau}_{xy}}{\partial x} + \frac{\partial \bar{\tau}_{yy}}{\partial y} \quad (3.10)$$

$$\begin{aligned} \frac{\partial}{\partial t} \left\{ \rho \left[ c_v T + \frac{1}{2}(U^2 + V^2 + k) \right] \right\} + \nabla \cdot \left\{ \rho \left[ c_v T + \frac{1}{2}(U^2 + V^2 + k) V \right] \right\} \\ = \frac{\partial}{\partial x} \left( u\bar{\tau}_{xx} + v\bar{\tau}_{xy} + k_{eff} \frac{\partial T}{\partial x} \right) + \frac{\partial}{\partial y} \left( u\bar{\tau}_{xy} + v\bar{\tau}_{yy} + k_{eff} \frac{\partial T}{\partial y} \right) \end{aligned} \quad (3.11)$$

## 3.2 Turbulence modelling

### 3.2.1 One-equation model

The implication of turbulence modelling is a mathematical derivation of the unknown terms in the RANS equation, also known as the closure problem. The concept of turbulence was initially characterised as viscous eddies, which was firstly proposed by Boussinesq in 1877. This concept assumes that the turbulence stress is analogous to the viscous shear stress between the fluid molecules. In 1925, Prandtl presented mixing length theory that further promotes the eddy viscosity assumption, namely the zero-equation model. This model is usually recognised as *Cebeci-Smith* (C-S) model, *Baldwin-Lomax* (B-L) model and *Johnson-King* (J-K) model. Using a zero-equation model requires obtaining different eddy viscosity ratio by dividing the turbulent boundary-layer into an inner and outer layer. However, Bradshaw pointed out that a zero-equation model is incapable to capture complex flow structures such as the boundary-layer on a rotating object (e.g. wind turbine blade) or a wall surface with large curvature (e.g. blunt body), three-dimensional wake, a transverse converging and diverging shear layer, and separated and rotational flows.

A one-equation turbulence model is one transport equation coupled with the full RANS equation. The most commonly used one-equation models are *Baldwin-Barth* (B-B) model and *Spalart-Allmaras* (S-A) model. This equation is a direct representation of the eddy viscosity ratio without having to specify the inner and outer layer of a boundary-layer, as well as eliminating the need for the estimation of the maximum first layer thickness in the normal direction of a mesh. It has been demonstrated that S-A model produces good results in the prediction of shock wave and large-scale separated flow.

The S-A model was developed in 1992 by the researchers from *Boeing Commercial Airplane*, with its transport equation given by,

$$\begin{aligned} \frac{\partial \tilde{\nu}}{\partial t} + u_j \frac{\partial \tilde{\nu}}{\partial x_j} = C_{b1}(1 - f_{t2})\Omega\tilde{\nu} + \frac{M_\infty}{Re} \left\{ C_{b1}[(1 - f_{t2})f_{v2} + f_{t2}]\frac{1}{\kappa^2} - C_{w1}f_w \right\} \frac{\tilde{\nu}^2}{d^2} \\ - \frac{M_\infty}{Re} \frac{C_{b2}}{\sigma} \tilde{\nu} \frac{\partial^2 \tilde{\nu}}{\partial x_j^2} + \frac{M_\infty}{Re} \frac{1}{\sigma} \frac{\partial}{\partial x_j} \left\{ [v + (1 + C_{b2})\tilde{\nu}] \frac{\partial \tilde{\nu}}{\partial x_j} \right\} \end{aligned} \quad (3.12)$$

The turbulent dynamic viscosity is defined as

$$\mu_t = \rho \tilde{\nu} f_{v1} \quad (3.13)$$

In which

$$f_{v1} = \frac{\chi^3}{\chi^3 + C_{v1}^3} \chi \equiv \frac{\tilde{\nu}}{\nu} \quad (3.14)$$

$$f_{t2} = C_{t3} e^{-C_{t4} \chi^2} \quad (3.15)$$

$$f_w = g \left( \frac{1 + C_{w3}^6}{g^6 + C_{w3}^6} \right)^{\frac{1}{6}} \quad (3.16)$$

$$g = r + C_{w2}(r^6 - r) \quad (3.17)$$

$$r = \frac{\tilde{\nu}}{\frac{Re}{M_\infty} \tilde{S} \kappa^2 d^2} \quad (3.18)$$

$$\tilde{S} = \Omega + \frac{\tilde{\nu}}{\frac{M_\infty}{Re} \kappa^2 d^2} f_{v2} \quad (3.19)$$

$$f_{v2} = 1 - \frac{\chi}{1 + \chi f_{v1}} \quad (3.20)$$

With the model constants given by  $C_{b1} = 0.1355$ ,  $\sigma = \frac{2}{3}$ ,  $C_{b2} = 0.622$ ,  $C_{w1} = C_{b1}/\kappa^2 + (1 + C_{b2})/\sigma$ ,  $C_{v1} = 7.1$ ,  $C_{w2} = 0.3$ ,  $C_{w3} = 2.0$ ,  $C_{t3} = 1.2$ ,  $C_{t4} = 0.5$ ,  $\kappa = 0.41$ .

### 3.2.2 Two-equation model

The most popular eddy viscosity-based turbulence model is known as  $k$ - $\varepsilon$  model and its alternative forms. This is a two-equation model that is evolved from the mixing length theory. The symbol  $k$  is the turbulent kinetic energy and  $\varepsilon$  is the dissipation rate of a fluid particle. This model performs quite well in the near-wall region and a free shear flow with small adverse pressure gradient. However, the standard  $k$ - $\varepsilon$  model also has a certain level of limitation, such as the disability of predicting the anisotropy in the boundary-layer or complex turbulent flow region and the influence of vorticity. In recent years, this model was greatly improved by including wall functions to correct the low Reynolds number effect in the near-wall region. A number of nonlinear  $k$ - $\varepsilon$  models were developed, such as the RNG  $k$ - $\varepsilon$  model and Realizable  $k$ - $\varepsilon$  model. The transport equations for a Realizable  $k$ - $\varepsilon$  model are written as follows, respectively:

$$\frac{\partial k}{\partial t} + u_j \frac{\partial k}{\partial x_j} = \frac{\partial}{\partial x_j} \left[ \left( \nu + \frac{\nu_t}{\sigma_k} \right) \frac{\partial k}{\partial x_j} \right] - \overline{u'_i u'_j} \frac{\partial u_i}{\partial x_j} - \varepsilon \quad (3.21)$$

$$\frac{\partial \varepsilon}{\partial t} + u_j \frac{\partial \varepsilon}{\partial x_j} = \frac{\partial}{\partial x_j} \left[ \left( \nu + \frac{\nu_t}{\sigma_\varepsilon} \right) \frac{\partial \varepsilon}{\partial x_j} \right] - C_{\varepsilon 1} \frac{\varepsilon}{k} \overline{u'_i u'_j} \frac{\partial u_i}{\partial x_j} - C_{\varepsilon 2} \frac{\varepsilon^2}{k} \quad (3.22)$$

Another common two-equation turbulence model is known as  $k$ - $\omega$  model, which was developed by Wilcox in 1988, who introduced a term called specific rate of dissipation  $\omega$ . This model aims to improve the limitation of low Reynolds number flow near the wall. A  $k$ - $\omega$  model possesses a good numerical stability in the buffer layer and does not require an explicit wall function. Furthermore, *Menter* develops a Shear-Stress-Transport (SST)  $k$ - $\omega$  model by combining the near-wall stability and adverse pressure gradient sensitivity of a standard  $k$ - $\omega$  model, and the outer boundary-layer independence of a standard  $k$ - $\varepsilon$  model. This model uses Wilcox  $k$ - $\omega$  model in the boundary-layer edges, and a standard  $k$ - $\varepsilon$  model in the free-shear-layers. Therefore, SST  $k$ - $\omega$  model produces more accurate and reliable results than the standard  $k$ - $\omega$  model. The transport equation for a SST  $k$ - $\omega$  model is expressed as,

$$\frac{\partial k}{\partial t} + u_j \frac{\partial k}{\partial x_j} = \frac{1}{\rho} P_k - \beta k \omega + \frac{1}{\rho} \frac{\partial}{\partial x_j} \left[ \left( \mu + \frac{\mu_t}{\sigma_k} \right) \frac{\partial k}{\partial x_j} \right] \quad (3.23)$$

$$\frac{\partial \omega}{\partial t} + u_j \frac{\partial \omega}{\partial x_j} = \frac{1}{\rho} P_\omega - \beta \omega^2 + \frac{1}{\rho} \frac{\partial}{\partial x_j} \left[ \left( \mu + \frac{\mu_t}{\sigma_\omega} \right) \frac{\partial \omega}{\partial x_j} \right] \quad (3.24)$$

where,

$$\mu_t = \frac{\rho k}{\omega} \quad (3.25)$$

$$P_k = \mu_t \Omega^2 \quad (3.26)$$

$$P_\omega = \gamma \rho \Omega^2 \quad (3.27)$$

### 3.3 Design of bump configurations

As mentioned in Section 2.5, a conventional 2D bump geometry consists of three elements: a ramp, a short crest and a tail. All these elements are represented by a straight line. The ramp and the tail are connected to the aerofoil surface by a circular arch with a positive radius of curvature, while the corners on the bump profile are a segment of a circle whose radius of curvature is negative. The bump geometry has three degrees of freedom, which are the ramp angle, the crest height and the chord length, as shown on Figure 3.1. To start with, a default forward and a backward bump are implemented on an OAT15A supercritical aerofoil, as shown schematically in Figure 3.2. There are some smaller and larger bumps that are not shown in this figure but with given dimensions presented in Table 3.1 and 3.2. Figure 3.4 presents four bump configurations placed at a forward location ( $x/c=30\%$ ), while Figure 3.5 presents the ones at a backward location ( $x/c=40\%$ ). The ramp angle, the crest height and the chord length for each design are listed in Table 3.1 and 3.2, and the parameters shown in Figure 3.1 are defined as follows:  $r_1 = 6.4 / \tan \frac{\theta_1}{2}$ ,  $r_2 = a'_2 / \tan \frac{\theta_2}{2}$ ,  $r_3 = a'_3 / \tan \frac{\theta_2}{2}$ ,  $r_4 = 6.4 / \tan \frac{\theta_2}{2}$ , where  $a'_2 = 6.4 / (1 + \cos \theta_1)$ ,  $a'_3 = 6.4 / (1 + \cos \theta_2)$ .

The aerofoil on which the bumps locate is an OAT15A supercritical aerofoil, which has a chord length of 230 mm, a thickness-to-chord ratio of 12.5% and a thick trailing edge of 0.5% of the chord length. This aerofoil is a base model that has been examined experimentally through wind tunnel tests, and its geometry is shown explicitly in Figure 3.6(b). The air passing around the aerofoil is considered to be an ideal gas, with a static pressure of 101325 kPa and a static temperature of 300 K. The freestream flow is a Mach number 0.73 and a  $3.5^\circ$  angle of attack, and a Reynolds number based on chord length  $3 \times 10^6$ .

Long and high-crest bump		
Ramp angle	Crest height	Chord length
$\theta_1=5.2^\circ$	$h_B/c=0.935\%$	$l_B/c=46.1\%$
Long and low-crest bump		
Ramp angle	Crest height	Chord length
$\theta_1=2.6^\circ$	$h_B/c=0.482\%$	$l_B/c=45.3\%$
Short and high-crest bump		
Ramp angle	Crest height	Chord length
$\theta_1=5.2^\circ$	$h_B/c=0.925\%$	$l_B/c=28.2\%$
Short and low-crest bump		
Ramp angle	Crest height	Chord length
$\theta_1=1.3^\circ$	$h_B/c=0.146\%$	$l_B/c=18.0\%$

**Table 3.1:** Forward bump parameters( $x/c=30\%$ )

Long and high-crest bump		
Ramp angle	Crest height	Chord length
$\theta_1=2.8^\circ$	$h_B/c=0.602\%$	$l_B/c=22.5\%$
Long and low-crest bump		
Ramp angle	Crest height	Chord length
$\theta_1=1.4^\circ$	$h_B/c=0.460\%$	$l_B/c=22.9\%$
Short and high-crest bump		
Ramp angle	Crest height	Chord length
$\theta_1=2.8^\circ$	$h_B/c=0.602\%$	$l_B/c=17.1\%$
Short and low-crest bump		
Ramp angle	Crest height	Chord length
$\theta_1=1.4^\circ$	$h_B/c=0.438\%$	$l_B/c=15.9\%$

**Table 3.2:** Backward bump parameters( $x/c=40\%$ )

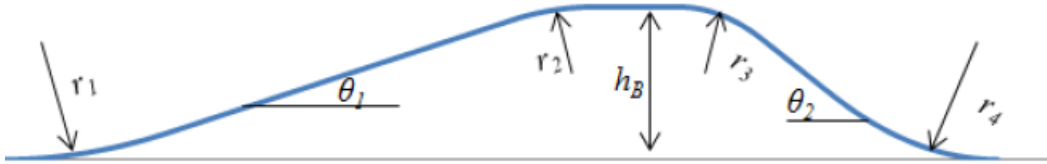


**Figure 3.1:** Geometrical feature of a standard bump(not to scale)

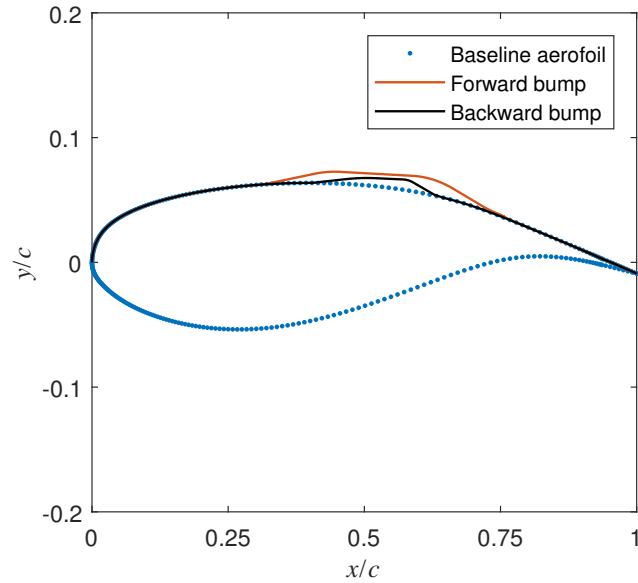


**Figure 3.2:** Schematic of a baseline aerofoil with bump(not to scale)

The turn angle of the bump ramp needs to be estimated by applying the compressible aerodynamics theory. For an oblique shock wave, four theoretical relations are shown in Figure 3.3, which are the shock angle, oblique shock downstream Mach number, static pressure and stagnation pressure ratio with respect to the flow deflection angle. It can be determined that the Mach number upstream to a normal shock wave over an aerofoil can be up to 1.37 or 1.38, for a freestream transonic Mach number that is marginally below and above 0.73. Based on these relations, in order to achieve a weak shock solution and avoid detached shock, the flow deflection angle should satisfy the following conditions: the maximum flow deflection angle should not exceed 9 degrees; downstream Mach number should remain supersonic; an optimum range of deflection angle should be determined to achieve a minimum pressure jump and total pressure loss through an oblique shock.

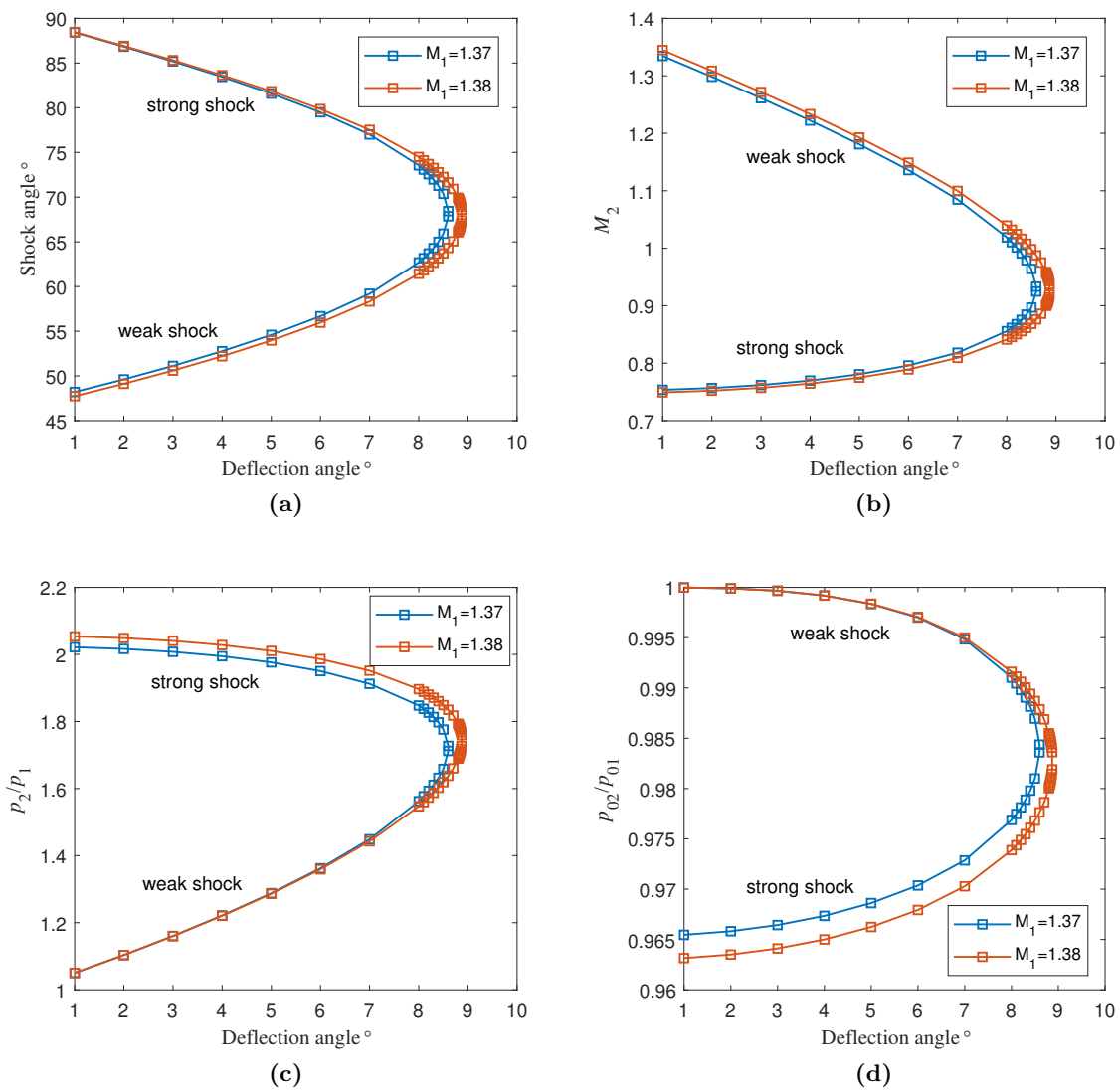
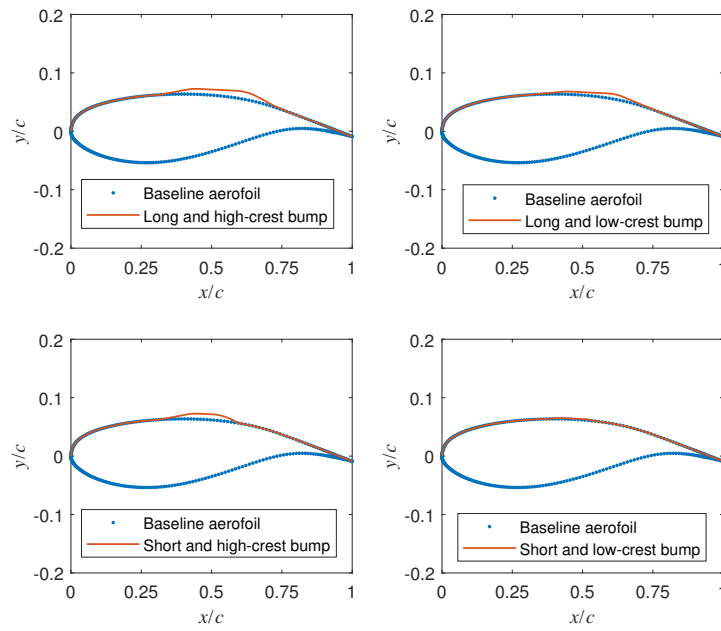
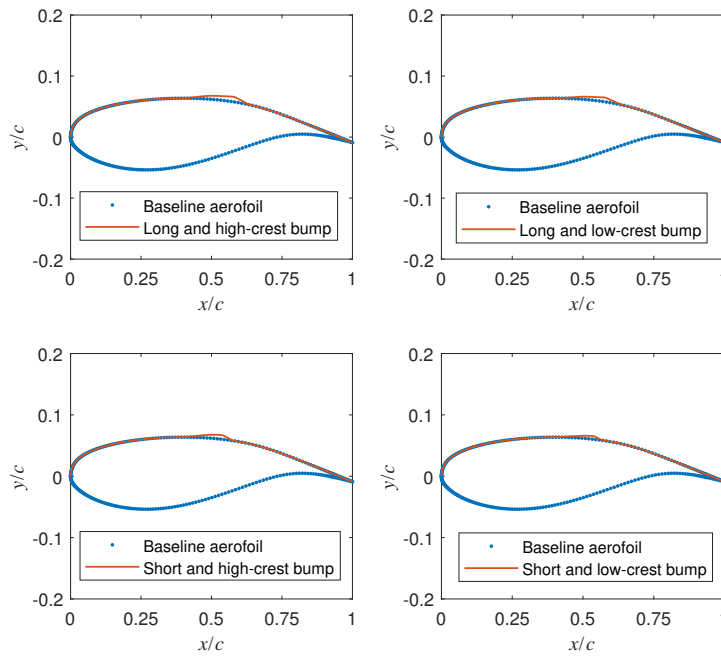


Figure 3.3: Theoretical oblique shock relations in transonic flow conditions



**Figure 3.4:** Schematic of different bump geometries (Forward position)



**Figure 3.5:** Schematic of different bump geometries (Backward position)

### 3.4 Numerical method

A first-order implicit dual-time marching scheme is chosen to be the numerical approach for transient computation. This approach is relatively more stable than an explicit scheme over a much larger value of time step with less computer time, but it can result in larger truncation error. However, for a time-dependent variable of which a steady-state solution is desired, the relative timewise accuracy becomes unimportant. An implicit finite-difference method has computationally reproduced the Tijdeman (1977) experimental observation of shock wave oscillation on an aerofoil in unsteady and transonic flow, as discussed by Ballhaus and Goorjian (1977).

The spatial discretisation for the governing equation is a second-order upwind scheme, and the flow domain is constructed by a C-grid topology. No-slip wall and pressure far-field boundary conditions are applied on the aerofoil surface and the C-grid domain, respectively.

A dual-time marching scheme is a fully implicit time-stepping scheme using a multi-grid approach. This scheme pays off the need for large variations in mesh size, of which the use of an explicit scheme would result in a very severe restriction on the time step [Jameson (1991)]. This method has been testified to be suitable with applications to unsteady flow past aerofoils and wings.

The *Jameson* time-stepping scheme is derived based on the spatial discretisation of *Navier-Stokes* equation expressed in curvilinear Cartesian coordinates, that is

$$\frac{\partial w}{\partial t} + \frac{\partial f_i(w)}{\partial x_i} = 0 \quad (3.28)$$

where  $w = \begin{bmatrix} \rho \\ \rho u_1 \\ \rho u_2 \end{bmatrix}$  and  $f_i = \begin{bmatrix} \rho u_i \\ \rho u_1 u_i + p \delta_{1i} \\ \rho u_2 u_i + p \delta_{2i} \end{bmatrix}$  represent the vectors of dependent variables.

Using a second order three-point rearward difference operator to Eq(3.28) yields

$$J^{-1} \frac{3w^{n+1} - 4w^n + w^{n-1}}{2\Delta t} + R(w^{n+1}) = 0 \quad (3.29)$$

where  $J^{-1}$  is Jacobi matrix and  $R(w)$  is the residual between the fluxes through a cell face. Adding an imaginary time derivative to the left hand side of Eq(3.29), and applying a first-order forward difference operator yields

$$J^{-1} \frac{w^{p+1} - w^p}{\Delta \tau} + J^{-1} \frac{3w^{n+1} - 4w^n + w^{n-1}}{2\Delta t} + R(w^{n+1}) = 0 \quad (3.30)$$

where  $\Delta\tau$  is the imaginary time step with first order accuracy and  $\Delta t$  is the physical time step with second order accuracy;  $p$  is the number of iteration of imaginary time step and  $n$  is the number of iteration of physical time step, respectively.

As Eq(3.30) converges on an imaginary timeline, the term  $J^{-1} \frac{w^{p+1}-w^p}{\Delta\tau} = 0$ , hence an unsteady solution with second order accuracy can be produced. A steady-state solution can be obtained with Eq(3.30) by adopting several well-developed fast convergence method, such as local time stepping method and multi-grid technology.

### 3.5 Mesh and time step independence study

A flow domain with a different number of cells has been examined to obtain a solution that is independent of the mesh resolution. For a single mesh grid, the convergence criterion is expected to be below order of  $10^{-5}$  for the continuity, momentum and energy residuals, and a steady-state solution of the lift and drag coefficients are chosen to check the history of convergence. A complete mesh independence study is carried out in the following steps:

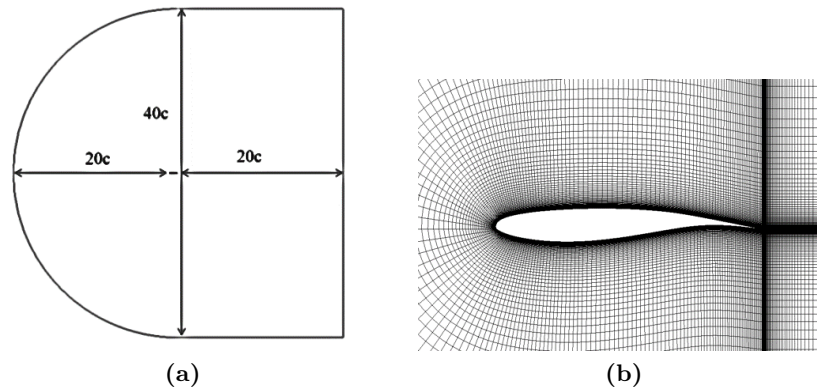


**Figure 3.6:** (a) Farfield domain and (b) structured mesh around an OAT15A aerofoil

Step 1: Perform a calculation with the initial mesh and ensure the convergence criterion is met, and the imbalances of lift and drag monitors need to be lower than 1%.

Step 2: Once the residual errors satisfy the requirement of the first calculation, refine the mesh globally throughout the domain. A factor of 1.5 times as the initial mesh size is preferred.

Step 3: Calculate the solution again for the refined mesh. Check the sensitivity of the resultant values. If this value is within an allowable tolerance (1% error) with the first value, then the mesh size in Step 1 is accurate enough to reach a reliable result. If not, the mesh should be refined more until the solution is within an acceptable range of tolerance.

Step 4: Plot a graph to show the relationship between the monitor values and their corresponding mesh cells. An optimum number of cells can be identified as the monitor no longer varies with the incremental change of cells. At this point, the mesh independence study is done and a converged mesh resolution can be used for the subsequent numerical analysis.

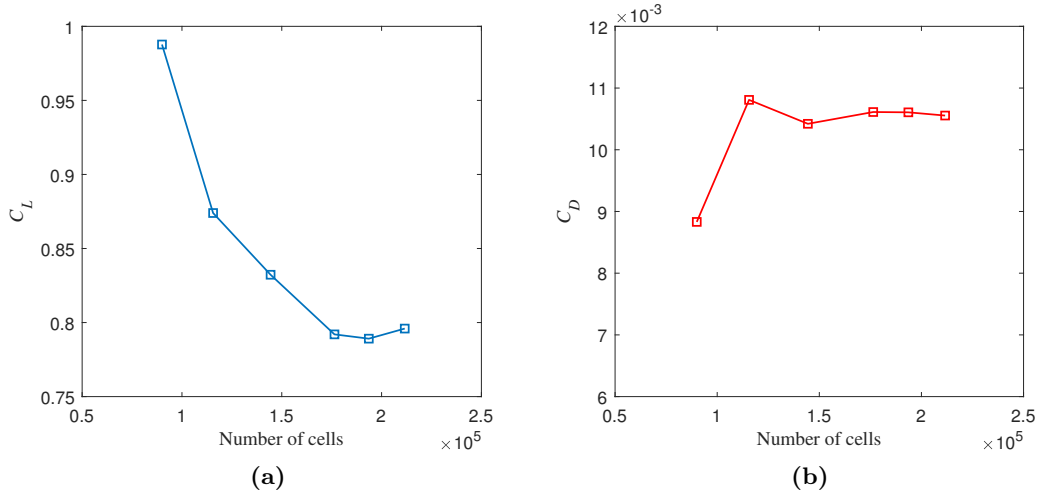


**Figure 3.7:** Mesh independence studies of (a) lift and (b) drag coefficients for a baseline aerofoil ( $M_\infty=0.73$ ,  $\alpha=3.5^\circ$ )

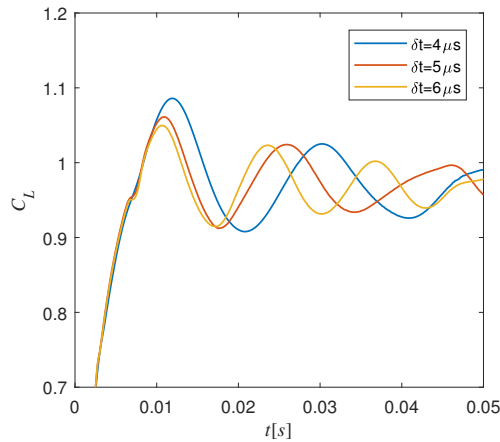


**Figure 3.8:** Time responses of lift coefficient for various time steps ( $M_\infty=0.73$ ,  $\alpha=3.5^\circ$ )

After the mesh resolution is converged, a suitable time step size should be determined for the analysis of transient computation. The lift and drag coefficients against the mesh densities are presented in Figure 3.7, indicating that the solution starts to converge at approximately 200,000 cells. The determination of a converged time step size is relatively more straightforward than the mesh cells, meaning that the transient solution is independent of the change of time step sizes. According to the existing literature on the transient numerical studies, an

acceptable range of time step size is between  $1\mu\text{s}$  to  $10\mu\text{s}$ . Figure 3.8 shows a time response of lift coefficient for a baseline aerofoil with different time steps. As the time step decreases, the lift oscillation becomes more and more damped with a gradually compressed angular frequency and amplitude. This behaviour indicates that a transient solution of URANS equation is sensitive to the time step and it directly affects the accuracy of the unsteady solution. The frequencies of oscillation at different Mach number are compared with the results obtained from global-stability theory and the wind tunnel experiment, as shown in Figure 3.9.

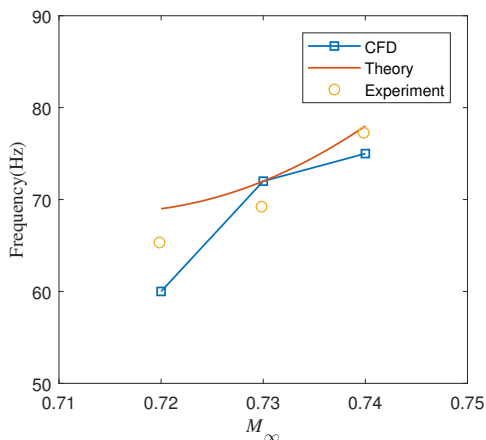


**Figure 3.9:** Buffet-onset frequencies for CFD, theory and experiment ( $\alpha=3.5^\circ$ )

## 3.6 Sensitivity of turbulence models

### 3.6.1 Aerofoil without control

A sensitivity study using different turbulence models and angle of attack is conducted based on the mesh resolution obtained from the mesh independence study. The pressure distribution on the aerofoil surface is plotted, as shown in Figure 3.10. The pressure profiles for two angles of attack are compared with the experimental data measured by the S3 Wind Tunnel in *ONERA Chalais-Meudon*. These pressure profiles indicate that the shock wave can move upstream to the oncoming flow for an increased angle of attack. At  $2.5^\circ$  angle, the numerical result shows a relatively good agreement with the measured values in terms of the supersonic flow region, the aerofoil's lower surface and the trailing edge. At  $3^\circ$  angle, the pressure downstream to the shock wave no longer matches well with experiment due to a more detached boundary-layer in the post-shock region. For the sensitivity of turbulence models, it can be seen clearly that Realizable  $k-\epsilon$  model indicates the best alignment with the experimental data measured by the S3 Wind Tunnel in *ONERA Chalais-Meudon*, including the supersonic flow region and the shock location, as well as the lower surface of the aerofoil. It can also be observed that this model shows a relatively good agreement in the post-shock region near the trailing edge.

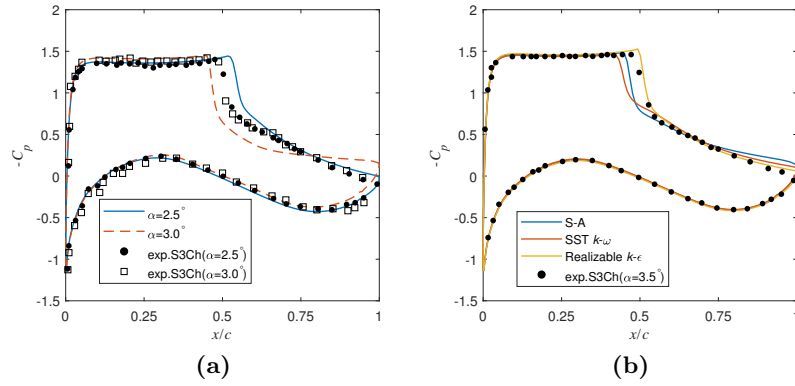


**Figure 3.10:** Pressure profiles for different (a) angles of attack and (b) turbulence models ( $M_\infty=0.73$ )

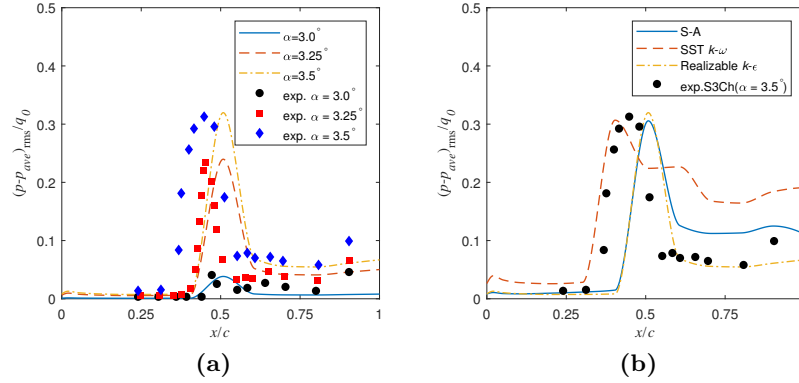


**Figure 3.11:** Root-Mean-Squared pressure fluctuations for different (a) angles of attack and (b) turbulence models ( $M_\infty=0.73$ )

The distribution of unsteady pressure fluctuation along the upper surface of the aerofoil is computed. The time-dependent pressure variations are the averaged values of the difference between the mean and fluctuating component of static pressure, namely the Root-Mean-Square (RMS) pressure fluctuation. Figure 3.11 shows the distribution of RMS fluctuation along the aerofoil’s upper surface with different turbulence models and angle of attack. It can be easily identified from Figure 3.11(b) that the maximum pressure fluctuation appears at  $x/c=45\%$ (experiment),  $x/c=40\%$ (SST  $k-\omega$ ),  $x/c=51\%$ (*Spalart-Allarmas* and Realizable  $k-\epsilon$ ), of which the maximum RMS fluctuation seen to be approximately between 30% to 35%. In particular, Realizable  $k-\epsilon$  model shows a relatively good agreement with the experimental measurements in terms of the supersonic flow region from  $x/c=24\%$  to  $x/c=42\%$ , as well as a point located at  $x/c=81\%$  on the trailing edge.

Figure 3.12 presents the wall shear stress distributions for different angles of attack and turbulence models. The magnitude of shear stress is non-dimensionalised into skin friction coefficient. Similar to the surface pressure, the shock location indicated by the shear stress also moves forward as the angle of attack increases. For a flow incidence below  $3.5^\circ$ , the wall

shear stress downstream to a shock wave remains positive even though an adverse pressure gradient is present in the boundary-layer. For the shear stresses computed by different turbulence models with a fixed angle of attack, the shear stresses in the supersonic flow upstream of the shock wave do not match very well regardless of the marginal error shown by the main shock location, as well as the pressure side of the aerofoil even though it is shock-free. It is evident that in the presence of transonic shock wave/boundary-layer interaction, the flow behind the shock wave tends to separate and detach from the wall, making the boundary-layer thicker and hence much lower shear stress. Given that the *Spalart-Allarmas* and SST  $k-\omega$  models are not coupled with a wall function, Realizable  $k-\epsilon$  model with a scalable wall function is able to capture a boundary-layer that is much closer to the onset of separation.

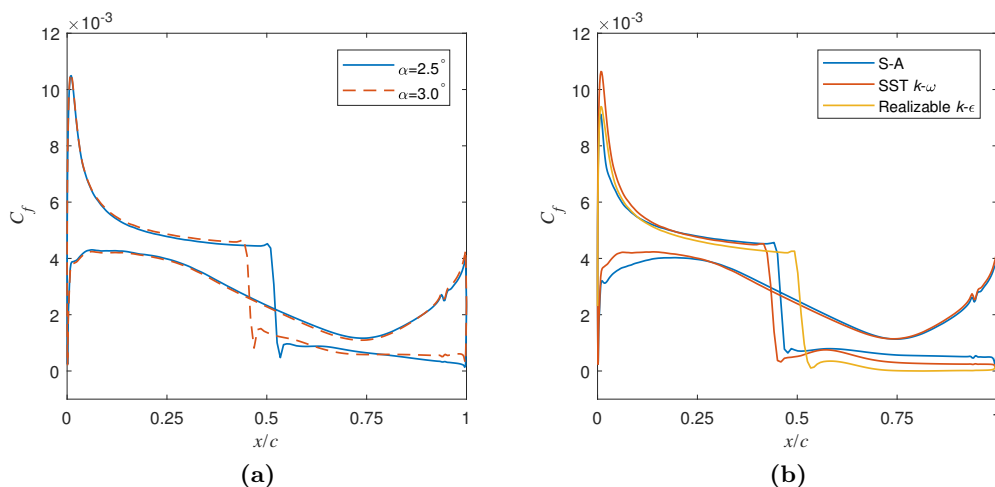
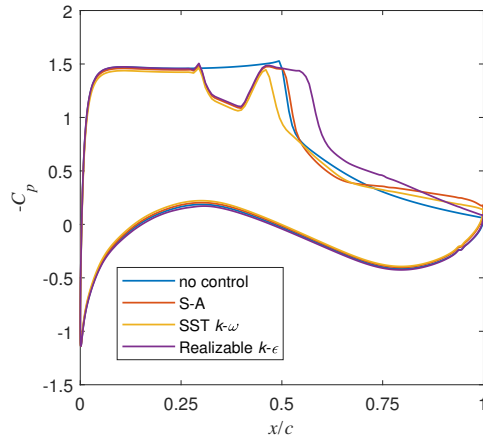


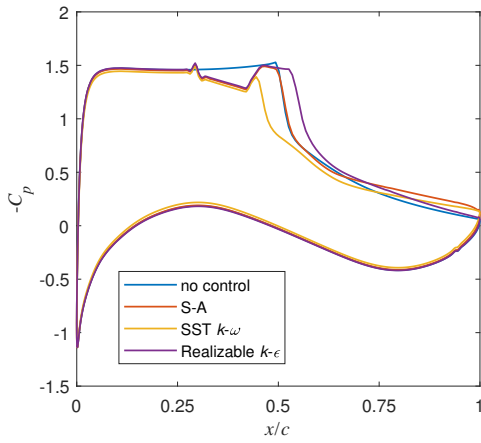
**Figure 3.12:** Wall shear stress for different (a) angles of attack and (b) turbulence models ( $M_\infty=0.73$ )

### 3.6.2 Aerofoil with control

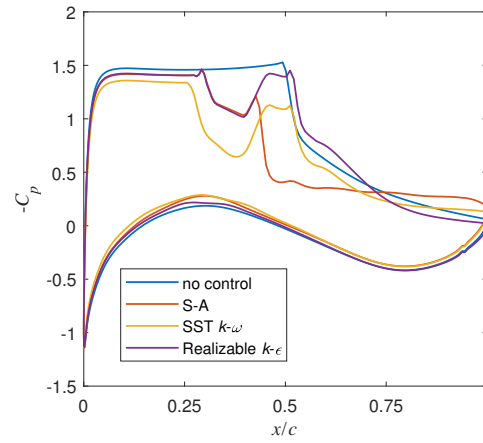
The pressure distributions for the aerofoils with different bump configurations are obtained with the turbulence models used in Section 3.6.1, as compared with the uncontrolled case. Figure 3.13 shows the surface pressure distributions for the forward bumps. For a forward long and high-crest bump, the pressure rise across an oblique shock wave created by the conjunction between the aerofoil surface and the bump ramp is accurately predicted. As the flow passes along the ramp, a linear pressure profile is created, which can be observed from  $x/c=33\%$  to  $x/c=40\%$  chord length. This implies that a reduced Mach number downstream to a shock wave causes an adverse pressure gradient. Similarly, the forward long and low-crest bump creates a longer linear pressure profile from  $x/c=32\%$  to  $x/c=42\%$ . It can be observed that the secondary compression waves created by long and high-crest bump are located at  $x/c=51\%$  (*Spalart-Allarmas*),  $x/c=46\%$  (SST  $k-\omega$ ) and  $x/c=55\%$  (Realisable  $k-\epsilon$ ). For a forward long and low-crest bump, the rear shock leg position is  $x/c=50\%$  (*Spalart-Allarmas*),  $x/c=44\%$  (SST  $k-\omega$ ) and  $x/c=53\%$  (Realisable  $k-\epsilon$ ). Alternatively, the forward bumps with shorter chord length and lower crest height are also assessed numerically with different turbulence models. Likewise, the short and high-crest bump also creates two pressure rises in the streamwise direction.



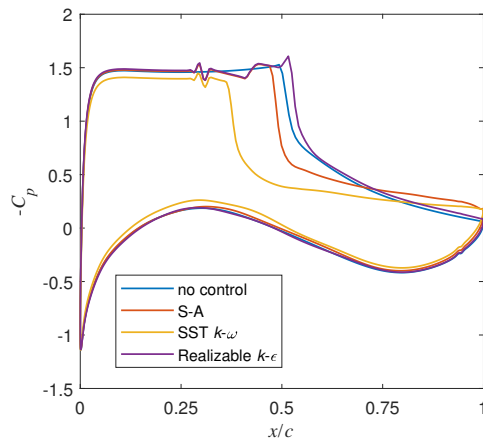
(a) Long and high-crest bump



(b) Long and low-crest bump

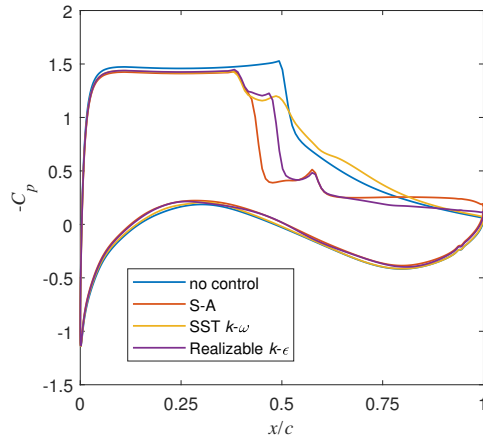


(c) Short and high-crest bump

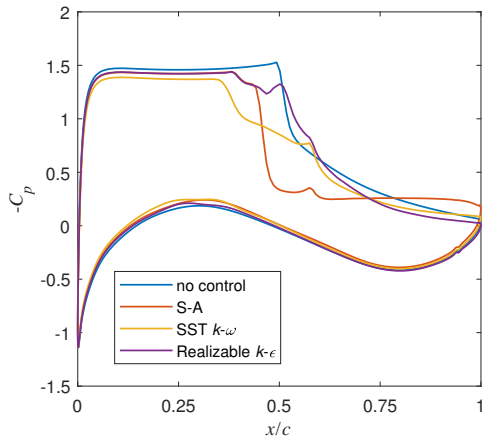


(d) Short and low-crest bump

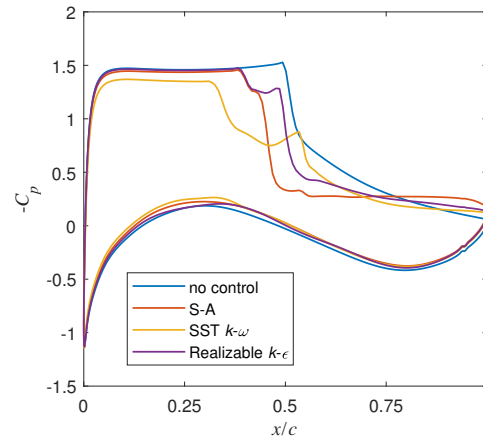
**Figure 3.13:** Pressure profiles for forward bumps with different turbulence models ( $M_\infty=0.73$ ,  $\alpha=3.5^\circ$ )



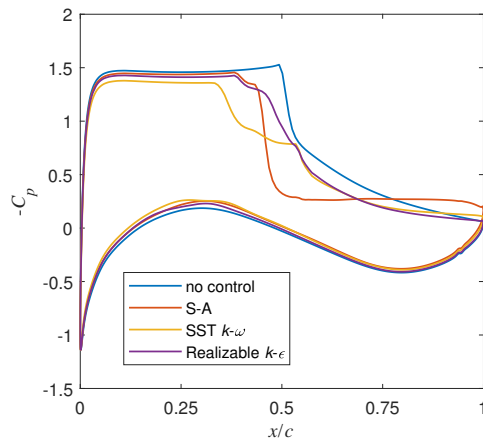
(a) Long and high-crest bump



(b) Long and low-crest bump

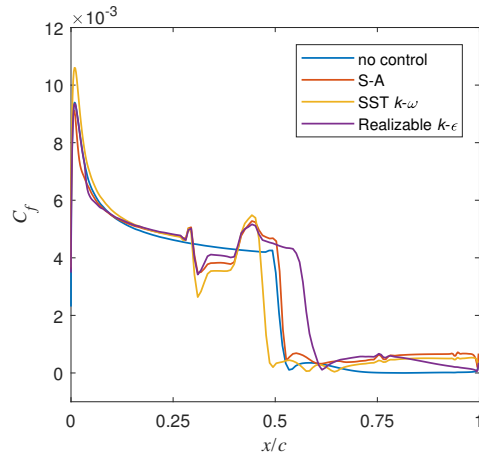


(c) Short and high-crest bump

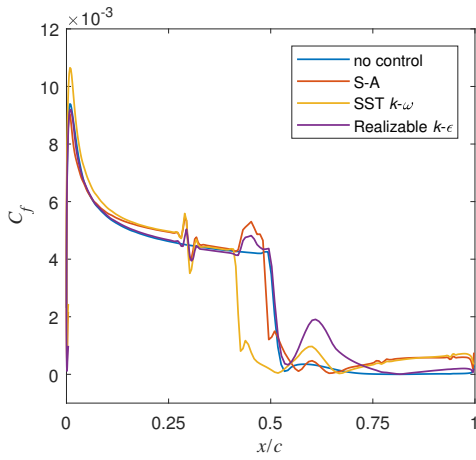


(d) Short and low-crest bump

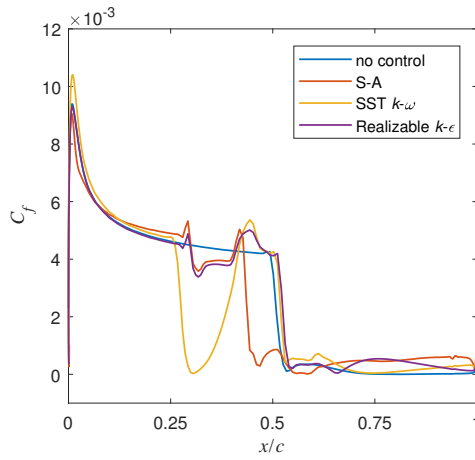
**Figure 3.14:** Pressure profiles for backward bumps with different turbulence models ( $M_\infty=0.73$ ,  $\alpha=3.5^\circ$ )



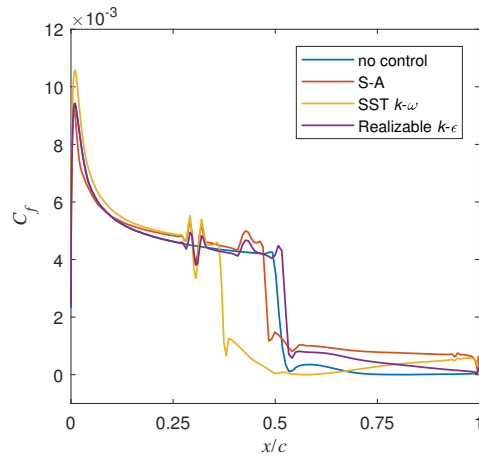
(a) Long and high-crest bump



(b) Long and low-crest bump

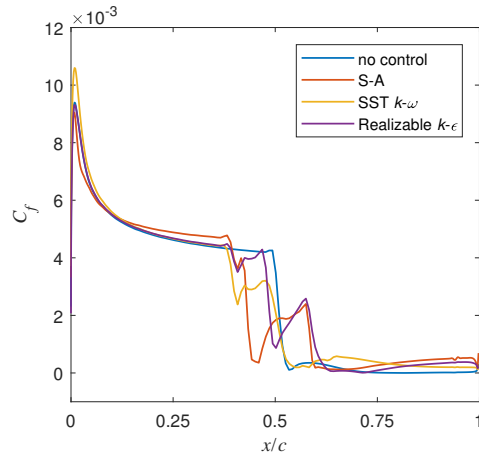


(c) Short and high-crest bump

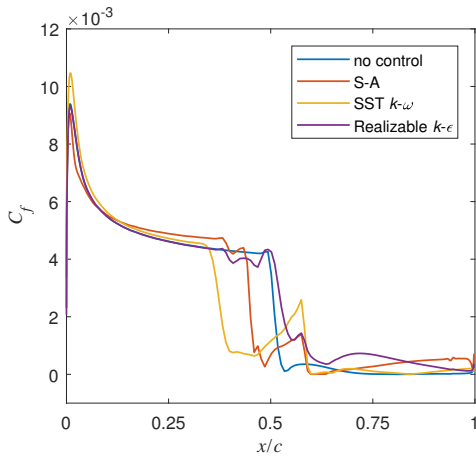


(d) Short and low-crest bump

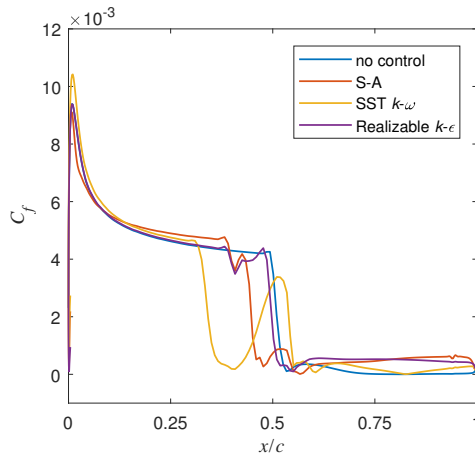
**Figure 3.15:** Upper surface shear stress distributions for forward bumps with different turbulence models ( $M_\infty=0.73$ ,  $\alpha=3.5^\circ$ )



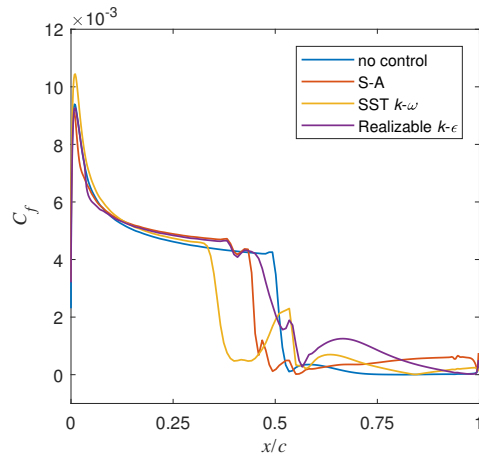
(a) Long and high-crest bump



(b) Long and low-crest bump



(c) Short and high-crest bump



(d) Short and low-crest bump

**Figure 3.16:** Upper surface shear stress distributions for backward bumps with different turbulence models ( $M_\infty=0.73$ ,  $\alpha=3.5^\circ$ )

The first pressure rise occurs at  $x/c=29\%$  (*Spalart-Allarmas* and Realisable  $k-\epsilon$ ), and  $x/c=26\%$  (SST  $k-\omega$ ). The second pressure rise locates at  $x/c=43\%$  (*Spalart-Allarmas*),  $x/c=51\%$  (SST  $k-\omega$  and Realisable  $k-\epsilon$ ). For a forward short and low-crest bump, a tiny pressure rise and drop is created due to a very low ramp angle, whereas the locations of the secondary pressure rise generated by the shock wave differs from one another, that are  $x/c=48\%$  (*Spalart-Allarmas*),  $x/c=36\%$  (SST  $k-\omega$ ) and  $x/c=52\%$  (Realisable  $k-\epsilon$ ). The pressure distributions for the backward bumps with different turbulence models are also computed and shown in Figure 3.14. The pressure rise points created by these bumps are shifted to a forward position relative to a baseline aerofoil, which implies that the backward bumps generate early adverse pressure gradients downstream to the supersonic flow region. For a backward long and high-crest bump, all three turbulence model predicts that the adverse pressure gradient occurs at  $x/c=38\%$ , whereas the adverse pressure gradient predicted by Realisable  $k-\epsilon$  model is earlier than the other two models for the rest of three bumps.

Figure 3.15 and 3.16 are the wall shear stress distributions on the aerofoil's upper surface for each bump configuration. It can be observed that the results are highly sensitive to the turbulence models. For a forward long and high-crest bump, the separation point predicted by SST  $k-\omega$  model is shifted to a forward location of  $x/c=48\%$ , while the location for Realisable  $k-\epsilon$  model is lagged to  $x/c=61\%$ . For a long and low-crest bump, all models predict that the separation point locates at  $x/c=53\%$ . It is also noteworthy to observe that a small region of flow reattachment is created between  $x/c=53\%$  and  $66\%$  on a forward long and low-crest bump. For a forward short and high-crest bump, the location of the separation point moves to  $x/c=47\%$  (*Spalart-Allarmas*) and  $54\%$  (Realisable  $k-\epsilon$ ). For a short and low-crest bump, the Realisable  $k-\epsilon$  model shows a separation point located at  $x/c=38\%$ , while the locations of separation for *Spalart-Allarmas* and Realisable  $k-\epsilon$  models are found to be around  $x/c=50\%$ .

For the backward bumps, as shown in Figure 3.15, the change of separation locations and boundary-layer status become even more complex. All bumps create a flow reattachment zone in which a positive gradient of shear stress occurs. The backward bumps create a flow reattachment that spans from  $x/c=46\%$  to  $58\%$  (long and high-crest),  $x/c=46\%$  to  $57\%$  (long and low-crest),  $x/c=41\%$  to  $52\%$  (short and high-crest) and  $x/c=44\%$  to  $53\%$  (short and low-crest). It is found that SST  $k-\omega$  predicts earlier onset of flow detachment on a backward short bump than the long bumps.

# Chapter 4

## Results

### 4.1 Flowfield properties

#### 4.1.1 Mach number distribution

##### No control

In the study of compressible gas dynamics, it is necessary to identify the shock wave that exists in the mixture of locally subsonic and supersonic flow. In the real world, the feature of a compressible flow can be experimentally visualised by conducting a shadowgraph technique called *Schlieren* Imaging. Since this technique requires physical wind tunnel facility, CFD simulation can be relatively easier and less expensive to visualise compressible flow by computing the distribution of Mach number in a flowfield. Unsteady RANS simulations with zero second initial condition are conducted to obtain the flowfields.

Figure 4.1 presents the Mach number distribution around an aerofoil without bump control (hence clean surface). The flow condition, in this case, is a freestream Mach number 0.73 and an angle of attack  $3.5^\circ$ , which is a typical onset condition of the buffet that has been investigated extensively. At the initial state of the simulation  $t=0.05T$  ( $T$ =period of shock-induced oscillation), the shock wave locates at a position of  $x/c=45\%$ , at which a separation bubble is formed at the shock foot, indicative of the streamline tracers. This separation bubble creates circulation that leads to flow separation. The shock then starts moving towards a upstream (left) direction at  $t=0.25T$ , stopping at the most downstream shock location  $x/c=42\%$ . During this movement, the boundary-layer becomes thinner and less detached to the aerofoil surface, making the separation bubble smaller. Later, at  $t=0.45T$ , the shock moves to the downstream direction (right) and reaches to a location of  $x/c=0.49\%$ , where the boundary-layer downstream to the shock wave reattaches to the surface, creating the least separation bubble at the shock foot. At  $t=0.65T$ , the shock wave reaches a position where the separation bubble starts to develop at the shock foot, and it continues to expand as the shock moving downstream.

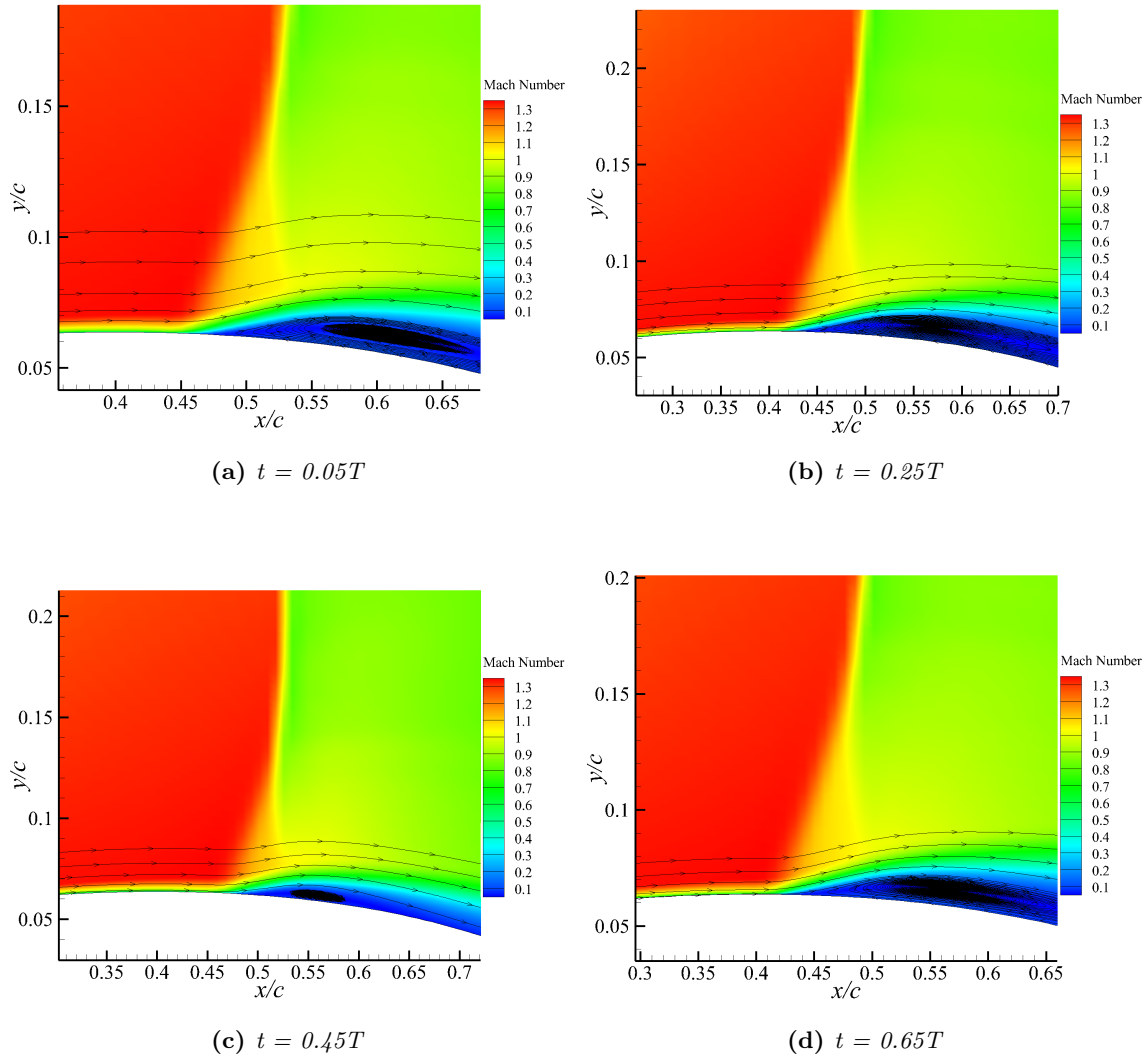


**Figure 4.1:** Transient Mach number contour on an aerofoil without control ( $M_\infty=0.73$ ,  $\alpha=3.5^\circ$ )

### With control

Figure 4.2 presents the full-view snapshots of the Mach number distribution around the aerofoils with the forward bumps, while Figure 4.3 presents the zoom-in view snapshots of the Mach number distribution near the bump region. It can be seen from Figure 4.3(a) that a forward long and high-crest bump creates an oblique shock wave locating at  $x/c=33\%$ , and the downstream Mach number is between 1.1 and 1.2. A supersonic flow zone is recreated over the crest region due to flow re-acceleration. This additional supersonic flow incurs a secondary  $\lambda$ -shock system with a front shock leg locating at  $x/c=41\%$  and a rear shock leg at  $x/c=49\%$ . Although an adverse pressure gradient exists at this location, the flow in the post-shock region remains attached to the surface because of the low wall curvature on the bump

profile. As shown in Figure 4.3(b), a forward long and low-crest bump creates a relatively weaker oblique shock at the bump leading edge, with a downstream Mach number in the verge between 1.3 and 1.2. This is due to a lower ramp angle of a low-crest bump. A secondary oblique shock also occurs on the bump crest, with a location of  $x/c=43\%$ . As indicated by Figure 4.3(c), a forward short and high-crest bump creates an oblique shock wave with the equal strength and the same location as the long and high-crest bump due to the same ramp angle. However, a relatively larger flow re-expansion is created and propagates farther downstream than the long and high-crest bump, leading to a higher adverse pressure gradient on the bump tail. As can be seen from Figure 4.3(d), the oblique shock created by a forward short and low-crest bump is barely visible due to a very tiny ramp angle and a crest height of the bump, but it is assumed that a very weak  $\lambda$ -shock structure is existent in the flowfield with a front shock leg locating at  $x/c=33\%$  and a rear shock leg locating at  $x/c=43\%$ .

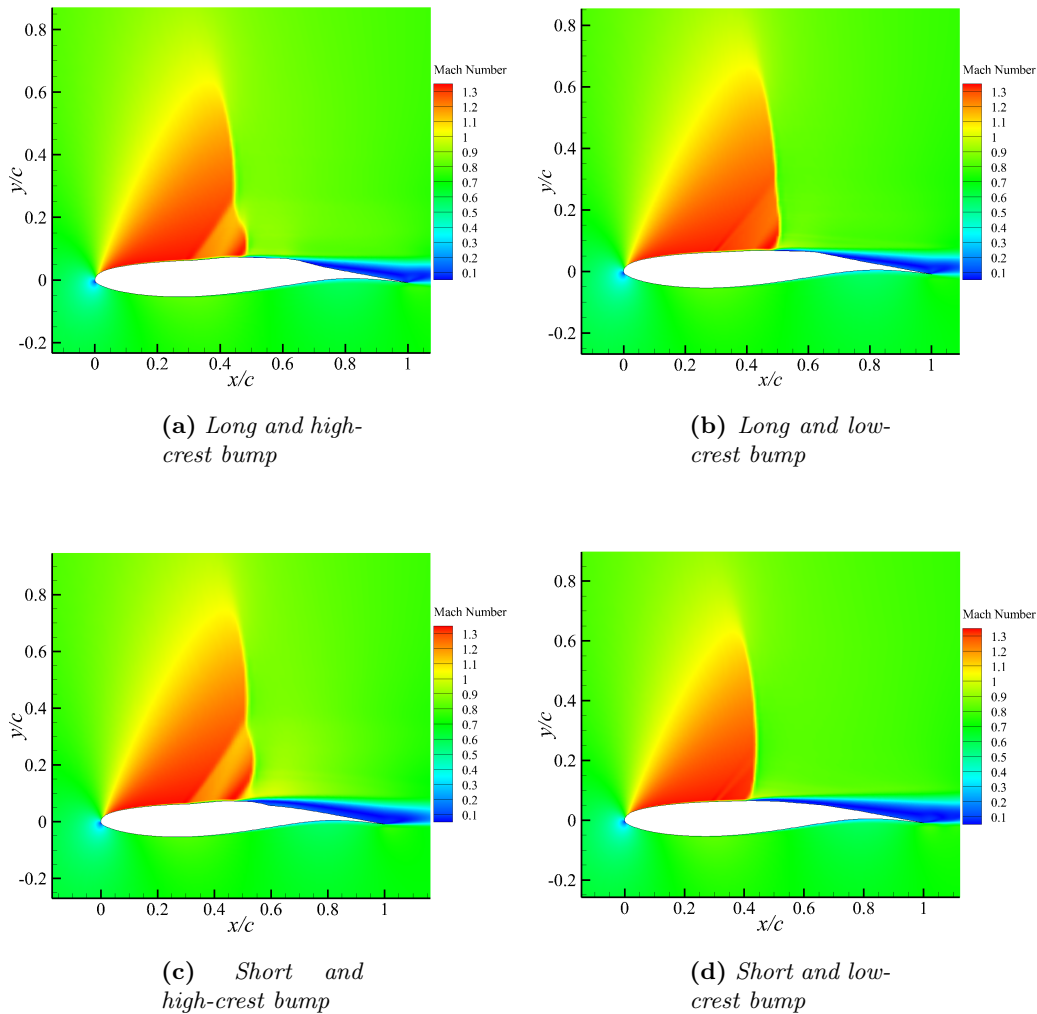


**Figure 4.2:** Mach number contours for forward bumps ( $M_\infty=0.73$ ,  $\alpha=3.5^\circ$ )

The numerical values of the front oblique shock angles shown in Figure 4.3 and 4.5 are listed in Table 4.1 and 4.2, as compared with the theoretical values which are obtained from the method used in Section 3.3. The upstream Mach number of an oblique shock wave  $M_1$  is calculated from the steady RANS equation, and the turn angle is the angle between the bump ramp and the horizontal direction in  $x$ -coordinate. For a forward long high-crest and low-crest bump, the CFD and theoretical values of the shock angles are quite close, whereas the values for a short and high-crest and low-crest bump do not match exactly. This may be due to the following reasons: the intensity and location of the oblique shock; the human errors made from inaccurate measurements of the input parameters (upstream Mach number and turn angle) and the systematic errors from the numerical method.

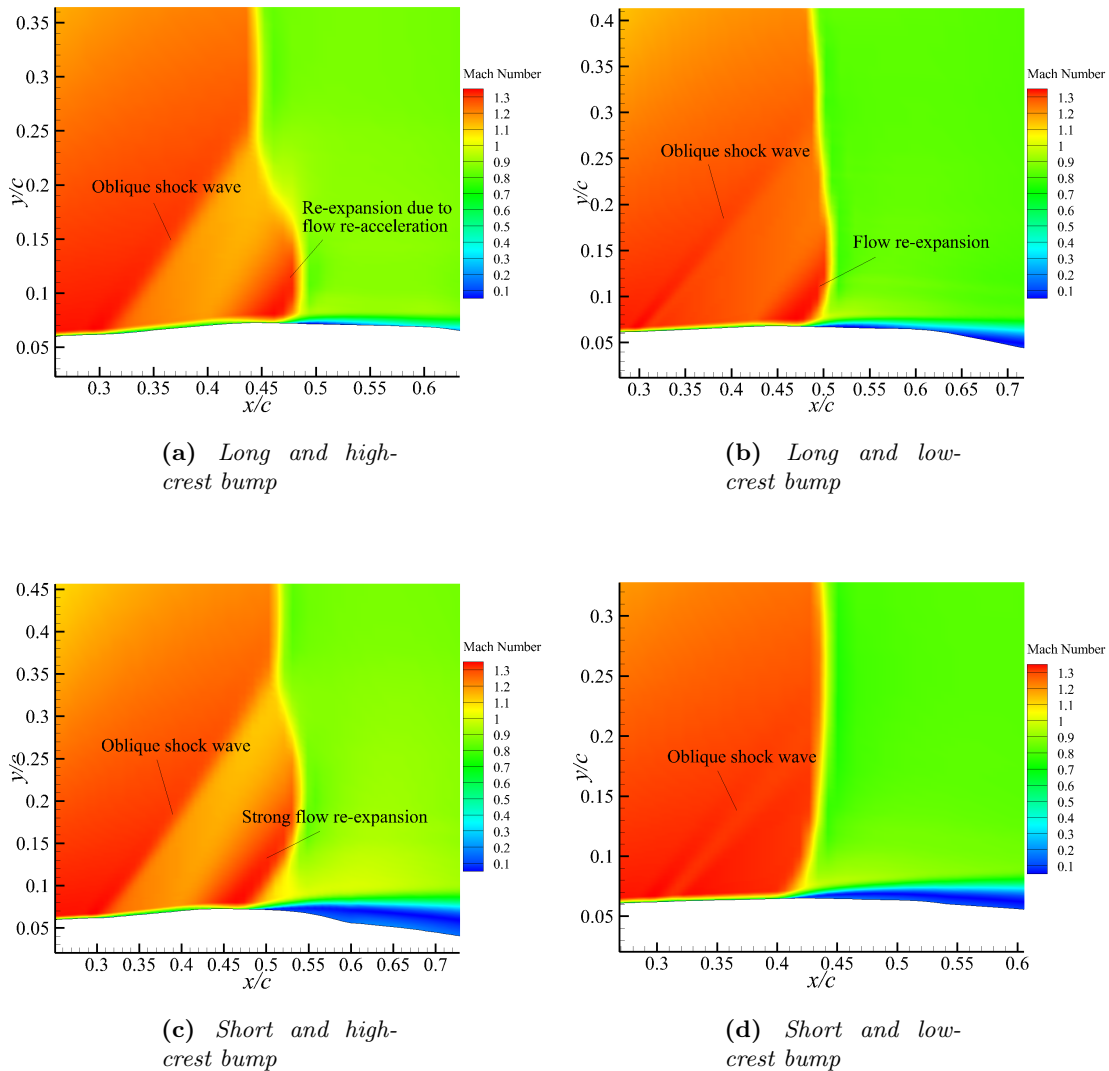


**Figure 4.3:** Flow structures in the vicinity of forward bumps ( $M_\infty=0.73$ ,  $\alpha=3.5^\circ$ )

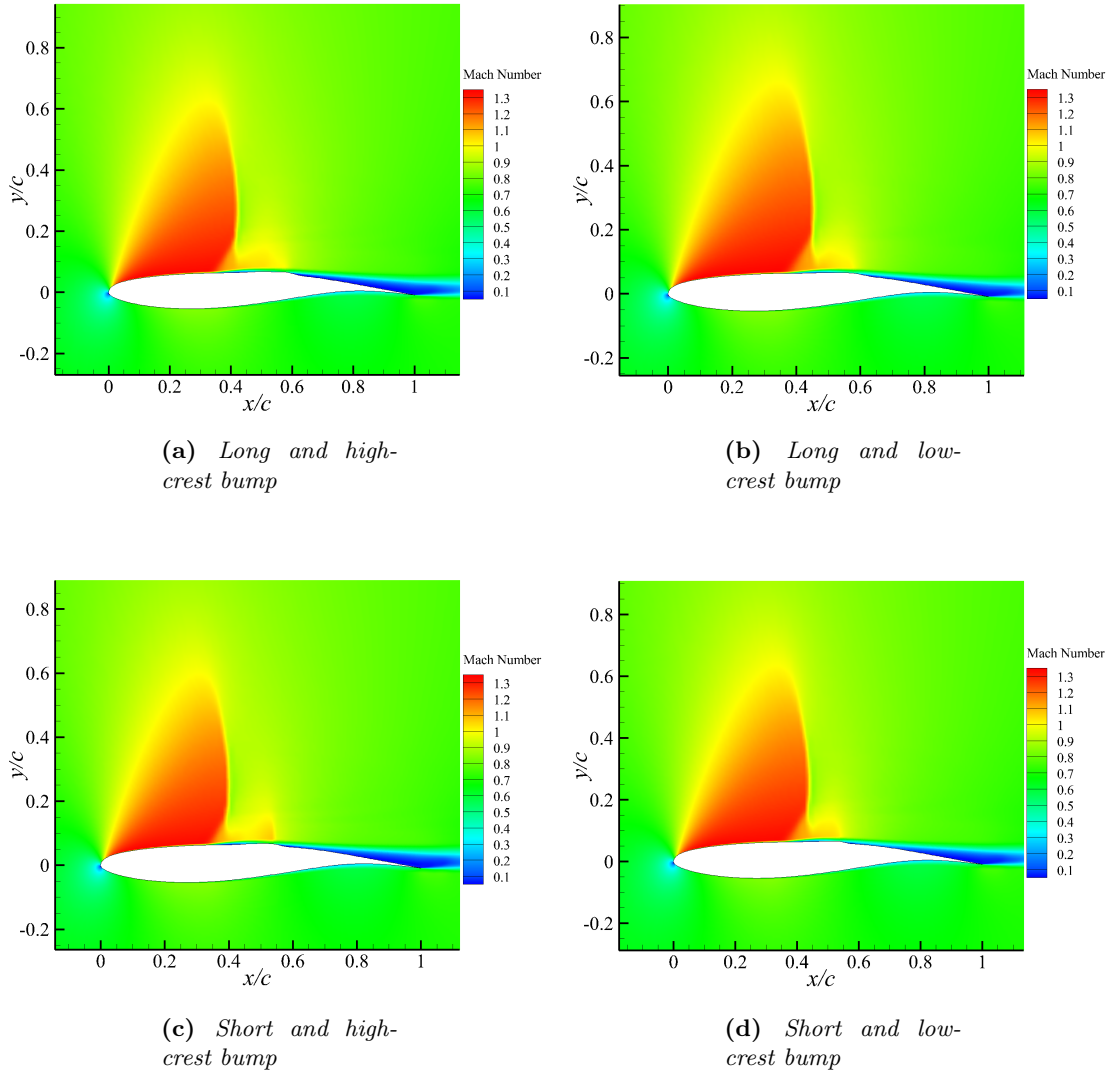
Long and high-crest bump		
$M_1$	Turn angle	Shock angle
1.34	4.81°	56.23°(Theory)55.83°(CFD)
Long and low-crest bump		
$M_1$	Turn angle	Shock angle
1.40	2.42°	48.76°(Theory)48.43°(CFD)
Short and high-crest bump		
$M_1$	Turn angle	Shock angle
1.37	4.40°	53.47°(Theory)56.90°(CFD)
Short and low-crest bump		
$M_1$	Turn angle	Shock angle
1.34	1.19°	48.46°(Theory)51.44°(CFD)

**Table 4.1:** Shock angle comparison with forward bumps

Long and high-crest bump		
$M_1$	Turn angle	Shock angle
1.32	2.16°	52.55°(Theory)60.80°(CFD)
Long and low-crest bump		
$M_1$	Turn angle	Shock angle
1.30	1.40°	52.46°(Theory)58.53°(CFD)
Short and high-crest bump		
$M_1$	Turn angle	Shock angle
1.30	1.52°	52.08°(Theory)59.45°(CFD)
Short and low-crest bump		
$M_1$	Turn angle	Shock angle
1.31	1.40°	51.88°(Theory)59.45°(CFD)

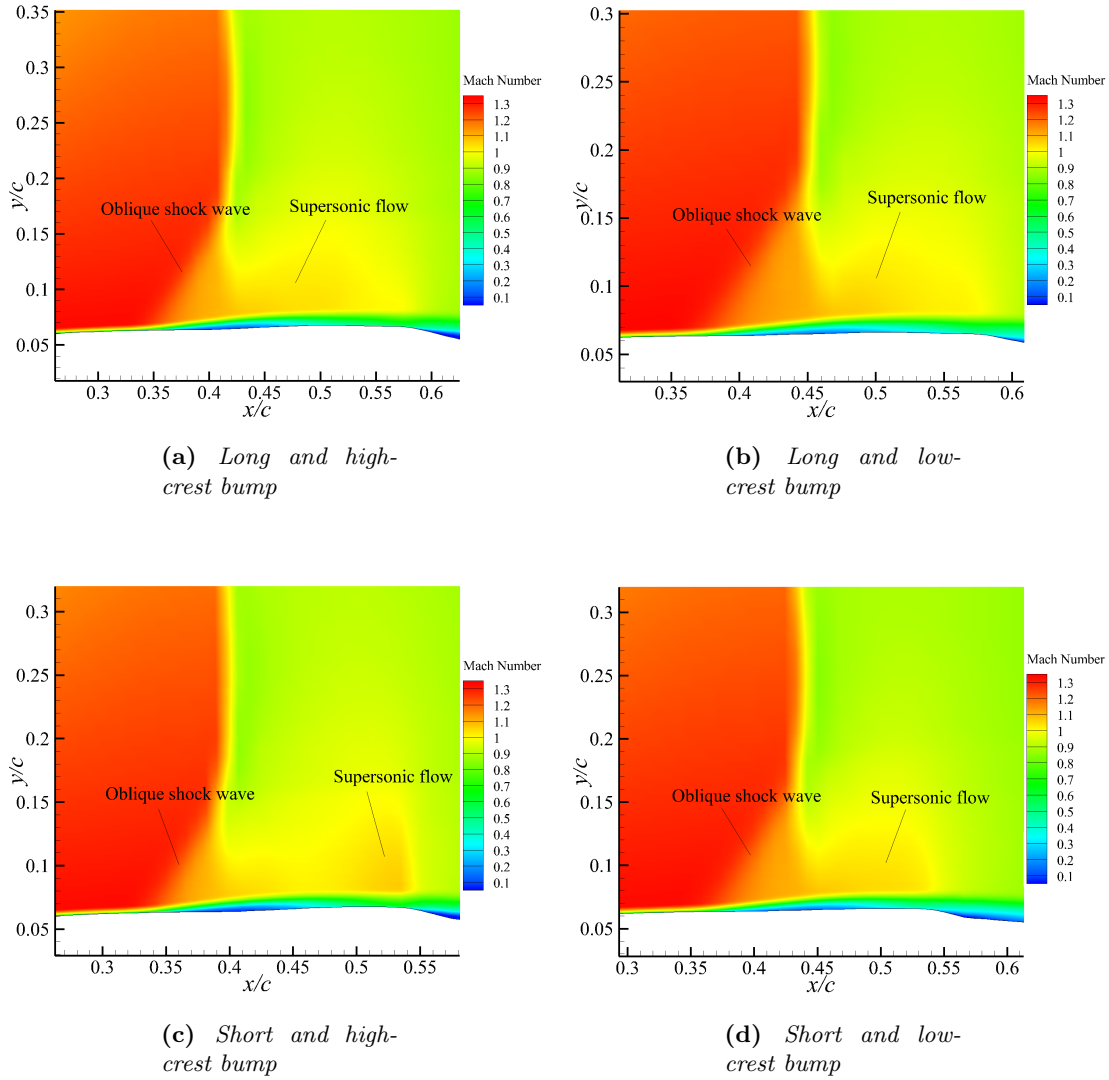
**Table 4.2:** Shock angle comparison with backward bumps

Figure 4.4 presents the full view of the flowfield controlled by the backward bumps, while Figure 4.5 presents the flow structures in the vicinity of the backward bumps. It can be seen from Figure 4.5 that the oblique shock waves created by the backward bumps are much weaker than the forward bumps, and no significant flow re-acceleration is found on the crest region of the backward bumps. The locations of the front oblique shock waves are  $x/c=37\%$ (long and high-crest bump),  $x/c=39\%$ (long and low-crest bump),  $x/c=35\%$ (short and high-crest bump) and  $x/c=39\%$ (short and low-crest bump). A bubble-like supersonic flow zone is created downstream to the shock wave. This additional supersonic flow is a part of the flow structure of shock wave/boundary-layer interaction and does not incur significant flow re-expansion that can cause a secondary shock wave. A very small region of flow separation can be found beneath the oblique shock wave, which lifts the supersonic tongue marginally above the bump crest. As shown in Figure 4.5(a) and 4.5(b), a bump with long chord length drags the supersonic bubble from  $x/c=41\%$  to 57%. As presented in Figure 4.5(c) and 4.5(d), a bump with short chord length only expands it from  $x/c=41\%$  to 55%.



**Figure 4.4:** Mach number contours for backward bumps ( $M_\infty=0.73$ ,  $\alpha=3.5^\circ$ )

To sum up, the bump location and geometry greatly characterise the flowfield. Despite the closeness between the forward and backward positions, a forward bump creates relatively stronger shock and expansion waves than the backward bumps, as well as flow separation. The forward bumps can accelerate the subsonic flow downstream to an oblique shock, but no significant flow re-acceleration can be found on the backward bumps as they can anchor the oblique shock at a fixed location. Regarding the geometry, a long bump can ease the separated flows at the shock foot, whereas a short bump can worsen the flow separation somewhere downstream to a shock, especially at the bump tail. Also, a bump with low crest height can produce weaker re-expansion than the high-crest bump.



**Figure 4.5:** Flow structures in the vicinity of backward bumps ( $M_\infty=0.73$ ,  $\alpha=3.5^\circ$ )

### 4.1.2 Streamwise velocity profiles

To study the boundary-layer status associated with the shock-induced separation, the longitudinal velocity profiles in the streamwise direction are plotted and compared with the experimental data obtained from the S3 Wind Tunnel test done by *ONERA Chalais-Meudon*. These measurements are conducted using a technique called *Laser Doppler Velocimetry* (LDV). Figure 4.10 shows the numerical and experimental results of the velocity profiles at four different locations on the suction side of a baseline aerofoil in a flow condition of  $M_\infty=0.73$  and  $\alpha=3.5^\circ$ . The  $y$ -coordinate is non-dimensionalized by dividing the aerofoil chord, while the velocity in  $x$ -coordinate is non-dimensionalized by dividing the freestream velocity which is about 253  $m/s$ . Overall, the numerical solution from RANS equation provides relatively good predic-

tions of the velocities in the outer-layer, but do not match very well in the inner-layer zones including a viscous sub-layer and a buffer layer. In the supersonic flow region, namely the locations of  $x/c=0.28$  and  $0.35$ , the boundary-layer remains attached to the aerofoil surface as the streamwise velocity equals to zero at the wall. The boundary-layer thickness at  $x/c=0.35$  is slightly thicker than  $x/c=0.28$ , which are approximately equivalent to 0.6% and 0.5% of the aerofoil chord length, respectively. At the location of  $x/c=0.55$ , the boundary-layer continues thickening and tends to separate as the reverse flow starts to emerge at the wall. At the location of  $x/c=0.75$ , which is closed to the trailing edge, a much thicker boundary-layer is created, and a negative velocity gradient occurs at the surface.

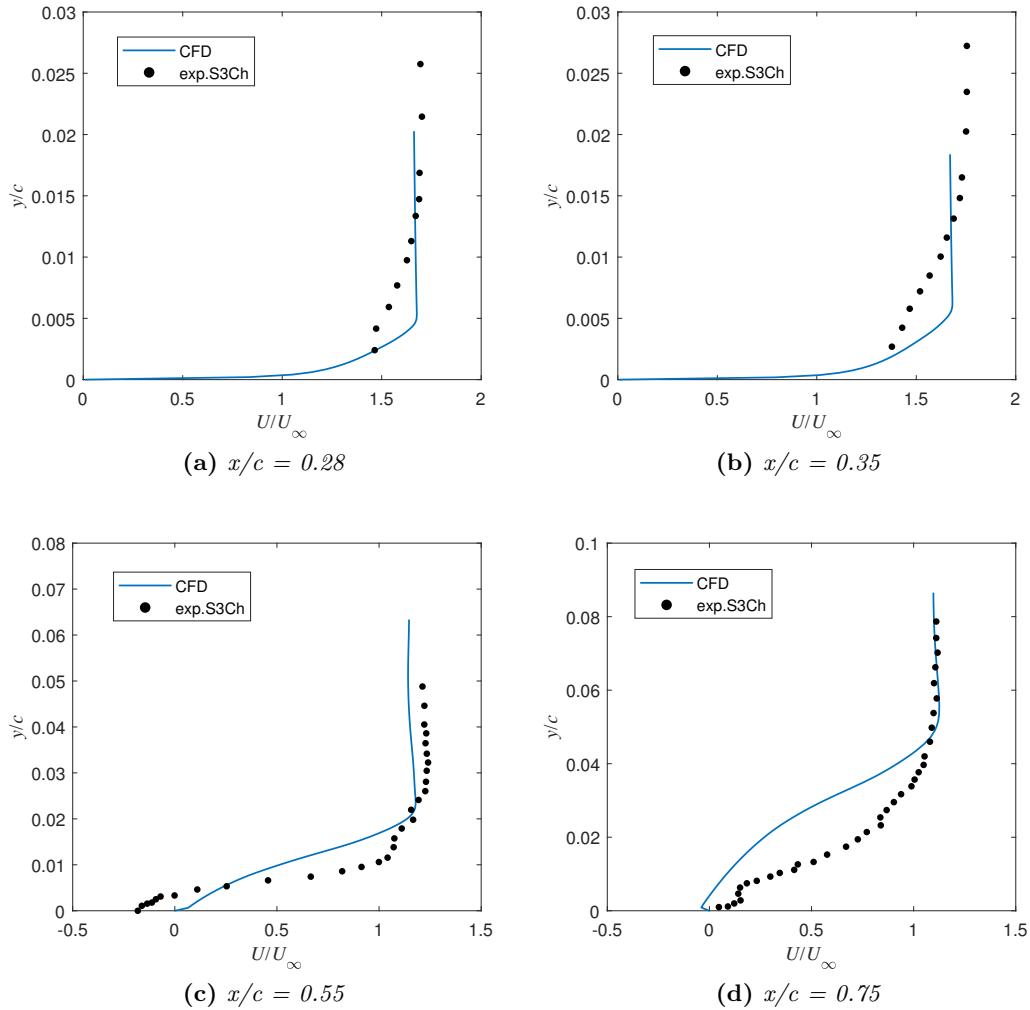


**Figure 4.6:** Streamwise velocity profiles at four different locations on a baseline aerofoil ( $M_\infty=0.73$ ,  $\alpha=3.5^\circ$ )

Figure 4.11 presents the unsteady velocity profiles at four instants within a complete buffet cycle at a location of  $x/c=0.6$ . The letter  $T$  stands for the period of the shock-induced oscillation. It can be seen that all the numerical results match quite well with the experimental ones in both the inner and outer layer of the boundary-layer. The boundary-layer is separated at the time when  $t=0.05T$  and reattaches to the wall at  $t=0.25T$ . During this time the shock wave moves in the upstream direction to the oncoming flow. From  $t=0.45T$  and to  $t=0.65T$ , the shock wave moves in the downstream direction and the boundary-layer gets increasingly thicker until the shock reaches its maximum downstream position.

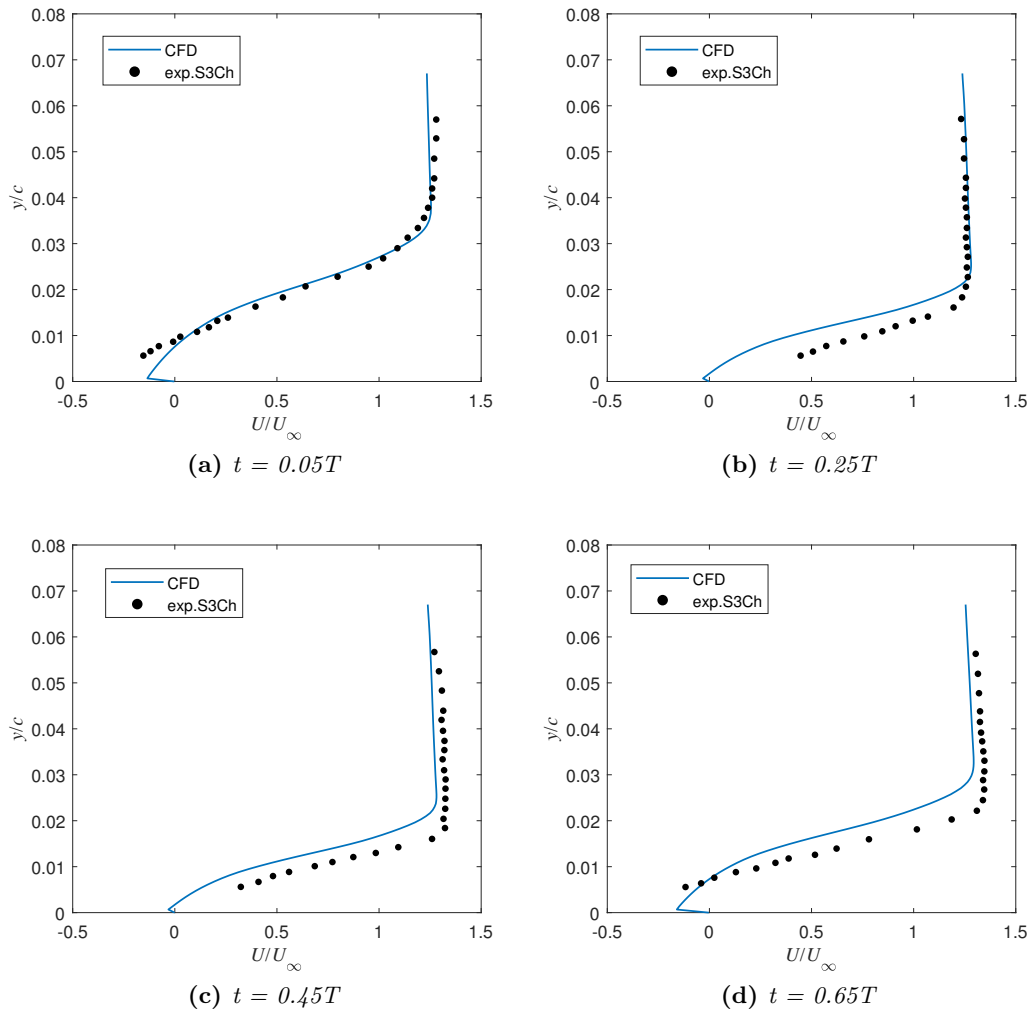


**Figure 4.7:** Local streamwise velocity profiles within one buffet cycle for a baseline aerofoil ( $M_\infty=0.73$ ,  $\alpha=3.5^\circ$ ,  $x/c=0.6$ )

Figure 4.12 shows the velocity profiles in streamwise direction at a location of  $x/c=0.6$  for a baseline aerofoil and the aerofoils with bump control. This location is somewhere between the bump crest and the bump tail on the forward bumps, and for the backward bumps, this location is on the bump crest. It can be seen clearly that the boundary-layers created by the control bumps become thinner than a baseline aerofoil, and the boundary-layer thicknesses on the backward bumps are lower than the forward bumps. Also, there is a very thin viscous layer on a forward long and high-crest bump where the no-slip wall boundary condition is satisfied. However, some of the forward and backward bumps incur a thin shear layer in the near-wall region, in which the flow velocity is not equal to zero at the wall.

To summarise, the boundary-layer can be strongly affected when it interacts with a shock wave in a transonic buffet flow. The local velocity profile shows that the boundary-layer can develop from full attachment to a complete separation. The flow upstream to a shock is considered to be fully developed, and the flow downstream to a shock has a developing behaviour as the boundary-layer thickness can rise in the streamwise direction. A shock control bump can lower the boundary-layer thickness in the subsonic flow zone downstream to a shock wave, hence the boundary-layer becomes more stable than a baseline aerofoil.

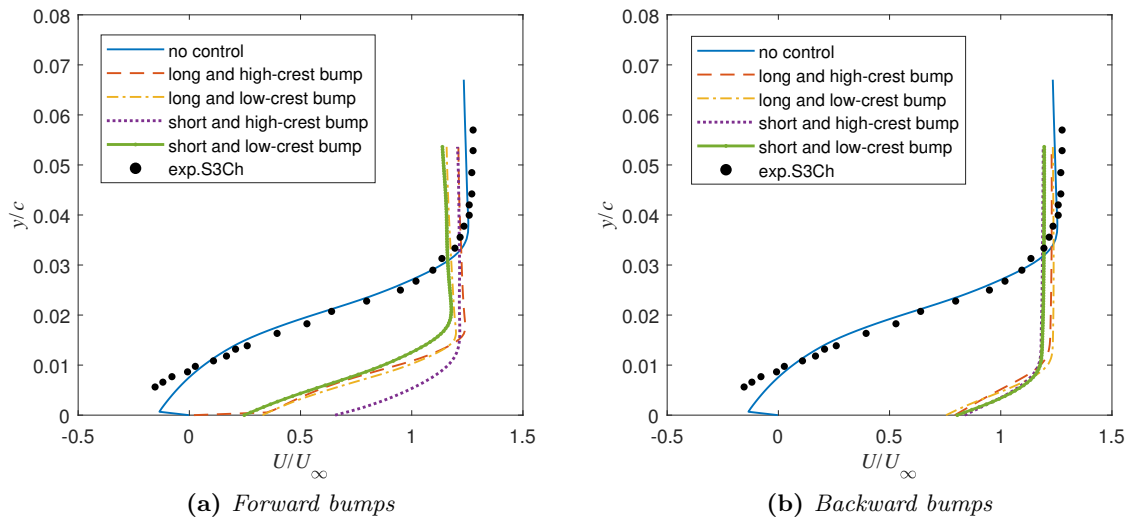


**Figure 4.8:** Streamwise velocity profiles at  $x/c=0.6$  for different bumps ( $M_\infty=0.73$ ,  $\alpha=3.5^\circ$ )

## 4.2 Transient solutions

### 4.2.1 Unsteady lift

#### Uncontrolled case

The time histories of the lift and drag coefficients are obtained from URANS simulations and are presented for different flow conditions and turbulence models. For a buffet onset condition ( $M_\infty=0.73$ ,  $\alpha=3.5^\circ$ ), as shown in Figure 4.9, the lift and drag coefficients finally converge to a steady-state after a gradual trend of damping. This indicates that the shock buffet will automatically disappear in a finite time. Moreover, each turbulence model exhibits an identical form of oscillation except the amplitude and frequency, which can be reflected by the Power Spectra Density (PSD) graphs shown in Figure 4.10. The PSD graphs are produced by performing Fast Fourier Transform (FFT), and they are presented in different spectra with the frequency and amplitude shown in logarithmic scales. It can be seen from Figure 4.10 that for all three turbulence models, the frequencies of lift and drag oscillation are consistent, maintaining at about 72 Hz (*Spalart-Allarmas*), 73 Hz (SST  $k-\omega$ ) and 76 Hz (Realizable  $k-\epsilon$ ). These frequencies are regarded as the main frequency of the lift and drag oscillation in a buffet period. For the lift and drag PSD, *Spalart-Allarmas* model has an amplitude that is marginally higher than the SST  $k-\omega$  model, while the Realizable  $k-\epsilon$  model produces the lowest amplitude of oscillation in finite computation time. It is also interesting to see that the Realizable  $k-\epsilon$  model shows the consistent amplitude and frequency for lift and drag oscillation. Besides, the sensitivity of the self-sustained lift and drag oscillations are also studied by varying the angle of attack, as shown in Figure 4.11(a). The PSD graphs of the corresponding time histories for the lift and drag signals are also displayed in Figure 4.11(b). It can be noticed from the time response of lift coefficient that the amplitude of oscillation is slightly decreased for an increased angle of attack, while the frequency of oscillation remains the same, as can be seen in the frequency domain signal. The time response of the drag coefficient shows a slight shift-up for an increased angle of attack.

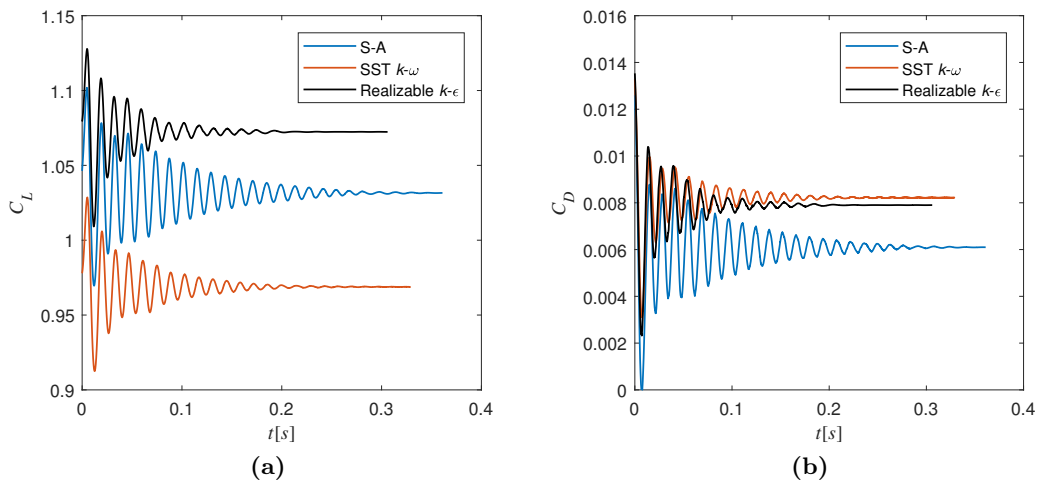


**Figure 4.9:** Time histories of (a) lift and (b) drag coefficients for a baseline aerofoil with different turbulence models ( $M_\infty=0.73$ ,  $\alpha=3.5^\circ$ )

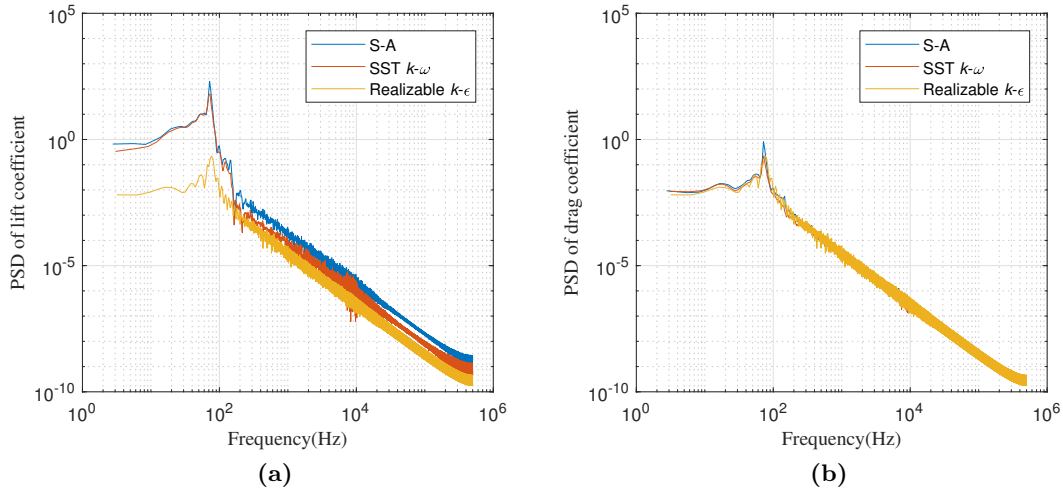


**Figure 4.10:** PSD of (a) lift and (b) drag coefficients for a baseline aerofoil with different turbulence models ( $M_\infty=0.73$ ,  $\alpha=3.5^\circ$ )

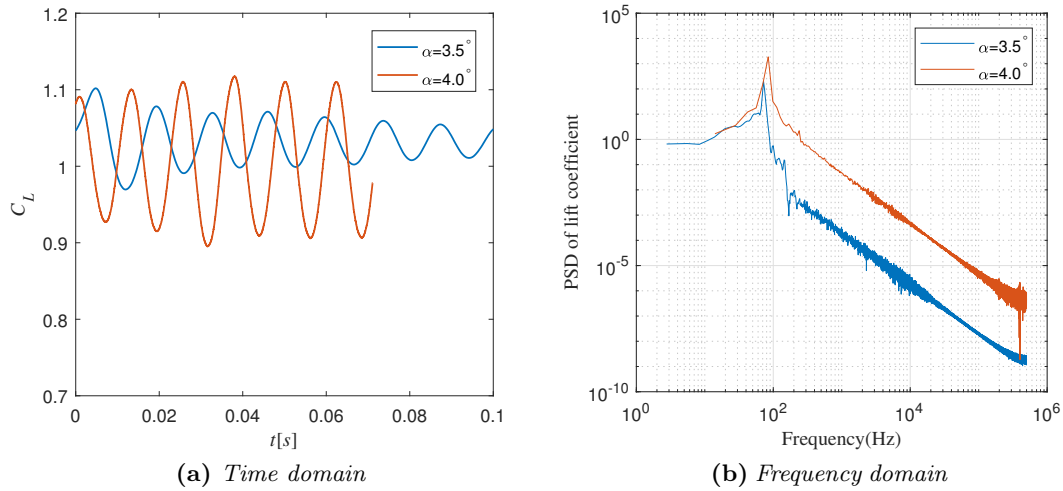


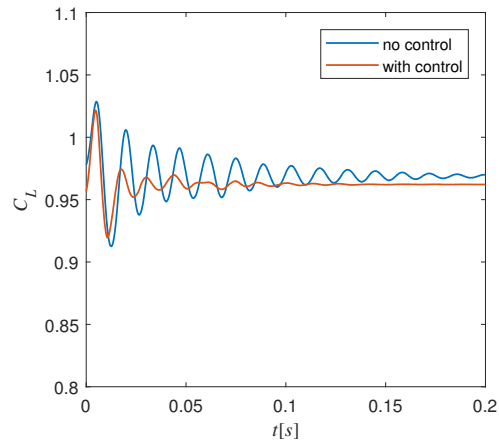
**Figure 4.11:** (a) Time and (b) frequency responses of lift coefficient for a baseline aerofoil with different angles of attack ( $M_\infty=0.73$ )

For a flow Mach number of 0.73 and  $4.0^\circ$  angle of attack, the time response of lift coefficient turns to a limit cycle oscillation, as shown by the red curve in Figure 4.11(a). At this flow condition, the shock oscillation can sustain itself with a higher frequency and amplitude, as can be identified from the PSD graph shown in Figure 4.11(b) where the main frequency of oscillation becomes 83 Hz compared to a buffet onset frequency of 72 Hz computed by unsteady RANS equation with *Spalart-Allmaras* model at  $3.5^\circ$  angle of attack. This analysis shows that the frequency of the periodic lift oscillation associated with shock-buffet is sensitive to angle of attack.

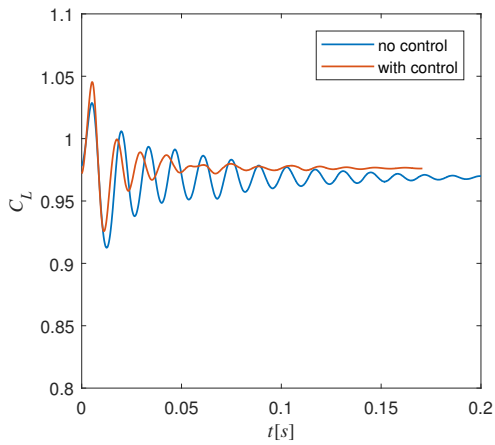
To sum up, the characteristics of shock-buffet is directly influenced by the freestream Mach number and the flow incidence, and the shock-induced oscillation is also very sensitive to the angle of attack. At a condition of buffet-onset, the oscillatory shock movement can develop in a finite time but gradually decays to steady-state. As the angle of attack reaches  $4.0^\circ$ , the shock motion becomes unsteady and can keep oscillating. Each turbulence model produces different frequencies and amplitudes within an acceptable error for a given transonic flow condition. It is encouraging to note that the periodic nature of transonic buffet due to the shock wave/boundary-layer interaction can be easily discovered by conducting a simple 2D CFD simulation. However, a wind tunnel experiment that can duplicate this mechanism is also demanding and essential, but this is beyond the scope of this research.

### Controlled case

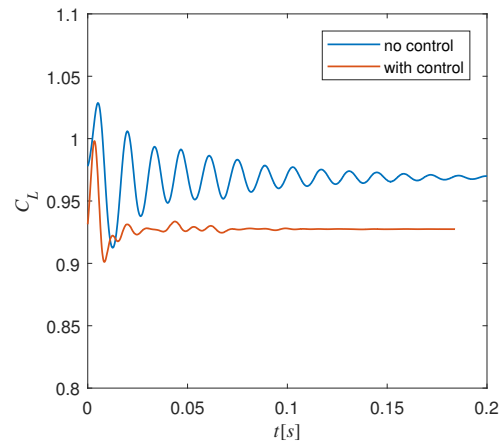
The control performances for all designed bumps are obtained by conducting a transient computation using the dual-time marching scheme, and the time histories for an aerofoil with/without control are compared. The time step used is  $1\mu\text{s}$ , and the duration of the simulation is 0.2s. Figure 4.12 and 4.13 show the lift responses in the time domain for the forward and backward bumps. Figure 4.14 and 4.15 present the lift responses expressed in the frequency domain for the forward and backward bumps. For a flow condition of  $M_\infty=0.73$  and  $\alpha=3.5^\circ$ , the time responses for all designed bumps indicate a prominent impact on controlling the self-sustained lift and drag oscillation. It shows that a shock control bump can effectively suppress the shock-induced oscillation with reduced frequency and amplitude, and time responses of the lift and drag coefficients converge faster to steady-state than an uncontrolled shock-induced oscillation. The PSD variations are plotted by converting the time-dependent signals to frequency domain signals. These plots provide an intuitive analysis of the controlled mechanisms. For an aerofoil with/without control, the primary frequency and amplitude locate at the low-frequency spectra on a PSD graph, which ranges from 0 to  $10^2\text{Hz}$ . For an aerofoil with control, the lift response indicates a fuzzy fluctuation at a medium frequency spectra ranging from  $10^2\text{Hz}$  to  $10^4\text{Hz}$ , then it finally decays at a high-frequency spectrum. The natural frequencies of the lift response on the forward bumps are 72Hz (long and high-crest bump), 41Hz (long and short-crest bump), 58Hz (short and high-crest bump) and 75Hz (short and low-crest bump). The natural frequencies of the lift response on the backward bumps are 52Hz (long and high-crest bump), 49Hz (long and short-crest bump), 53Hz (short and high-crest bump) and 71Hz (short and low-crest bump).



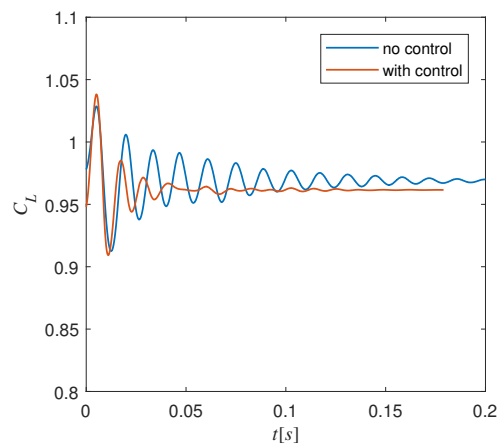
(a) Long and high-crest bump



(b) Long and low-crest bump

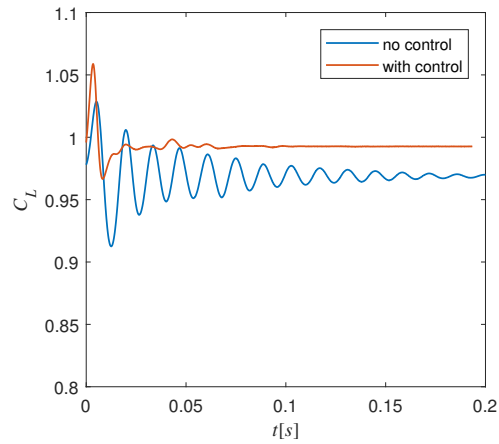


(c) Short and high-crest bump

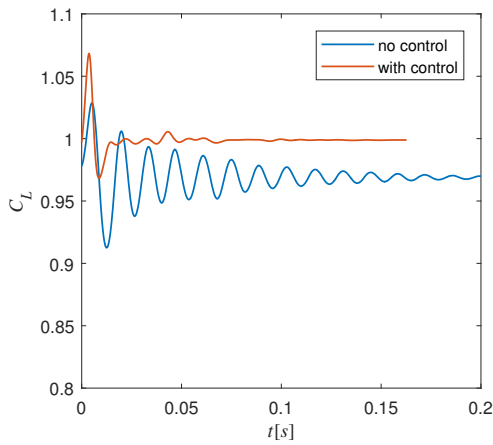


(d) Short and low-crest bump

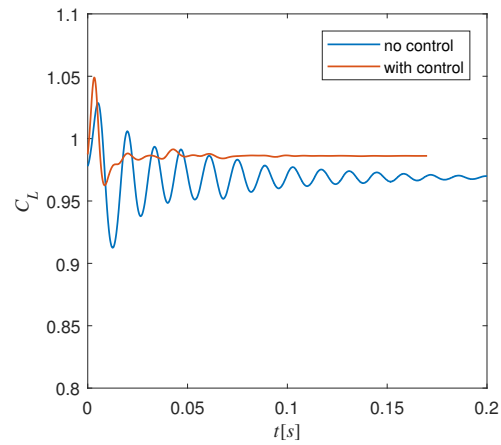
Figure 4.12: Lift response for forward bumps ( $M_\infty=0.73$ ,  $\alpha=3.5^\circ$ )



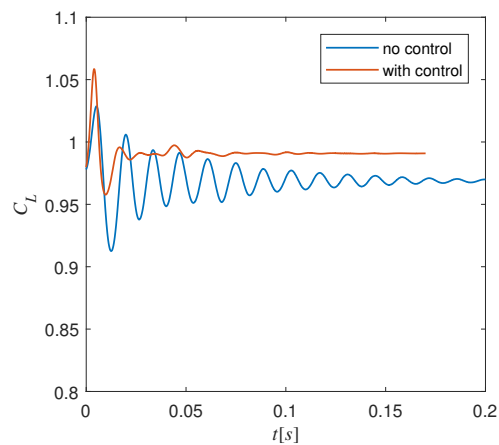
(a) Long and high-crest bump



(b) Long and low-crest bump

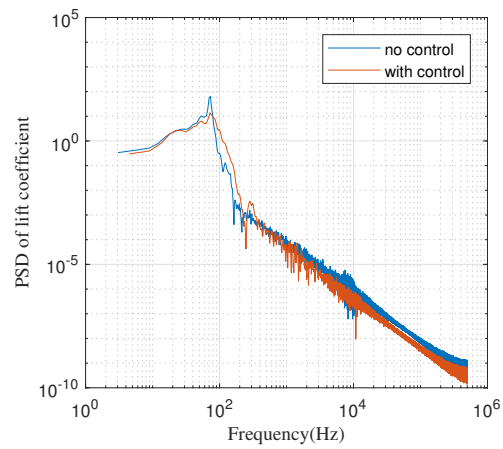


(c) Short and high-crest bump

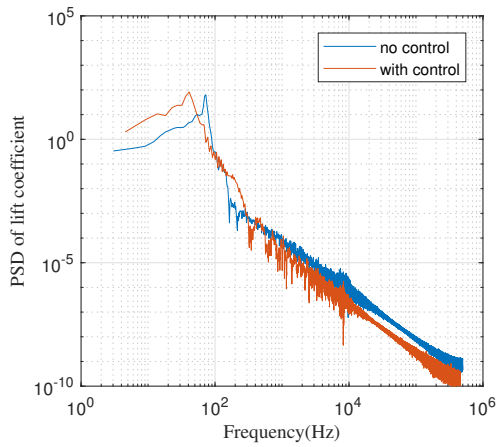


(d) Short and low-crest bump

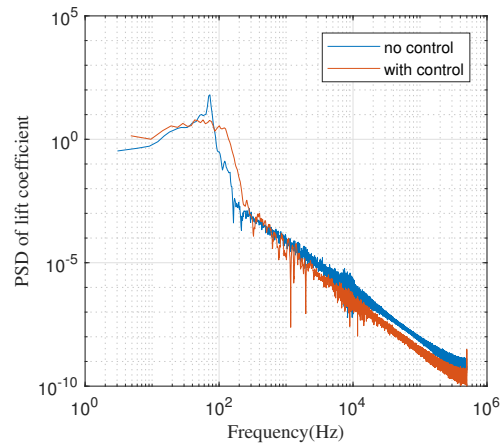
Figure 4.13: Lift response for backward bumps ( $M_\infty = 0.73$ ,  $\alpha = 3.5^\circ$ )



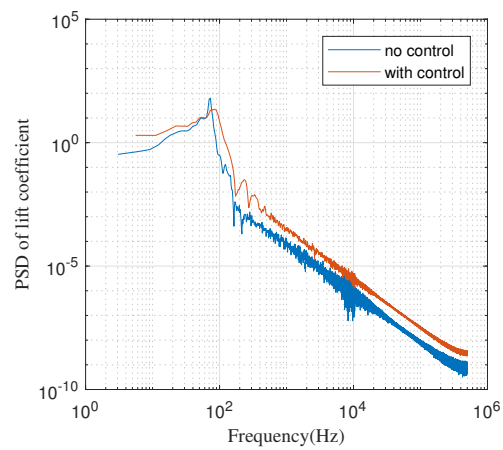
(a) Long and high-crest bump



(b) Long and low-crest bump

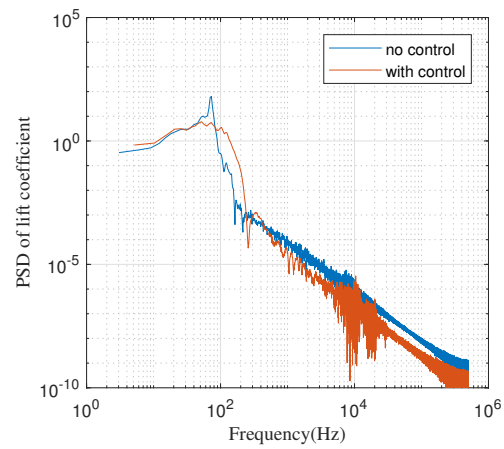


(c) Short and high-crest bump

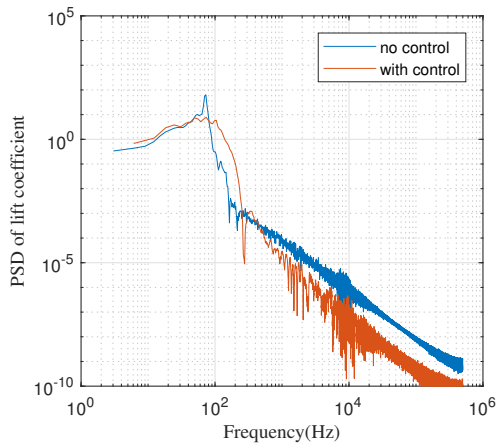


(d) Short and low-crest bump

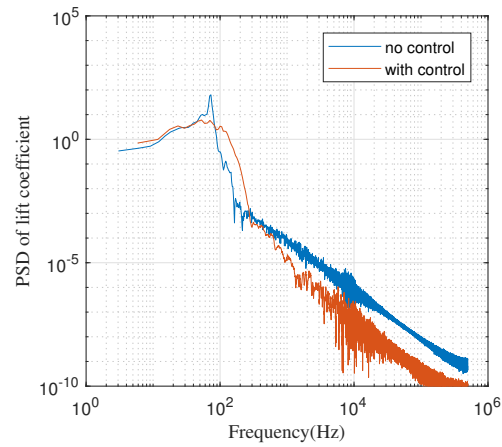
Figure 4.14: PSD of lift coefficient for forward bumps ( $M_\infty=0.73$ ,  $\alpha=3.5^\circ$ )



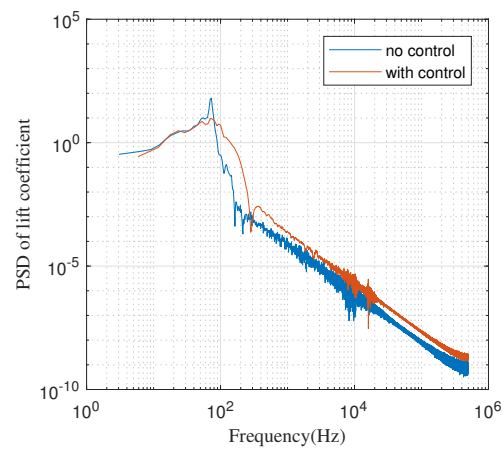
(a) Long and high-crest bump



(b) Long and low-crest bump



(c) Short and high-crest bump



(d) Short and low-crest bump

**Figure 4.15:** PSD of lift coefficient for backward bumps ( $M_\infty=0.73$ ,  $\alpha=3.5^\circ$ )

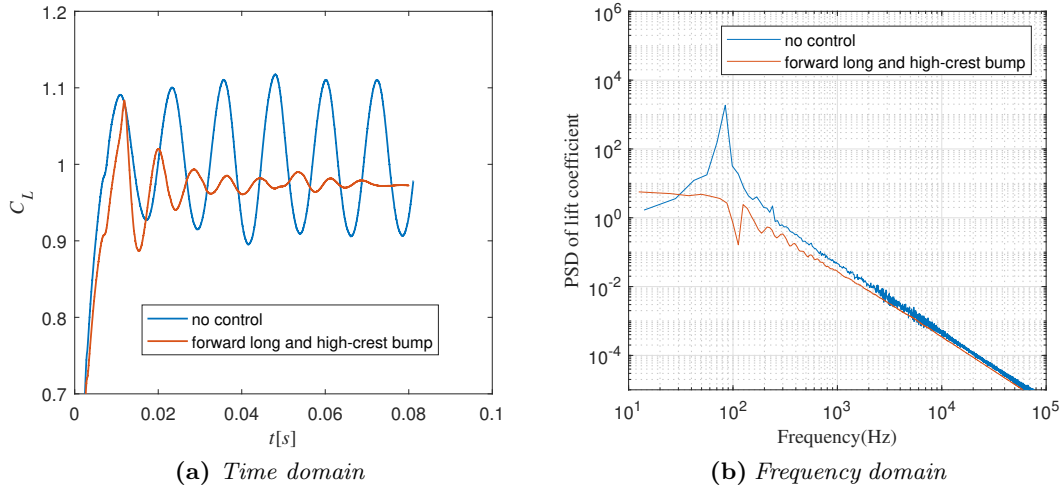


**Figure 4.16:** (a) Time and (b) frequency responses of lift coefficient with/without control ( $M_\infty=0.73$ ,  $\alpha=4.0^\circ$ )

In addition, the control performance of a forward long and high-crest bump has also been evaluated with a flow condition of  $M_\infty=0.73$  and  $\alpha=4.0^\circ$ . The variations of the lift coefficient with/without control are obtained in both time and frequency domain, as indicated in Figure 4.16. It can be seen from Figure 4.16(a) that a shock control bump is still capable of effectively suppressing the self-sustained shock oscillation associated with transonic buffet. With control, the lift oscillation indicates an initially damped behaviour then gradually tends to a steady state as time progresses. Also, the fluctuation associated with the unsteady shock motion has been significantly mitigated, indicating an effective suppression of transonic buffet achieved by a 2D surface bump control.

The mechanisms of the unsteady shock-induced oscillation have been predicted for a baseline aerofoil with different turbulence models and angle of attack. It has also been demonstrated numerically that a 2D surface bump successfully alleviates the periodic and self-sustained shock motion. In the presence of bump control, a damping behaviour has been observed at the initial transient of the simulation, and the frequency and the amplitude of the lift response starts decaying to steady-state as time passes.

### 4.2.2 Unsteady pressure fluctuation

The time-varying pressure signals are obtained using the data computed from the transient simulation. The Root-Mean-Squared value of the static pressure fluctuation is calculated for each type of bump configuration. The distributions of RMS fluctuation with/without control are plotted concerning the chordwise direction, as shown in Figure 4.17. It has been demonstrated that the RMS fluctuation for a baseline aerofoil has one single peak, indicating the maximum value of pressure fluctuation at the mid-chord. The aerofoil with a forward long and high-crest bump creates two peaks in RMS pressure fluctuation. The first peak locates at about  $x/c=40\%$ , at which the value of RMS fluctuation is higher than the uncontrolled case. The second peak appears at about  $x/c=65\%$ , whose value is approximately equal to a baseline aerofoil. A similar pattern can also be observed from the RMS fluctuation over an aerofoil with a backward long and high-crest bump, as can be seen in Figure 4.18(a).

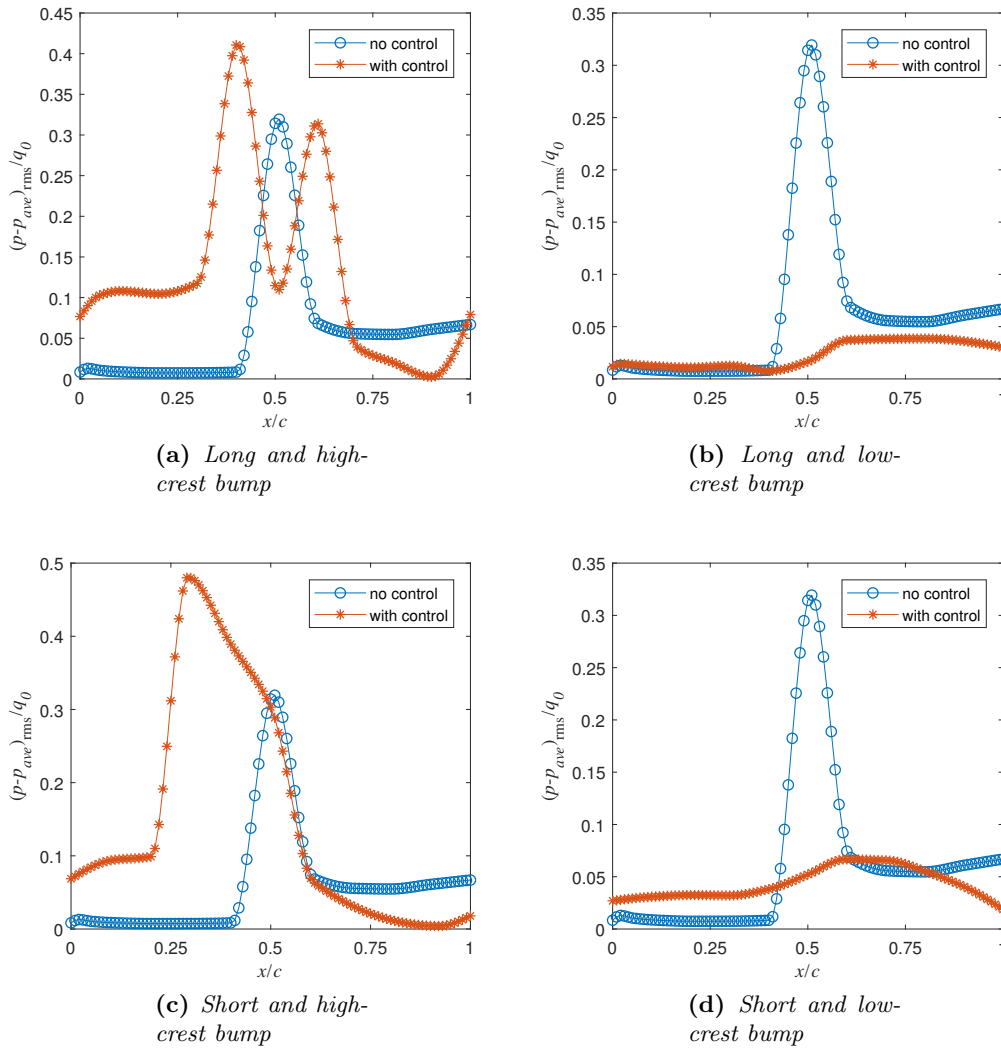


**Figure 4.17:** Root-Mean-Squared pressure fluctuation distributions for forward bumps ( $M_\infty=0.73$ ,  $\alpha=3.5^\circ$ )

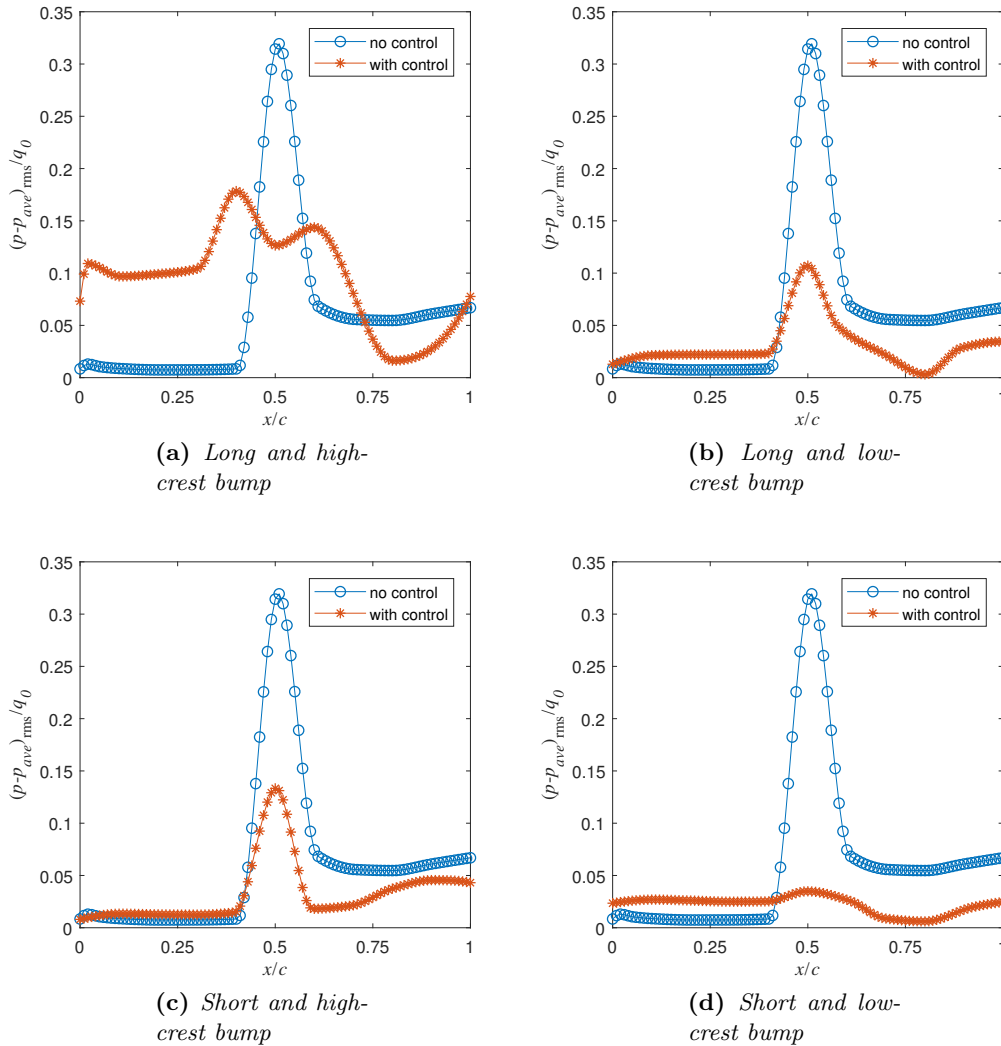


**Figure 4.18:** Root-Mean-Squared pressure fluctuation distributions for backward bumps ( $M_\infty=0.73$ ,  $\alpha=3.5^\circ$ )

A forward long and low-crest bump presents no significant pressure fluctuation over the bump profile, and the RMS fluctuation maintains to be lower than the baseline aerofoil from  $x/c=40\%$  down to the trailing edge. The maximum RMS fluctuation created by a forward short and high-crest bump is relatively higher than the uncontrolled aerofoil, with a value of 48% located at  $x/c=30\%$ . Similar to the long and low-crest bump, no peak points are found along the entire aerofoil chord and the values of RMS fluctuation are well below 10%. A backward long and high-crest bump also creates two turning points at the locations of  $x/c=40\%$  and  $60\%$ , at which the extreme values of RMS fluctuation have gone down to 20% of the uncontrolled case. It also shows that the pressure fluctuation ahead of the bump is about 100 times higher than a baseline aerofoil. This is caused by the deceleration of supersonic flow passing through an oblique shock wave along an inclined surface of a bump ramp, leading to an increase of static pressure. Meanwhile, there is also a drop-down of RMS

fluctuation near the trailing edge, on which a minimum value of pressure fluctuation occurs at about  $x/c=80\%$ . A backward long and low-crest bump indicates a maximum pressure fluctuation at mid-chord but has a value of only 30% of the uncontrolled case. Besides, a minimum pressure fluctuation is also found on  $x/c=80\%$ , and the value of RMS pressure fluctuation on a backward long and low-crest bump is well below 10% from  $x/c=40\%$  to the trailing edge. A backward short and high-crest bump also creates a maximum RMS fluctuation at the mid-chord, with a value of about 50% of the baseline aerofoil. For a backward short and low-crest bump, no significant pressure fluctuation exists on the entire aerofoil and the RMS values are below 5%.

Overall, it can be concluded that some of the bump configurations produce the considerable effect of weakening the unsteady pressure fluctuation on an aerofoil, whereas some of them are unable to achieve desired outcomes. A long and high-crest bump has a negative impact of creating multiple fluctuation points over the bump profile, regardless of a forward or a backward position. A forward short and high-crest bump can amplify the level of pressure fluctuation on a forward position that is closed to the aerofoil's leading edge. To sum up, a forward long and low-crest bump, a forward short and low-crest bump and a backward short and low-crest bump are most effective to attenuate pressure fluctuation and maintain the value below 10%, while a backward long and low-crest bump and a backward short and high-crest bump achieve dramatic suppression of pressure fluctuation but with a maximum value above 10%.

# Chapter 5

## Discussion of results

### 5.1 No control

The surface pressure and wall shear stress distribution on a baseline aerofoil show that an adverse pressure gradient exists at the mid-chord of an aerofoil, which incurs separated flow. The location of the shock wave and the flow separation point can vary for different angles of attack. A higher angle of attack shifts the shock wave to a forward position hence advances the onset of separation. A lower angle of attack can move the shock wave to a backward position, so the onset of the shock-induced separation can be suppressed and delayed.

The flow over a transonic aerofoil is influenced by the shock wave/boundary-layer interaction. This interaction exhibits a transient and periodic nature, which can be reflected upon the high-frequency oscillation of a shock wave, as well as causing unsteady pressure fluctuation. The oscillatory behaviour of the aerodynamic forces depends chiefly on the flow Mach number and the angle of attack. A flow Mach number of 0.73 and a  $3.5^\circ$  angle of attack have been confirmed as the onset condition of transonic buffet. Similar behaviour related to this can also be observed for a marginally higher Mach number and angle of attack.

### 5.2 With control

The surface pressure distributions show that the forward bumps can create a favourable pressure gradient on the bump crest. A forward bump with a high crest causes a significant pressure rise, whereas a forward bump with a low crest creates less pressure jump on the bump ramp. A significant pressure rise can be found on a forward long and high-crest bump and a short and high-crest bump, whereas a forward long and low-crest bump creates the least pressure rise. A short and low-crest bump produces the largest pressure gradient across a normal shock wave. The shear stresses on the leading edges of the forward bumps are found to be lower than a baseline aerofoil, whereas higher shear stresses can be found on the bump crest. A forward bump with high crest causes larger separation on the bump tail, while a forward bump with low crest produces a local reattachment zone on the crest region and the boundary-layer becomes less separated.

A forward long and low-crest bump works as the most effective configuration by reducing the frequency of the shock-induced oscillation to a minimum. The pressure fluctuation on the surface of a forward long and low-crest bump is restricted to the lowest among all forward bumps. A forward short and low-crest bump also indicates an effective suppression in the pressure fluctuation. Although a forward long and high-crest bump and a forward short and high-crest bump can lower the pressure fluctuation on the trailing edge of an aerofoil, they fail to reduce the pressure fluctuations in the supersonic flow zone and even magnify them.

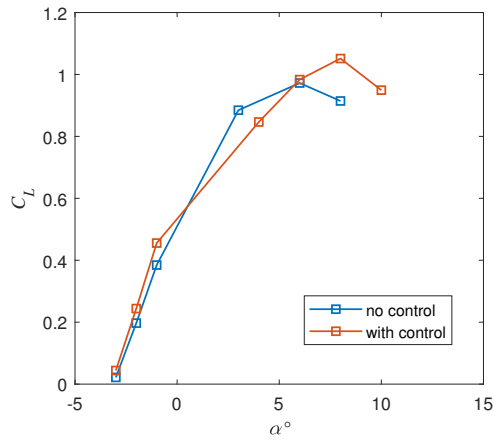
The backward bumps create moderate pressure jump, and the flow downstream to a shock wave becomes less separated than the forward bumps by creating a long flow reattachment downstream to a shock wave, which stabilises the viscous shear layer in the near-wall region by lowering the boundary-layer thickness. The time response of the aerodynamic force on the backward bumps becomes less oscillatory than a baseline aerofoil by anchoring the front oblique shock on the bump ramp. As shown by the transient results from the backward bumps, a gain of the steady-state lift that is higher than a baseline aerofoil can also be obtained from the backward bumps. Overall, the pressure fluctuation on a backward bump becomes lower than a baseline aerofoil. A backward short and low-crest bump achieves the most effective suppression in the pressure fluctuation.

## 5.3 Aerodynamic performance

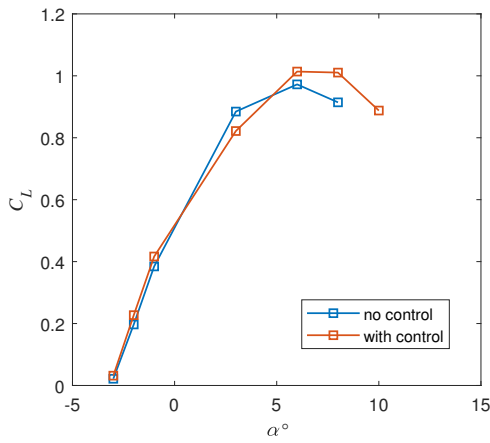
### 5.3.1 Lift curve

The lift curve is one of the aerodynamic properties which reflects how the lift on an aerofoil varies with the angle of attack, as well as indicating the stalling point at a certain flow incidence. At low angles of attack, the lift increases with the angle of attack, and the lift curve is considered to be linear as the flow around an aerofoil is steady. As the angle of attack increases, the lift curve will be non-linear as the flow starts to become quasi-steady until the aerofoil reaches its maximum lift coefficient. Further increasing the angle of attack leads to a loss of lift, thus the aerofoil is said to be stalled. The lift curves are plotted by calculating the values of lift coefficients at the angles ranging from  $-3^\circ$  to  $12^\circ$ , for both a baseline aerofoil and those with bump control.

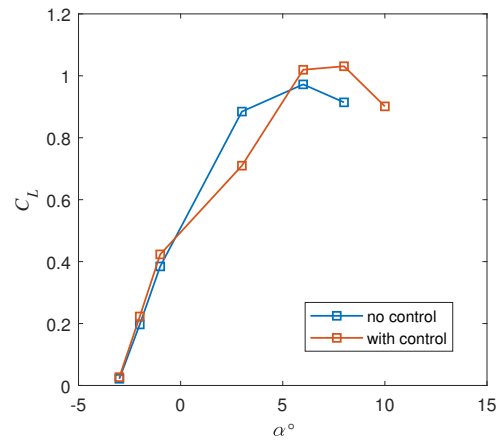
Figure 5.1 and figure 5.2 present the lift curves at a flow Mach number of 0.73, while Figure 5.3 and Figure 5.4 present the lift curves at a flow Mach number of 0.75. For a baseline aerofoil at a flow Mach number of 0.73, the linear part of its lift curve starts from  $-3^\circ$  to  $3^\circ$ , with a slope of and a zero-lift coefficient of 0.14 per degree. The flow over a baseline aerofoil becomes unsteady as the angle of attack exceeds  $3^\circ$ , and the maximum lift coefficient occurs at  $5^\circ$ , namely the stall angle of attack. The aerofoils with bump control have similar slopes and the zero-lift coefficients as the baseline aerofoil at low angles of attack. At a Mach number of 0.73, some of the forward bumps can raise the maximum lift coefficient at a higher stall angle, which are a long and high-crest bump, a long and low-crest bump and short and high-crest bump.



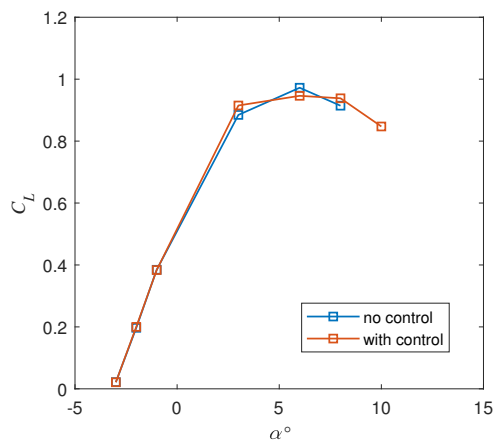
(a) Long and high-crest bump



(b) Long and low-crest bump

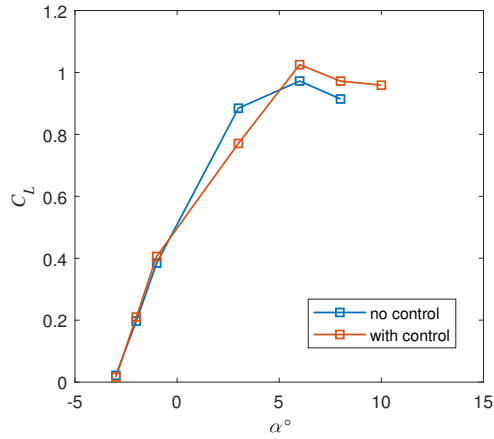


(c) Short and high-crest bump

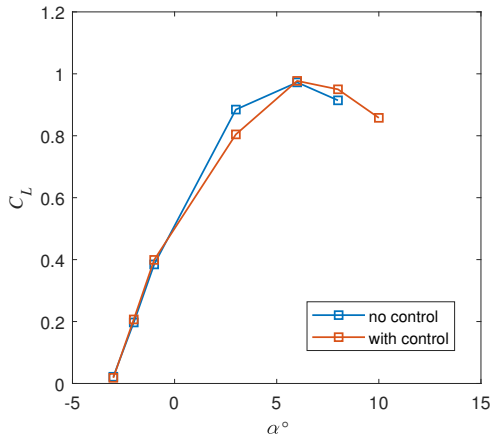


(d) Short and low-crest bump

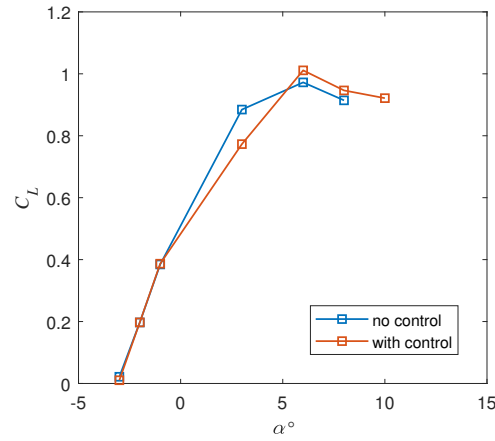
Figure 5.1: Lift curves for forward bumps ( $M_\infty=0.73$ )



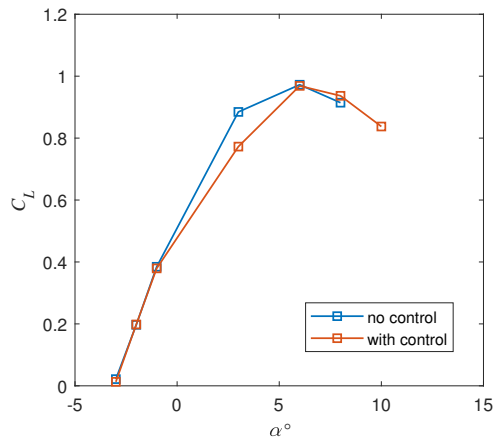
(a) Long and high-crest bump



(b) Long and low-crest bump

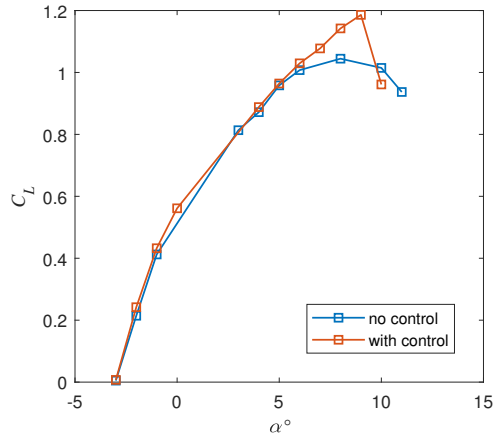


(c) Short and high-crest bump

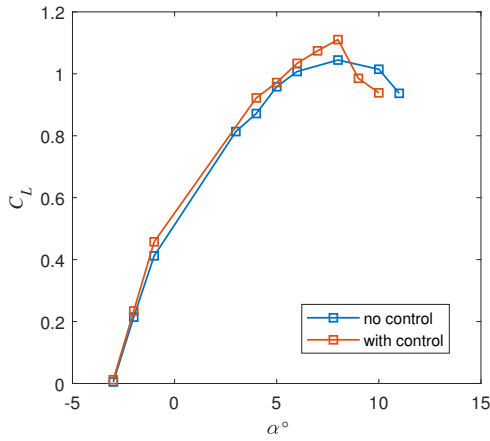


(d) Short and low-crest bump

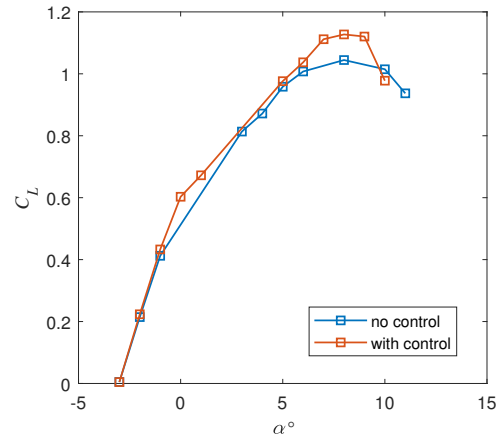
Figure 5.2: Lift curves for backward bumps ( $M_\infty = 0.73$ )



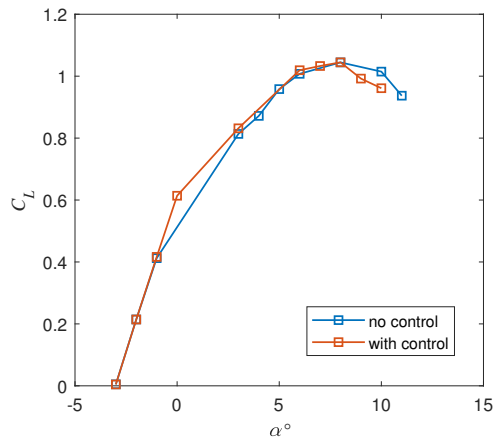
(a) Long and high-crest bump



(b) Long and low-crest bump

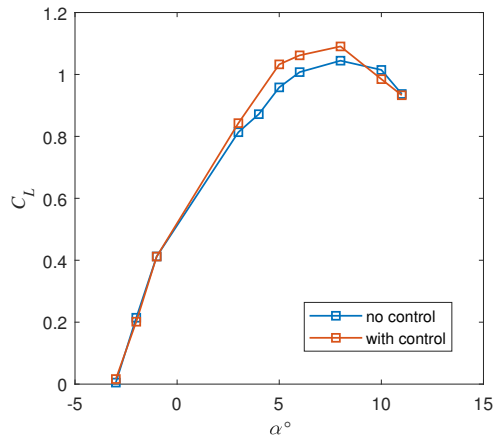


(c) Short and high-crest bump

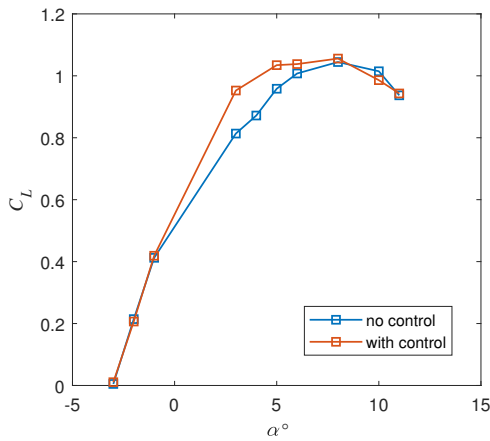


(d) Short and low-crest bump

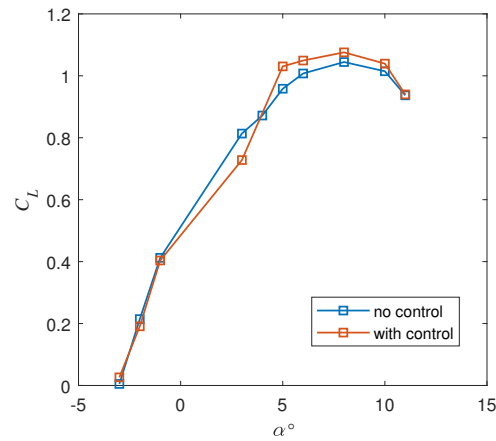
Figure 5.3: Lift curves for forward bumps ( $M_\infty=0.75$ )



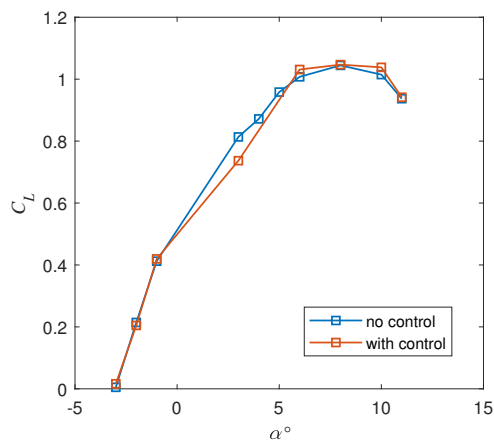
(a) Long and high-crest bump



(b) Long and low-crest bump



(c) Short and high-crest bump



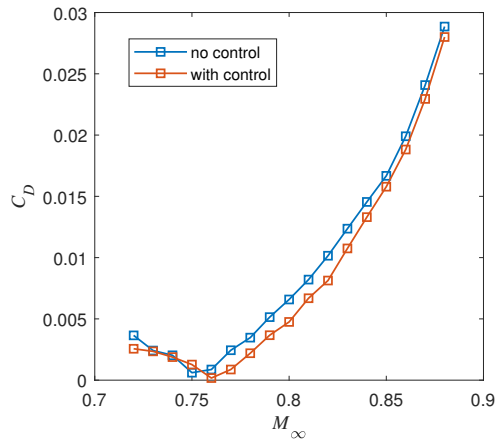
(d) Short and low-crest bump

Figure 5.4: Lift curves for backward bumps ( $M_\infty = 0.75$ )

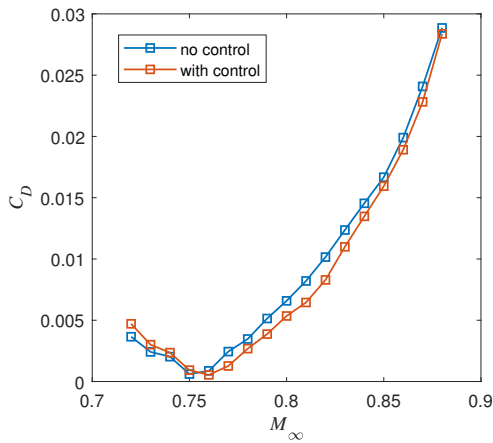
These bumps yield a maximum lift coefficient of 1 and a stall angle of attack of  $7^\circ$ . The backward bumps also shift the stall angle of attack from  $5^\circ$  to  $6^\circ$ . A backward bump with high crest creates a loss of lift at an angle of attack from  $0^\circ$  to  $5^\circ$ , whereas recovery of lift occurs from  $5^\circ$  to  $10^\circ$ , and the stall angle of attack now lags to  $9^\circ$ , compared to a  $5^\circ$  stall angle for a baseline aerofoil. A backward bump with a low crest can delay the stall angle, but cannot increase the maximum lift coefficient. For a flow Mach number of 0.75, the lift curve slope and the zero-lift coefficient for a baseline aerofoil remain roughly the same as Mach 0.73, but the stall angle of attack and the maximum lift coefficient get higher than Mach 0.73. Some of the forward bumps can increase the maximum lift coefficient, but the onset of the stall angle of attack cannot be delayed. However, some of the backward bumps can marginally increase the maximum lift coefficient, whereas the onset of stall angle of attack gets lower than a baseline aerofoil. A backward bump with long chord length produces more lift than a baseline aerofoil between  $2^\circ$  and  $9^\circ$ , but its stall angle of attack becomes lower. A backward short and high-crest bump causes the highest loss of lift at  $2^\circ$  angle of attack, but it gains more lift as the angle exceeds  $4^\circ$ , leading to a stall angle of  $8^\circ$ . A backward short and low-crest bump creates a stall angle of attack of  $8^\circ$ , at which the maximum lift coefficient becomes marginally higher than a baseline aerofoil.

### 5.3.2 Effect of drag divergence

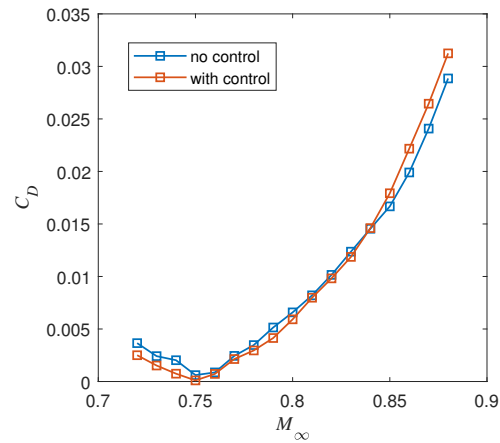
The aerodynamic drag for an aerofoil with/without control is evaluated for a transonic flow regime ranging from Mach 0.7 to 0.9. Figure 5.5 and 5.6 show the relationship between the total drag coefficient and the freestream Mach number for the forward/backward bump configurations at an angle of attack of  $3.5^\circ$ , as compared with the baseline aerofoil. Firstly, it is found that the onsets of drag divergence for a baseline aerofoil, a forward short and high-crest bump and a forward short and low-crest bump occur at a Mach number of 0.75, while the rest of the bumps yield a drag divergence Mach number of 0.76. Secondly, the drag produced by a forward long and high-crest bump and a forward long and low-crest bump is marginally lower than a baseline aerofoil for a Mach number beyond 0.76; the drag created by a forward short and high-crest bump is marginally lower than a baseline aerofoil for a Mach number between 0.72 to 0.75, but the drag will get higher if the Mach number exceeds 0.84; an aerofoil with a forward short and low-crest bump can neither delay the onset of drag divergence Mach number nor lower the drag acting on itself. Finally, a backward long and high-crest bump and a backward long and low-crest bump can decrease the aerofoil's drag from Mach 0.76 to Mach 0.86, but can increase the drag if the Mach number exceeds 0.86; a backward short and high-crest bump can lower the drag between Mach 0.76 and Mach 0.84, but becomes ineffective if Mach number is higher than 0.85; a backward short and low-crest bump can be effective to decrease the drag from Mach 0.76 to 0.84, but is no longer valid from Mach 0.85 above.



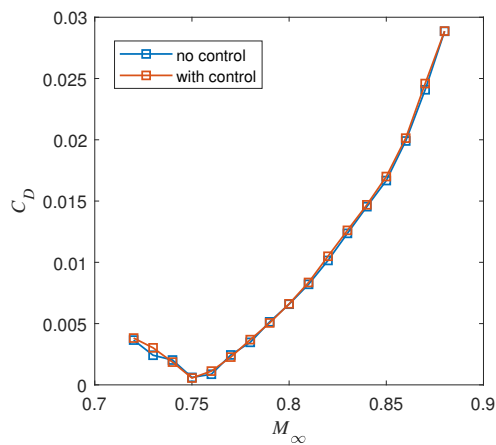
(a) Long and high-crest bump



(b) Long and low-crest bump

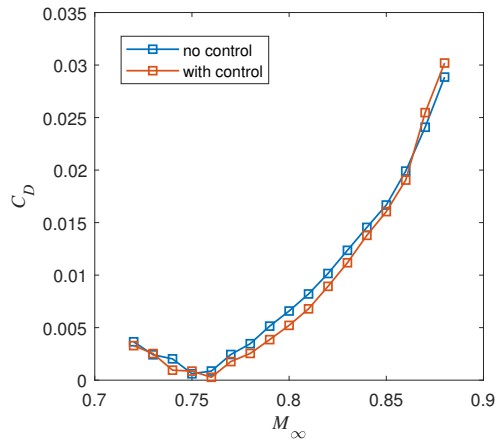


(c) Short and high-crest bump

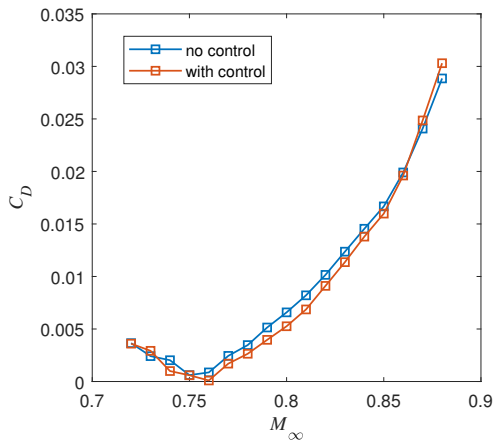


(d) Short and low-crest bump

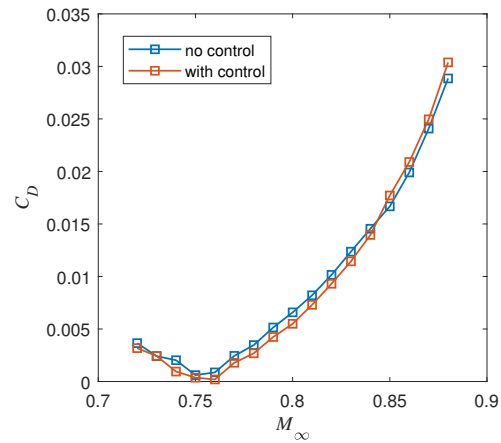
**Figure 5.5:** Total drag coefficient versus Mach number for forward bumps ( $\alpha=3.5^\circ$ )



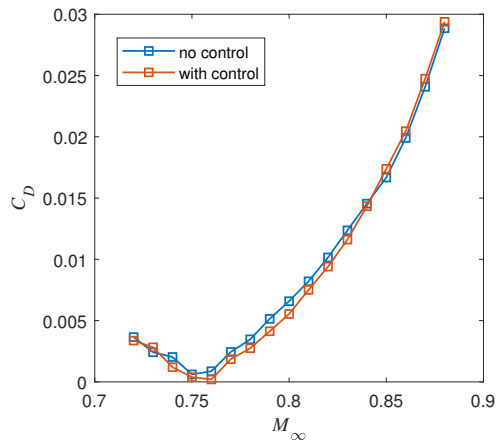
(a) Long and high-crest bump



(b) Long and low-crest bump



(c) Short and high-crest bump



(d) Short and low-crest bump

**Figure 5.6:** Total drag coefficient verses Mach number for backward bumps ( $\alpha=3.5^\circ$ )

To sum up, some of the bump configurations are capable of achieving a reasonable effort to delay the onset of drag divergence, as well as reducing the aerodynamic drag in a certain range of Mach number, except a forward short and high-crest bump and a forward short and low-crest bump. Firstly, a bump with a long chord-length can not only reduce the drag but also can widen the range of a cruising Mach number. Secondly, a bump with a short chord length has no prominent impact on delaying the onset of drag divergence but can yield a little drag reduction in a narrower range of flight Mach number. Thirdly, a bump with a high or low crest has a considerable impact on drag reduction but is not particularly effective to delay the drag divergence Mach number. Overall, a backward bump is generally more effective to fulfil both objectives than a forward bump for a higher Mach number.

### 5.3.3 Drag comparison

The total drag (parasitic drag) and viscous drag are compared and contrasted for different bump configurations. For a flow condition of  $M_\infty=0.73$  and  $\alpha=3.5^\circ$ , as shown by Figure 5.7 and 5.8, most of the forward bumps can reduce the total drag, but a forward long and low-crest bump indicates almost no reduction in the total drag due to the significantly re-expanded flow on the bump crest, while all the backward bumps can effectively reduce the total drag. At this flow condition, the reductions achieved by the forward bumps are: 12% (long and high-crest bump), 29% (short and high-crest bump) and 15% (short and low-crest bump); the reductions achieved by the backward bumps are: 29% (long and high-crest bump), 18% (long and low-crest bump), 32% (short and high-crest bump) and 21% (short and low-crest bump).

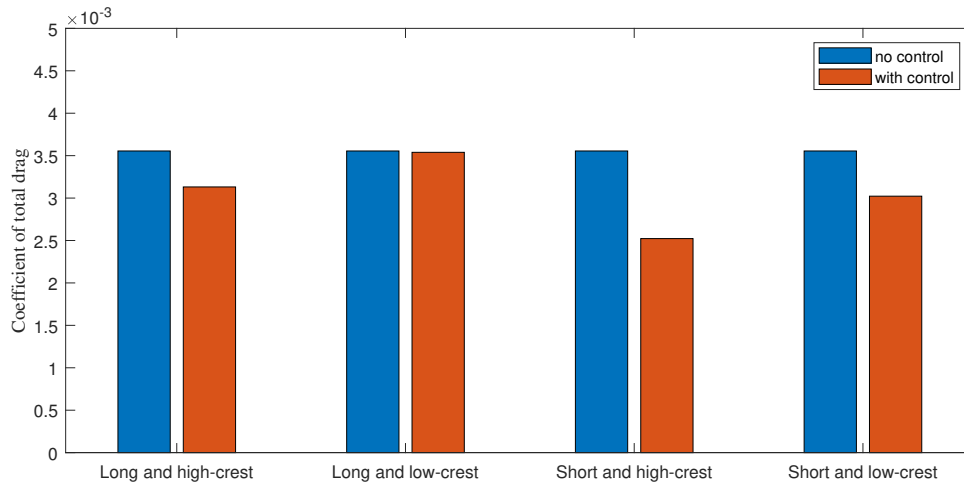


**Figure 5.7:** Total drag comparisons for the forward bumps ( $M_\infty=0.73$ ,  $\alpha=3.5^\circ$ )

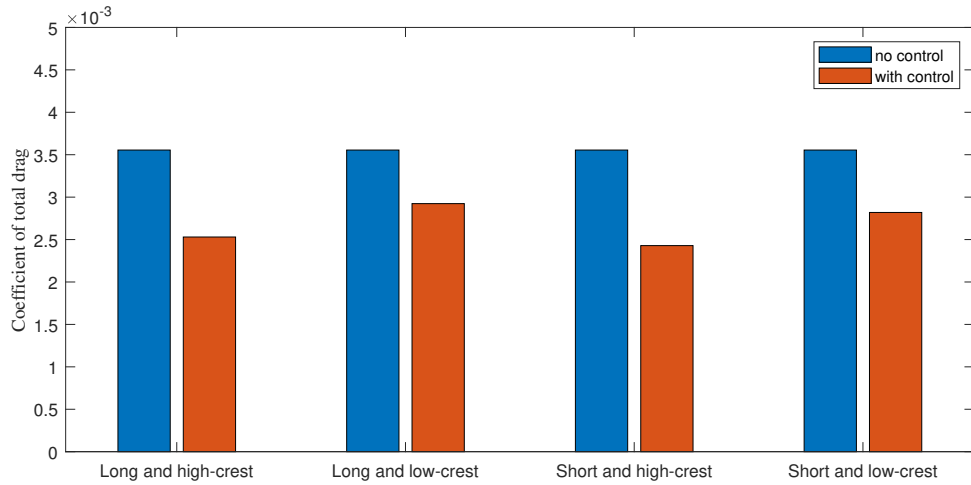


**Figure 5.8:** Total drag comparisons for the backward bumps ( $M_\infty=0.73$ ,  $\alpha=3.5^\circ$ )

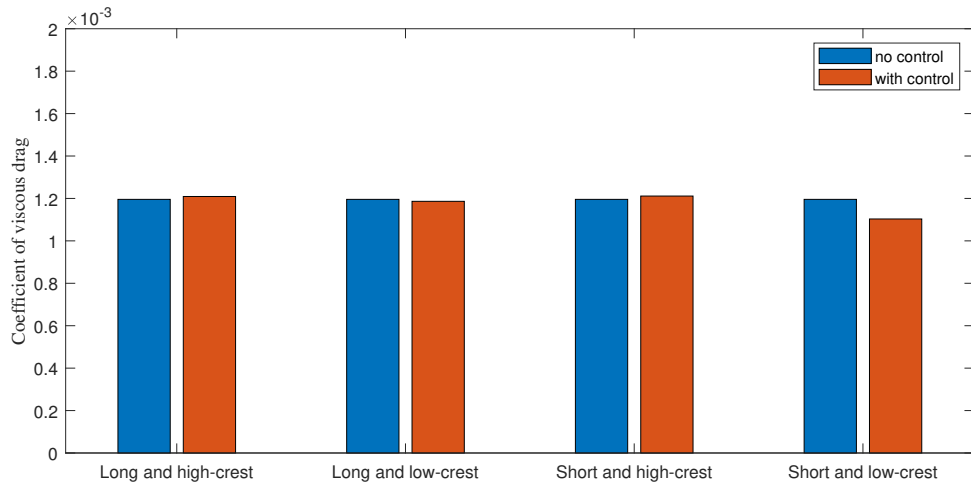


**Figure 5.9:** Viscous drag comparisons for the forward bumps ( $M_\infty=0.73$ ,  $\alpha=3.5^\circ$ )

A forward short and low-crest bump exhibits a little reduction in the viscous drag, as indicated in Figure 5.9, whereas no reductions can be found on the remaining forward bumps. The viscous drag created by the backward bumps also cannot be effectively deducted, as shown in Figure 5.10. These results show that a shock control bump can result in a viscous drag penalty, but this drawback is relatively negligible compared to the effective reduction in the total drag. The average reductions in the total drag on the aerofoils under a  $M_\infty=0.73$  and  $3.5^\circ$  angle of attack are: 18.6% (forward bumps) and 25% (backward bumps); while the average additions in the viscous drag on the aerofoils at this flow condition are: 4% (forward bumps) and 7.5% (backward bumps).

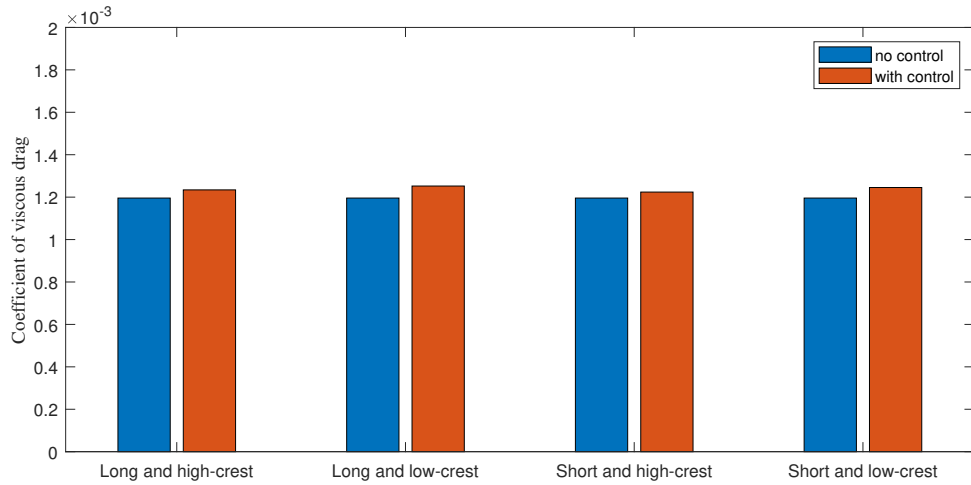


**Figure 5.10:** *Viscous drag comparisons for the backward bumps ( $M_\infty=0.73$ ,  $\alpha=3.5^\circ$ )*

Besides controlling transonic buffet, a 2D surface bump is also capable of reducing the aerodynamic drag on an aerofoil with a little addition in viscous drag. On the one hand, an aerofoil with backward bumps achieves higher reduction in total drag than the forward bumps. On the other hand, a backward short and high-crest bump has been shown to achieve the highest reduction in total drag for a transonic aerofoil under a buffet-onset condition.

# Chapter 6

## Conclusions and future work

### 6.1 Conclusions

#### I. Remarks on the numerical studies of a baseline aerofoil

- The transonic buffet flow over a supercritical aerofoil has been simulated numerically through unsteady RANS equation. The numerical model has been successfully validated, and good agreements have been shown by comparing the numerical results with the existing experimental measurements taken from the current literature.
- The transient results from URANS computation show that the shock-induced oscillations of the aerodynamic forces undergo a finite time for a specific buffet onset condition. Incremental variations of the flow Mach number and the angle of attack do not result in the unique behaviour of an unsteady aerodynamic response.

#### II. Remarks on the control performance (Answers to the questions in Section 2.8)

The transient solutions have shown that a shock control bump achieves effective mitigation of transonic buffet. It attenuates the shock-induced oscillation of the lift and drag by alleviating the unsteady pressure fluctuation on an aerofoil surface and the trailing edge, as well as creating an unseparated boundary-layer on the crest region of a bump. It has been found that a bump with a low-crest height is the most effective to suppress pressure fluctuations, and the backward bumps can produce locally thinner boundary-layers than the forward bumps.

The major characteristics of a flowfield in the presence of a bump is a formation of an oblique shock wave located at the leading edge of the bump. An additional flow re-expansion is created on the crest of the bump, which is caused by the zonal supersonic flow due to re-acceleration. The oblique shock wave and the locally re-expanded flow can vary depending on the geometrical feature of a bump configuration. It has been found that some of the bumps create desirable flow features, that is a well-established oblique shock structure without incurring significant additional expansion waves. These bumps are a forward long and low-crest bump, a forward short and low-crest bump and the backward bumps. Although a forward long and high-crest bump and a forward short and high-crest bump can cause undesirable

effects, they are still effective in some aspects that are beneficial for the control performance.

The benefits of adopting a 2D surface bump include refraining the shock-induced oscillation, such as reducing the parasitic drag, delaying the drag-rise and the stall angle of attack. However, none of these benefits can be fulfilled simultaneously. The high-crest bumps create significant pressure fluctuation in the flow zone where supersonic re-expansion is present, but they can restrict the pressure fluctuation on the trailing edge of an aerofoil.

Many of the designs can delay the stall angle of attack and gain a higher maximum lift coefficient, for a flow Mach number of 0.73. When the Mach number becomes 0.75, some of the bumps are no longer effective to achieve a lagged stall angle, also, the backward bumps create an earlier onset of the stall than the forward bumps at this Mach number. On the effect of drag-rise, a backward bump has been demonstrated to be more effective to fulfil the two objectives than a forward bump, namely delaying the drag-divergence Mach number and drag reduction. On the total drag reduction, a backward short and high-crest bump has been found to achieve the highest reduction in total drag. Besides, the backward bumps have been examined to be generally more effective to reduce aerodynamic drag than the forward bumps at a buffet-onset condition.

In general, the backward bumps perform better than the forward bumps. A backward long and low-crest bump performs the best among all the designed ones. The backward bumps have more advantages than the forward bumps. The backward bumps can not only eliminate the flow unsteadiness caused by the shock-induced separation but also stabilise the turbulent boundary-layer. Also, the aerofoil with a backward bump can be aerodynamically more efficient than that with a forward bump in terms of drag reduction, broadening the transonic speed range of operation and preventing an early aerodynamic stall. The major drawback of a shock control bump is the tiny addition of viscous drag, which cannot be avoided in all designs.

## 6.2 Recommendation for future work

The control effects on transonic buffet using a two-dimensional bump have been studied numerically. Some aspects have not been covered in the current research due to the constraints of time and resources. Therefore, further investigations are recommended in the following manners, which will offer a high potential to gain a complete insight into the control mechanism:

- Multi-objective optimisation of the bump geometry based on mathematical algorithms.
- Prediction of the buffet-onset condition with bump control via global-stability analysis.
- Further investigation probing into the unsteady results of lift curve, drag-rise and buffet boundary.

The following points are not emphasised but worth investigating on a higher demand:

- High fidelity CFD simulation in-cooperating the effect of wingspan.
- Wind tunnel validation that confirms the numerical results of a control bump.

# Bibliography

- Alber, I. E., Bacon, J. W., Masson, B. S., and Collins, D. J. (1973). An experimental investigation of turbulent transonic viscous-inviscid interactions. *AIAA Journal*, 11(5):620–627.
- Anderson, J. D. (1995). *Computational Fluid Dynamics the Basics With Applications*. McGraw-Hill, Inc.
- Anderson, J. D. (2016). *Fundamentals of Aerodynamics*, volume 6th. McGraw-Hill New York.
- Apetrei, R. M., Curiel-Sosa, J. L., and Qin, N. (2018). Using the reynolds stress model to predict shock-induced separation on transport aircraft. *Journal of Aircraft*, 56(2):583–590.
- Ashill, P., Fulker, J., and Hackett, K. (2005). A review of recent developments in flow control. *The Aeronautical Journal*, 109(1095):205–232.
- Babinsky, H. and Ogawa, H. (2008). SBLI control for wings and inlets. *Shock Waves*, 18(2):89.
- Ballhaus, W. and Goorjian, P. (1977). Implicit finite-difference computations of unsteady transonic flows about airfoils. *AIAA Journal*, 15(12):1728–1735.
- Barakos, G. and Drikakis, D. (2000). Numerical simulation of transonic buffet flows using various turbulence closures. *International Journal of Heat and Fluid Flow*, 21(5):620–626.
- Bhamidipati, K. K., Reasor, D. A., and Pasiliao, C. L. (2015). Unstructured grid simulations of transonic shockwave-boundary layer interaction-induced oscillations. In *22nd AIAA Computational Fluid Dynamics Conference*, page 2287.
- Birkenmeyer, R., Rosemann, H., and Stanewsky, E. (2000). Shock control on a swept wing. *Aerospace Sci. Technol*, 4:147–156.
- Bogar, T. (1986). Structure of self-excited oscillations in transonic diffuser flows. *AIAA journal*, 24(1):54–61.
- Bogdonoff, S. and Shapey, B. (1987). Three-dimensional shock wave turbulent boundary layer interaction for a 20 deg sharp fin at mach 3. In *25th AIAA Aerospace Sciences Meeting*, page 554.
- Braza, M. and Hourigan, K. (2009). *IUTAM Symposium on Unsteady Separated Flows and their Control: Proceedings of the IUTAM Symposium Unsteady Separated Flows and their Control, Corfu, Greece, 18-22 June 2007*, volume 14. Springer Science & Business Media.

- Bruce, P. and Colliss, S. (2015). Review of research into shock control bumps. *Shock Waves*, 25(5):451–471.
- Brunet, V., Deck, S., Molton, P., and Thiery, M. (2005). A complete experimental and numerical study of the buffet phenomenon over the oat 15 a airfoil. *ONERA: Tire a Part*, (35):1–9.
- Caruana, D., Mignosi, A., Corrège, M., Le Pourhiet, A., and Rodde, A. (2005). Buffet and buffeting control in transonic flow. *Aerospace Science and Technology*, 9(7):605–616.
- Chen, C., Sajben, M., and Kroutil, J. (1979). Shock-wave oscillations in a transonic diffuser flow. *AIAA journal*, 17(10):1076–1083.
- Crouch, J., Garbaruk, A., and Magidov, D. (2007). Predicting the onset of flow unsteadiness based on global instability. *Journal of Computational Physics*, 224(2):924–940.
- Crouch, J., Garbaruk, A., Magidov, D., and Travin, A. (2009). Origin of transonic buffet on aerofoils. *Journal of fluid mechanics*, 628:357–369.
- Deck, S. (2005). Numerical simulation of transonic buffet over a supercritical airfoil. *AIAA journal*, 43(7):1556–1566.
- Eastwood, J. P. and Jarrett, J. P. (2012). Toward designing with three-dimensional bumps for lift/drag improvement and buffet alleviation. *AIAA journal*, 50(12):2882–2898.
- Edwards, J. W. (1996). Transonic shock oscillations and wing flutter calculated with an interactive boundary layer coupling method.
- Ganapathisubramani, B., Clemens, N., and Dolling, D. (2009). Low-frequency dynamics of shock-induced separation in a compression ramp interaction. *Journal of Fluid Mechanics*, 636:397–425.
- Ganapathisubramani, B., Clemens, N. T., and Dolling, D. (2007). Effects of upstream boundary layer on the unsteadiness of shock-induced separation. *Journal of fluid Mechanics*, 585:369–394.
- Iovnovich, M. and Raveh, D. E. (2012). Reynolds-averaged navier-stokes study of the shock-buffet instability mechanism. *AIAA journal*, 50(4):880–890.
- Jacquín, L., Molton, P., Deck, S., Maury, B., and Soulevant, D. (2009). Experimental study of shock oscillation over a transonic supercritical profile. *AIAA journal*, 47(9):1985–1994.
- Jameson, A. (1991). Time dependent calculations using multigrid, with applications to unsteady flows past airfoils and wings. In *10th Computational Fluid Dynamics Conference*, page 1596.
- Kim, H., Matsuo, K., and Setoguchi, T. (1996). Investigation on onset of shock-induced separation. *Shock Waves*, 6:275–286.
- König, B., Pätzold, M., Lutz, T., Krämer, E., Rosemann, H., Richter, K., and Uhlemann, H. (2009). Numerical and experimental validation of three-dimensional shock control bumps. *Journal of Aircraft*, 46(2):675–682.

- Lange, R. H. (1954). Present status of information relative to the prediction of shock-induced boundary-layer separation.
- Langtry, R. and Menter, F. (2005). Transition modeling for general CFD applications in aeronautics. In *43rd AIAA aerospace sciences meeting and exhibit*, page 522.
- Lee, B. (1990). Oscillatory shock motion caused by transonic shock boundary-layer interaction. *AIAA journal*, 28(5):942–944.
- Lee, B. (2001). Self-sustained shock oscillations on airfoils at transonic speeds. *Progress in Aerospace Sciences*, 37(2):147–196.
- Love, E. S. (1955). Pressure rise associated with shock-induced boundary-layer separation.
- Mabey, D. (1989). Buffeting criteria for a systematic series of wings. *Journal of Aircraft*, 26(6):576–582.
- Mabey, D. G. (1981). Some remarks on buffeting. Technical report, ROYAL AIRCRAFT ESTABLISHMENT FARNBOROUGH (ENGLAND).
- Mayer, R., Lutz, T., and Krämer, E. (2015). Toward numerical optimization of buffet alleviating three-dimensional shock control bumps. In *6th European Conference for Aerospace Sciences*, pages 1–12.
- Megson, T. H. G. (2016). *Aircraft structures for engineering students*. Butterworth-Heinemann.
- Murayama, M., Yamamoto, K., Hashimoto, A., Ishida, T., Ueno, M., Tanaka, K., and Ito, Y. (2013). Summary of JAXA studies for the fifth AIAA CFD drag prediction workshop using UPACS and FaSTAR. In *51st AIAA Aerospace Sciences Meeting including the New Horizons Forum and Aerospace Exposition*, page 49.
- Ogawa, H., Babinsky, H., Pätzold, M., and Lutz, T. (2008). Shock-wave/boundary-layer interaction control using three-dimensional bumps for transonic wings. *AIAA journal*, 46(6):1442–1452.
- Orlik, E., Mazellier, N., and Kourta, A. (2011). Numerical prediction of transonic buffeting by means of standard and time-dependent turbulent models. In *TSFP DIGITAL LIBRARY ONLINE*. Begel House Inc.
- Panda, J. (1998). Shock oscillation in underexpanded screeching jets. *Journal of Fluid Mechanics*, 363:173–198.
- Pearcey, H. (1959). *Some effects of shock-induced separation of turbulent boundary layers in transonic flow past aerofoils*. HM Stationery Office.
- Piponniau, S., Dussauge, J.-P., Debieve, J.-F., and Dupont, P. (2009). A simple model for low-frequency unsteadiness in shock-induced separation. *Journal of Fluid Mechanics*, 629:87–108.

- Plotkin, K. J. (1975). Shock wave oscillation driven by turbulent boundary-layer fluctuations. *AIAA Journal*, 13(8):1036–1040.
- Qin, N., Wong, W., and Le Moigne, A. (2008). Three-dimensional contour bumps for transonic wing drag reduction. *Proceedings of the Institution of Mechanical Engineers, Part G: Journal of Aerospace Engineering*, 222(5):619–629.
- Raghunathan, S., Gillan, M., Cooper, R., Mitchell, R., and Cole, J. (1999). Shock oscillations on biconvex aerofoils. *Aerospace Science and Technology*, 3(1):1–9.
- Rahman, M. R., Labib, M. I., Hasan, A. B. M. T., Joy, M. S. H., Setoguchi, T., and Kim, H. D. (2015). Control of transonic shock wave oscillation over a supercritical airfoil. *Open Journal of Fluid Dynamics*, 5(04):302.
- Rahman, M. R., Labib, M. I., Hasan, A. T., Ali, M., Mitsutake, Y., and Setoguchi, T. (2016). Effect of cavity on shock oscillation in transonic flow over rae2822 supercritical airfoil. In *AIP Conference Proceedings*, volume 1754, page 040025. AIP Publishing.
- Reneaux, J., Brunet, V., Caruana, D., Deck, S., and Naudin, P. (2005). A combined experimental and numerical investigation of the buffet phenomenon and its control through passive and active devices. *ONERA: Tire a Part*, (103):1.
- Reshotko, E. and Tucker, M. (1955). Effect of a discontinuity on turbulent boundary-layer-thickness parameters with application to shock-induced separation.
- Sabater, C. and Görtz, S. (2019). An efficient bi-level surrogate approach for optimizing shock control bumps under uncertainty. In *AIAA Scitech 2019 Forum*, page 2214.
- Sartor, F., Mettot, C., and Sipp, D. (2014). Stability, receptivity, and sensitivity analyses of buffeting transonic flow over a profile. *AIAA Journal*, 53(7):1980–1993.
- Smith, A., Babinsky, H., Fulker, J., and Ashill, P. (2004). Shock wave/boundary-layer interaction control using streamwise slots in transonic flows. *Journal of Aircraft*, 41(3):540–546.
- Spalart, P. and Allmaras, S. (1992). A one-equation turbulence model for aerodynamic flows. In *30th aerospace sciences meeting and exhibit*, page 439.
- Stanewsky, E. and Little, B. (1971). Separation and reattachment in transonic airfoil flow. *Journal of Aircraft*, 8(12):952–958.
- Tai, T. C. (1977). Theoretical aspects of dromedaryfoil. Technical report, DAVID W TAYLOR NAVAL SHIP RESEARCH AND DEVELOPMENT CENTER BETHESDA MD.
- Thiery, M. and Coustols, E. (2006). Numerical prediction of shock induced oscillations over a 2d airfoil: Influence of turbulence modelling and test section walls. *International journal of heat and fluid flow*, 27(4):661–670.
- Tian, Y., Liu, P., and Feng, P. (2011). Shock control bump parametric research on supercritical airfoil. *Science China Technological Sciences*, 54(11):2935.
- Tijdeman, H. (1977). Investigations of the transonic flow around oscillating airfoils.

- Touber, E. and Sandham, N. D. (2009). Large-eddy simulation of low-frequency unsteadiness in a turbulent shock-induced separation bubble. *Theoretical and Computational Fluid Dynamics*, 23(2):79–107.
- Wikimedia (2013). Shockwave above airliner wing. [https://commons.wikimedia.org/wiki/File:Shockwave\\_above\\_airliner\\_wing.jpg](https://commons.wikimedia.org/wiki/File:Shockwave_above_airliner_wing.jpg). [Online].
- Wilcox, D. C. (1988). Reassessment of the scale-determining equation for advanced turbulence models. *AIAA journal*, 26(11):1299–1310.
- Xiao, Q., Tsai, H.-M., and Liu, F. (2006). Numerical study of transonic buffet on a supercritical airfoil. *AIAA journal*, 44(3):620–628.
- Yun, T., Shiqi, G., Peiqing, L., and Jinjun, W. (2017). Transonic buffet control research with two types of shock control bump based on rae2822 airfoil. *Chinese Journal of Aeronautics*, 30(5):1681–1696.
- Zhu, M., Li, Y., Qin, N., Huang, Y., Deng, F., Wang, Y., and Zhao, N. (2019). Shock control of a low-sweep transonic laminar flow wing. *AIAA Journal*, 57(6):2408–2420.